

**WAVE PROPAGATION BASED
STRUCTURAL HEALTH MONITORING**

A thesis submitted to
the Faculty of Graduate Studies and Research
in Partial Fulfillment of the requirements for the degree

Masters of Applied Science

by

Amin Fereidooni

B.Sc., IUST, Tehran, Iran

Department of Civil and Environmental Engineering
Carleton University

Ottawa-Carleton Institute of Civil and Environmental Engineering

September 2009

©2009 Amin Fereidooni



Library and Archives
Canada

Published Heritage
Branch

395 Wellington Street
Ottawa ON K1A 0N4
Canada

Bibliothèque et
Archives Canada

Direction du
Patrimoine de l'édition

395, rue Wellington
Ottawa ON K1A 0N4
Canada

Your file *Votre référence*
ISBN: 978-0-494-60266-9
Our file *Notre référence*
ISBN: 978-0-494-60266-9

NOTICE:

The author has granted a non-exclusive license allowing Library and Archives Canada to reproduce, publish, archive, preserve, conserve, communicate to the public by telecommunication or on the Internet, loan, distribute and sell theses worldwide, for commercial or non-commercial purposes, in microform, paper, electronic and/or any other formats.

The author retains copyright ownership and moral rights in this thesis. Neither the thesis nor substantial extracts from it may be printed or otherwise reproduced without the author's permission.

AVIS:

L'auteur a accordé une licence non exclusive permettant à la Bibliothèque et Archives Canada de reproduire, publier, archiver, sauvegarder, conserver, transmettre au public par télécommunication ou par l'Internet, prêter, distribuer et vendre des thèses partout dans le monde, à des fins commerciales ou autres, sur support microforme, papier, électronique et/ou autres formats.

L'auteur conserve la propriété du droit d'auteur et des droits moraux qui protègent cette thèse. Ni la thèse ni des extraits substantiels de celle-ci ne doivent être imprimés ou autrement reproduits sans son autorisation.

In compliance with the Canadian Privacy Act some supporting forms may have been removed from this thesis.

While these forms may be included in the document page count, their removal does not represent any loss of content from the thesis.

Conformément à la loi canadienne sur la protection de la vie privée, quelques formulaires secondaires ont été enlevés de cette thèse.

Bien que ces formulaires aient inclus dans la pagination, il n'y aura aucun contenu manquant.


Canada

Abstract

A wave propagation based damage identification approach is proposed. This approach relies on a comparison of the structural wave speeds in the healthy and damaged structure. Estimates of the time of travel between two measurement locations, and hence of the wave speed, are obtained through cross-correlation analysis on the measured signals. The one-dimensional structural elements considered are a rod carrying non-dispersive wave in axial vibration and a beam conducting dispersive wave in lateral vibration.

Waves generated by both random and transient excitations are considered. It is shown through computer simulation studies that the proposed method is successful in providing reasonably accurate estimates of both the location and extent of damage even in the presence of significant measurement noise and reflections from boundaries. Accuracy of the estimates can be improved by increasing the measurement locations. Certain limitations of the method and the related future research needs are identified.

Dedicated to my parents

ACKNOWLEDGMENTS

I would like to sincerely thank my supervisor Professor J. L. Humar, Distinguished Research Professor in the Department of Civil Engineering at Carleton University, for providing me encouragement, motivation and guidance during the course of my thesis. Working under supervision of Professor Humar was an invaluable experience that allowed me to learn many aspects of science and life. I am also thankful to Professor Humar and to Carleton University for providing me financial support during my graduate studies.

I am grateful to my co-supervisor Professor A. Sarkar, Associate Professor in the Department of Civil and Environmental Engineering at Carleton University, for fruitful discussions and helpful suggestions in many stages of my research.

I am indebted to my parents whose love, support and understanding helped me to pursue graduate studies. My final thought is always with them.

Finally, I wish to thank my friends who made the two years at Carleton an enjoyable period in my life.

Table of Contents

Abstract	ii
Acknowledgements	iv
Table of Contents	v
List of Tables	ix
List of Figures	xii
Notations	xxii
Chapter 1: Introduction	1
1.1 General	1
1.2 Literature Survey of Vibration Based Damage Identification Methods	4
1.3 The Proposed Approach for Damage Detection	7
1.4 Objectives of the Present Study	10
1.5 Layout of the thesis	12
Chapter 2: Random Dynamical System	14
2.1 Introduction	14
2.2 Random Data Analysis	15
2.2.1 Random Process	15
2.2.2 Stationary Random Process	15
2.2.3 Autocorrelation Function	16
2.2.4 Cross-Correlation Function	22

2.2.5 Cross-Correlation Coefficient	24
2.3 Single Input/Single Output Relationship	25
2.3.1 Ideal Dynamical System	25
2.3.2 Stationary Input	27
2.3.3 Transient Input	28
Chapter 3: Time Delay Estimation and Path Identification	30
3.1 Introduction	30
3.2 Non-Dispersive Propagation Path Identification	31
3.2.1 Noise Free Case	31
3.2.2 Noisy Case	38
3.3 Dispersive Propagation Path Identification	41
Chapter 4: Wave Propagation	55
4.1 Introduction	55
4.2 Non-dispersive Wave propagation	56
4.2.1 Spectral Derivation	56
4.2.2 FEM derivation	60
4.3 Dispersive Wave Propagation	63
4.3.1 Spectral Derivation	63
4.3.2 FEM Derivation	69
4.4 Numerical Implementation	73
4.4.1 Spectral Approach	73

4.4.2 FEM Approach	75
Chapter 5: Numerical Illustration : Non-dispersive Wave Propagation	77
5.1 Introduction	77
5.2 Model Validation	78
5.2.1 Analytical Model	78
5.2.2 FEM Model	85
5.3 Time Delay Estimation	93
5.3.1 Problem Description	93
5.3.2 Effect of Loading	94
5.3.3 Effect of Reflection	103
5.3.4 Effect of Noise	113
5.4 Damage Detection	120
5.4.1 Damage on the Left Side of Sensor A	121
5.4.2 Damage on the Right Side of Sensor B	128
5.4.3 Damage Between Sensors A and B	135
5.4.4 Conclusions	144
Chapter 6: Numerical Illustration: Dispersive Wave propagation	146
6.1 Introduction	146
6.2 Model Validation	147
6.2.1 Analytical Model	147
6.2.2 FEM Model	154

6.3 Time Delay Estimation	159
6.3.1 Effect of Loading	159
6.3.2 Effect of Length of Propagation Path	172
6.3.3 Effect of Reflection	175
6.3.4 Effect of Noise	180
6.4 Damage Detection	188
6.4.1 Damage Length $L_d = 2 m$	190
6.4.2 Damage Length $L_d = 4 m$	193
6.4.3 Conclusions	195
Chapter 7: Summary, Conclusions and Future Research	197
7.1 Summary	197
7.2 Conclusions	199
7.3 Future Research	201
References	204

List of Tables

	Page
Table (5.1): Material properties of the rod model.....	79
Table (5.2): Material properties of rod model per unit length.....	79
Table (5.3): FEM mesh properties.....	87
Table (5.4): Arrival time of incident and reflected waves in a rod with absorbing-fixed ends.....	104
Table (5.5): Arrival time of incident and reflected waves in a rod with fixed-absorbing ends.....	108
Table (5.6): Arrival time of incident and reflected waves in a rod with fixed-fixed ends.....	111
Table (5.7): Calculation of time delay in undamaged and damaged rod (damage length 2.5 m).....	125
Table (5.8): Calculation of damage extent in damaged rod (damage length 2.5 m).....	125
Table (5.9): Calculation of time delay in undamaged and damaged rod (damage length 1m).....	127
Table (5.10): Calculation of damage extent in damaged rod (damage length 1m).....	127
Table (5.11): Calculation of time delay in undamaged and damaged rod (damage length 2.5 m).....	132

Table (5.12):	Calculation of damage extent in damaged rod (damage length 2.5 m).....	132
Table (5.13):	Calculation of time delay in undamaged and damaged rod (damage length 1 m).....	134
Table (5.14):	Calculation of damage extent in damaged rod (damage length 2.5 m).....	135
Table (5.15):	Calculation of time delay in undamaged and damaged rod (damage length 2.5 m).....	138
Table (5.16):	Calculated and estimated time delay in damaged rod (damage length 2.5 m).....	139
Table (5.17):	Calculation of damage extent in damaged rod (damage length 2.5 m).....	139
Table (5.18):	Calculation of time delay in undamaged and damaged rod (damage length 1 m).....	142
Table (5.19):	Calculated and estimated time delay in damaged rod (damage length 1 m).....	143
Table (5.20):	Calculation of damage extent in damaged rod (damage length 1 m).....	143
Table (6.1):	Material properties of the beam model.....	148
Table (6.2):	Material properties of beam model per unit length.....	148
Table (6.3):	FEM mesh properties.....	155
Table (6.4):	Arrival time of incident and reflected waves in a simply supported beam.....	175

Table (6.5):	Percentage of error of estimated time delay	179
Table (6.6):	Calculation of damage extent in damaged beam (damage length $2m$).....	192
Table (6.7)	Calculation of damage extent in damaged beam (damage length $4m$).....	194

List of Figures

	Page
Figure (2.1): Autospectral density function of narrow-band white random process.....	19
Figure (2.2): Autocorrelation function of narrow-band white random process....	19
Figure (2.3): Autospectral density function for broad-band white random process.....	21
Figure (2.4): Autocorrelation function of broad-band white random process.....	21
Figure (2.5): An ideal single input/single output system.....	28
Figure (3.1): Cross-correlation coefficient of narrow-band white input and output of a non-dispersive path.....	36
Figure (3.2): Cross-correlation coefficient of broad-band white input and output of a non-dispersive path.....	38
Figure (3.3): Cross-correlation coefficient of narrow-band white input and output of a dispersive path.....	50
Figure (3.4): Frequency selective band-pass filter.....	54
Figure (4.1): Typical velocity response of an impacted rod.....	59
Figure (4.2): Typical velocity response of an impacted beam.....	66
Figure (4.3): Carrier wave and group wave in dispersive wave propagation.....	69
Figure (4.4): Numerical scheme of spectral solution.....	74
Figure (4.5): Numerical scheme of FEM solution.....	76
Figure (5.1): Analytical model: infinite rod impacted at the center	78
Figure (5.2): Triangular impulsive force applied at the center of infinite rod.....	80
Figure (5.3): Fourier spectrum of impulsive force.....	81

Figure (5.4):	Velocity response of an infinite rod impacted at the center.....	84
Figure (5.5):	FEM model: rod impacted at the center.....	85
Figure (5.6):	Velocity response of impacted rod with absorbing boundary condition.....	90
Figure (5.7):	Velocity response of impacted rod with free boundary condition...	91
Figure (5.8):	Velocity response of impacted rod with fixed boundary condition.	92
Figure (5.9):	Rod model for time delay estimation problem.....	94
Figure (5.10):	A sample of the narrow-band force history	95
Figure (5.11):	Autospectral density function of narrow-band force.....	95
Figure (5.12):	Acceleration response a) at sensor A b) at sensor.....	96
Figure (5.13):	Autospectral density function of acceleration responses a) at sensor A b) at sensor B.....	97
Figure (5.14):	Cross-correlation coefficient of acceleration response to narrow-band force.....	98
Figure (5.15):	Cross-correlation coefficient of velocity response to narrow-band force.....	98
Figure (5.16):	Cross-correlation coefficient of acceleration response to broad-band force.....	99
Figure (5.17):	Cross-correlation coefficient of velocity response to broad-band force.....	100
Figure (5.18):	Triangular impulsive force.....	101
Figure (5.19):	Fourier spectrum of the triangular impulsive force.....	101
Figure (5.20):	Acceleration response due to triangular impulsive force a) at sensor A b) at sensor B.....	102

Figure (5.21):	Cross-correlation coefficient of acceleration response to transient force.....	102
Figure (5.22):	Cross-correlation coefficient of velocity response to transient force.....	103
Figure (5.23):	Model of rod with absorbing-fixed ends.....	104
Figure (5.24):	Cross-correlation coefficient of acceleration response in rod with absorbing-fixed ends.....	106
Figure (5.25):	Cross-correlation coefficient of acceleration responses (first peak): comparison of rod with absorbing-absorbing and absorbing -fixed ends.....	106
Figure (5.26):	Cross-correlation coefficient of acceleration response in rod with absorbing-fixed ends (second peak).....	107
Figure (5.27):	Model of rod with fixed-absorbing ends.....	108
Figure (5.28):	Cross-correlation coefficient of acceleration response in rod with fixed-absorbing ends.....	109
Figure (5.29):	Cross-correlation coefficient of acceleration responses (first peak): comparison of rod with absorbing-absorbing and fixed-absorbing ends.....	110
Figure (5.30):	Cross-correlation coefficient of acceleration response in rod with fixed-absorbing ends (second peak).....	110
Figure (5.31):	Model of rod with fixed-fixed ends.....	111
Figure (5.32):	Cross-correlation coefficient of acceleration response in rod with fixed-fixed ends.....	112
Figure (5.33):	Response at sensor A a) acceleration b) noise (R=30%) c) noisy acceleration.....	114

Figure (5.34):	Response at sensor B a) acceleration b) noise (R=30%) c)noisy acceleration.....	114
Figure (5.35):	Autospectral density function of noisy acceleration (R=30%) response at a) sensor A b) sensor B.....	115
Figure (5.36):	Cross-correlation coefficient of acceleration response in presence of 30% noise.....	116
Figure (5.37):	Cross-correlation coefficient between noisy acceleration measurements: comparison of the effect of different levels of noise on first peak.....	117
Figure (5.38):	Cross-correlation coefficient between noisy acceleration measurements: comparison of the effect of different levels of noise on second peak	117
Figure (5.39):	Cross-correlation coefficient between noisy acceleration measurements: comparison of the effect of different levels of noise on third peak.....	118
Figure (5.40):	Cross-correlation function between noisy acceleration measurements: comparison of the effect of different levels of noise on first peak.....	118
Figure (5.41):	Cross-correlation function between noisy acceleration measurements: comparison of the effect of different levels of noise on second peak.....	119
Figure (5.42):	Cross-correlation function between noisy acceleration measurements: comparison of the effect of different levels of noise on third peak.....	119
Figure (5.43):	Model of rod with damage at left side of sensor A.....	121

Figure (5.44):	Cross-correlation function of acceleration measurements: 10% damage on the left side of sensor A (damage length 2.5 m)	122
Figure (5.45):	Cross-correlation function of acceleration measurements: comparison of the effect of different damage extent on the first peak (damage length 2.5 m).....	122
Figure (5.46):	Cross-correlation function of acceleration measurements: comparison of the effect of different damage extent on the second peak (damage length 2.5 m).....	123
Figure (5.47):	Cross-correlation function of acceleration measurements: comparison of the effect of different damage extent on the third peak (damage length 2.5 m).....	123
Figure (5.48):	Cross-correlation function of acceleration measurements: comparison of the effect of different damage extent on the third peak (damage length 1 m).....	126
Figure (5.49):	Model of rod with damage on right side of sensor B.....	128
Figure (5.50):	Cross-correlation function of acceleration measurements: 10% damage on the right side of sensor B (damage length 2.5 m).....	130
Figure (5.51):	Cross-correlation function of acceleration measurements: comparison of the effect of different damage extent on the first peak (damage length 2.5 m).....	130
Figure (5.52):	Cross-correlation function of acceleration measurements: comparison of the effect of different damage extent on the third peak (damage length 2.5 m).....	131

Figure (5.53):	Cross-correlation function of acceleration measurements: comparison of the effect of different damage extent on the second peak (damage length 2.5 m).....	131
Figure (5.54):	Cross-correlation function of acceleration measurements: comparison of the effect of different damage extent on the second peak (damage length 1 m).....	134
Figure (5.55):	Model of damage between sensors A and B.....	135
Figure (5.56):	Cross-correlation function of acceleration measurements: 10% damage between sensor A and B (damage length 2.5 m).....	136
Figure (5.57):	Cross-correlation function of acceleration measurements: comparison of the effect of different damage extent on the first peak (damage length 2.5 m).....	137
Figure (5.58):	Cross-correlation function of acceleration measurements: comparison of the effect of different damage extent on the second peak (damage length 2.5 m).....	137
Figure (5.59):	Cross-correlation function of acceleration measurements: comparison of the effect of different damage extent on the third peak (damage length 2.5 m).....	138
Figure (5.60):	Cross-correlation function of acceleration measurements: comparison of the effect of different damage extent on the first peak (damage length 1 m).....	141
Figure (5.61):	Cross-correlation function of acceleration measurements: comparison of the effect of different damage extent on the second peak (damage length 1 m).....	141

Figure (5.62):	Cross-correlation function of acceleration measurements: comparison of the effect of different damage extent on the third peak (damage length 1 m).....	142
Figure (6.1):	Analytical model: infinite beam impacted at center.....	147
Figure (6.2):	Triangular impulsive force applied at the center of infinite beam..	149
Figure (6.3):	Fourier spectrum of impulsive force.....	149
Figure (6.4):	Velocity response of infinite beam impacted at the center.....	153
Figure (6.5):	FEM model: finite beam impacted at center.....	154
Figure (6.6):	Velocity response of impacted beam: ____beam with fixed-fixed boundary _ _ _ _ infinite beam	157
Figure (6.7):	Velocity response of impacted beam: ____simply supported beam _ _ _ _ infinite beam	158
Figure (6.8):	Beam model for time delay estimation problem: investigation of the effect of different types of loading.....	159
Figure (6.9):	A sample of the narrow-band force history.....	161
Figure (6.10):	Autospectral density function of narrow-band force.....	161
Figure (6.11):	Acceleration response a) at sensor A b) at sensor.....	162
Figure (6.12):	Autospectral density function of acceleration responses a) at sensor A b) at sensor B.....	163
Figure (6.13):	Cross-correlation coefficient of acceleration response to narrow-band force.....	163
Figure (6.14):	Cross-correlation coefficient of velocity response to narrow-band force.....	164
Figure (6.15):	Cross-correlation coefficient of acceleration response to narrow-band force (with the bandwidth of 1/3 of an octave).....	165

Figure (6.16):	Cross-correlation coefficient of acceleration response to broad-band force.....	166
Figure (6.17):	A sample of filtered acceleration response a) at sensor A b) at sensor B (with the pass band of one octave).....	166
Figure (6.18):	Autospectral density f-unction of filtered acceleration response a) at sensor A b) at sensor B.....	167
Figure (6.19):	Cross-correlation coefficient of filtered acceleration response to broad-band force	167
Figure (6.20):	Triangular impulsive force	168
Figure (6.21):	Fourier spectrum of the triangular impulsive force	169
Figure (6.22):	Filtered acceleration response a) at sensor A b) at sensor B (with the pass band of one octave).....	169
Figure (6.23):	Fourier spectrum of filtered acceleration response a) at sensor A b) at sensor B.....	170
Figure (6.24):	Cross-correlation coefficient of filtered acceleration response to transient force ($B = 2\pi \times 4000 \text{ rad/s}$, $\omega_0 = 2\pi \times 6000 \text{ rad/s}$).	170
Figure (6.25):	Cross-correlation coefficient of filtered acceleration response to transient force ($B = 2\pi \times 2000 \text{ rad/s}$, $\omega_0 = 2\pi \times 3000 \text{ rad/s}$).	171
Figure (6.26):	Beam model for time delay estimation problem: investigation of the effect of propagation path length.....	172
Figure (6.27):	Cross-correlation coefficient of acceleration response $L_p = 8 \text{ m}$...	173
Figure (6.28):	Cross-correlation coefficient of acceleration response $L_p = 16 \text{ m}$.	173
Figure (6.29):	Cross-correlation coefficient of acceleration response $L_p = 20 \text{ m}$.	174
Figure (6.30):	Beam model for time delay estimation problem: investigation of the effect of reflection from boundaries.....	176

Figure (6.31):	Cross-correlation coefficient of acceleration response in a simply supported beam.....	177
Figure (6.32):	First peak of cross-correlation coefficient of acceleration responses: comparison of simply supported beam and infinite beam.....	178
Figure (6.33):	Second peak of cross-correlation coefficient of acceleration responses.....	178
Figure (6.34):	Third peak of cross-correlation coefficient of acceleration responses.....	179
Figure (6.35):	Response at sensor A a) acceleration b) noise(R=30%) c) noisy acceleration.....	182
Figure (6.36):	Response at sensor B a) acceleration b) noise(R=30%) c) noisy acceleration.....	183
Figure (6.37):	Autospectral -density -function of noisy acceleration (R=30%) response at a) sensor A b) sensor B.....	183
Figure (6.38):	Cross-correlation coefficient of acceleration response in presence of 30% noise.....	184
Figure (6.39):	Cross-correlation coefficient between noisy acceleration measurements: comparison of the effect of different levels of noise on first peak.....	184
Figure (6.40):	Cross-correlation coefficient between noisy acceleration measurements: comparison of the effect of different levels of noise on second peak	185

Figure (6.41):	Cross-correlation coefficient between noisy acceleration measurements: comparison of the effect of different levels of noise on third peak.....	185
Figure (6.42):	Cross-correlation function between noisy acceleration measurements: comparison of the effect of different levels of noise on first peak.....	186
Figure (6.43):	Cross-correlation function between noisy acceleration measurements: comparison of the effect of different levels of noise on second peak.....	187
Figure (6.44):	Cross-correlation function between noisy acceleration measurements: comparison of the effect of different levels of noise on third peak	187
Figure (6.45):	Beam model for time delay estimation problem: investigation of damage in a beam.....	188
Figure (6.46):	Cross-correlation function of acceleration measurements: comparison of the effect of different damage extent (damage length 2 <i>m</i>).....	190
Figure (6.47):	Cross-correlation function of acceleration measurements: comparison of the effect of different damage extent (damage length 4 <i>m</i>).....	193

Notations

A	Cross-sectional area
B	Bandwidth of the random process
c	Non-dispersive wave speed
\bar{c}	Damping per unit length
c_d	Wave speed in damage area
c_g	Group speed
c_{gd}	Group speed in damage area
c_p	Phase speed
C	Damping matrix
d	Distance
e_t	Finite element length
E	Elasticity modulus
$h(t)$	Impulse response function
$H(\omega)$	Frequency response function
I	Moment of inertia
k	Wavenumber
K	Stiffness matrix
L_d	Damage length
L_p	Propagation path length
$n(t), m(t)$	Extraneous measurement noise
\bar{m}	Mass per unit length

M	Mass matrix
R	Noise level
$R_{xx}(\tau)$	Autocorrelation function
$R_{xy}(\tau)$	Cross-correlation function
s	Damage extent
$s(t), r(t)$	Clean measurement
$S_{xx}(\omega)$	Autospectral density function
$\mathcal{S}_{xx}(\omega)$	Auto-energy spectral density function
$S_{xy}(\omega)$	Cross-spectral density function
$\mathcal{S}_{xy}(\omega)$	Cross-energy spectral density function
$\{x_k\}, \{y_k\}$	Random process
$z(t)$	Analytical function
α	Attenuation factor
ζ	Damping ratio
λ	Wavelength
μ	Mean of random process
$\rho_{xy}(\tau)$	Cross-correlation coefficient
σ^2	Variance of the random process
τ	Time delay
ψ^2	Mean square value of the random process
ω	Frequency

Chapter 1

Introduction

1.1 General

The process of periodic or continuous inspection of the safety and functionality of a structure and the tests performed in order to understand the behavior mechanisms of structures are commonly referred to as Structural Health Monitoring (SHM) (Farrar and Sohn, 2001). SHM is an interdisciplinary field of research that involves a broad range of disciplines such as structural, material, computer and communications engineering (Mufti, 2001). SHM process consists of several tasks that can be summarized in seven steps (Mufti, 2001):

1. Acquisition of Data
2. Communication of Data
3. Processing of Data
4. Storage of Processed Data
5. Extraction of Appropriate Information from Data (Diagnostics)
6. Retrieval of Data

The most important step of this inspection process is the *diagnostics* step that includes extraction of useful information from stored data e.g. any information about the presence of damage in structure. This process is generally referred to as *damage detection*.

Generally structural damage is any undesirable change in a structure that causes a negative effect on its serviceability (Amin, 2002). The damages in civil engineering structures are in the form of cracks, reinforcement fracture, delamination, broken welds, loose bolts, corrosion, etc (Amin, 2002). The detection procedure for such damages can be classified into four levels (Rytter, 1993):

- Level 1: Determination that damage is present in the structure.
- Level 2: Level 1 plus determination of the geometric location of the damage.
- Level 3: Level 2 plus quantification of the severity of the damage.
- Level 4: Level 3 plus prediction of the remaining service life of the structure.

Damage detection methods can be grouped in various categories:

- (1) Destructive Evaluation Methods
- (2) Non-Destructive Evaluation Methods
- (3) Vibration Based Damage Identification Methods

1. Destructive Evaluation Methods

Destructive evaluation methods are those in which the entire structure or a part of it is destroyed after the evaluation is performed. Extracting core samples for testing from a structure and testing of the structure under the application of design load are examples of

methods that belong to this category. These methods are costly and generally impractical for the structures which are under service.

2. Non-Destructive Evaluation Methods (NDE Methods)

In these methods the physical condition of the known damaged area of the structure is interrogated directly by measurement. This measurement can be done in three ways:

- Visual inspection
- Static field test
- Instrumental evaluation method

Common NDE methods include ultrasonic, acoustic, X-ray and magnetic field tests.

There are several limitations associated with the NDE methods (Xu, 2005):

- The damage area must be known.
- The damage area should be accessible.
- Some types of damages cannot be identified by this method.
- It is difficult to evaluate the extent of damage.

For the foregoing reasons, application of NDE methods may become too expensive or impractical. Hence, Vibration Based Damage Identification (VBDI) methods are now being considered as alternative methods for the identification of damage. One of the major differences of these methods with NDE methods is that in VBDI techniques the damage is identified in a global sense by inspection of global parameters while in NDE methods evaluation of local parameters leads to detection of local damages.

3. Vibration Based Damage Identification Methods (VBDI Methods)

The aforementioned drawbacks of the NDE methods have led to the development of global detection methods. In these methods, vibration signals are measured by sensors installed on the structure. These measured structural signals are processed in order to identify the vibration signatures of the structure. Any change in these signatures can be used as a tool to infer structural damage. In the next section a literature survey of the VBDI methods is presented.

1.2 Literature Survey of Vibration Based Damage Identification Methods

Vibration based damage identification methods are classified into the following two categories (Doebling et al., 1998):

1. Model-based approaches
2. Data-driven approaches

1. Model-based approaches

Traditional approaches in this category examine the changes in modal parameters as indicators of damage. Examples of such modal parameters or quantities derived from these modal parameters are (Humar et al., 2006):

- Frequency
- Mode Shape
- Mode Shape Curvatures

- Strain Energy
- Physical Property Matrices

These parameters are extracted from both undamaged and damaged structures. The difference between the values of these parameters for the two cases relates to a change in the physical properties of structures such as mass, damping and stiffness. Damage can be inferred based on this comparison. In general, an analytical model of the structure must be developed to achieve this. A thorough survey of these approaches and their application can be found in Humar et al. (2006), Chang (2001, 2003) and Doebling et al. (1996, 1998). These traditional approaches are still not widely accepted for the following reasons (Salvino et al., 2005):

1. Insensitivity to localized damage
2. Linearity assumptions
3. Sensitivity to sensor locations
4. Sensitivity to environmental effects

Recently data assimilation techniques Such as extended Kalman filter and ensemble Kalman are used for the detection of damage. Relevant examples can be found in Yang et al. (2006) and Ghanem and Ferro (2006). One of the important features of these techniques is the capability to tackle non-linear problems.

2. Data-driven approaches

In the approaches discussed earlier, the measured signals are fitted to a specific mathematical model. These mathematical models may not successfully capture the true complexity of the structure (Salvino et al., 2005). Hence, the data-driven approaches have

recently attracted considerable interest. These methods are based on structural parameters that are extracted directly from the measurements. The parameters are extracted for both undamaged and damaged structure. Comparison between the parameter values in the two states leads to the identification of damage.

A number of approaches have been reported in data-driven category, notably, studies of Lamb wave, electro-mechanical impedance, and electrical resistance (Yang et al., 2007). Some of these approaches exploit signal processing tools such as wavelet analysis (Hera and Hou, 2004, Staszewski, 1998) and Hilbert –Huang transform (Pines and Salvino, 2006). Pines and Salvino (2006) use the difference of instantaneous phase function between two successive degrees of freedom to infer damage. In this approach it is assumed that damage changes the wave speed and consequently the time delay between two measurements of the structural elements. This time delay shift, induced by damage, will be reflected on the instantaneous phase function of the two degrees of freedom of the structural element.

In the present study, the time delay is directly estimated by the application of cross-correlation analysis. Based on this estimation, the wave speeds in intact and damaged structures are compared to detect damage. Yang et al. (2007) have also used cross-correlation analysis for damage detection, but in the approach presented in this work, any change in the amplitude of cross-correlation reveals a change in the dynamic properties.

Time delay estimation is a challenging problem, which has attracted considerable attention for more than three decades. Winter and Bies (1962) examined the applicability of cross-correlation analysis for speed detection in long thin bars excited by broad band

random process. In contrast, Novikov (1962) investigated the estimation of flexural wave speed in a beam subjected to narrow-band force. White (1969) showed the efficiency of cross-correlation analysis for time delay estimation in both non-dispersive and dispersive wave media.

1.3 The Proposed Approach for Damage Detection

In structural engineering, there are two kinds of one dimensional waveguides: The first types of waveguides are rods. They conduct longitudinal waves, which are examples of non-dispersive waves. The speed of longitudinal waves in rods depends on its physical properties. Hence any change in the physical properties of the rod, such as axial stiffness, will be reflected in the speed of axial wave.

The second types of waveguides are beams. They conduct flexural waves, which are examples of dispersive waves. The speed of flexural waves relates to the physical properties of the medium and the excitation frequency. Stated differently, any change in the physical properties of the beam affect the flexural wave speed of a specific band of frequencies.

The general idea of the proposed approach lies in the estimation of wave speed in the waveguides (i.e. rod or beam) before and after the introduction of damage. Consider an undamaged waveguide, in which measurement sensors are installed at two locations the distance between which is known. If the time delay of propagation between these two locations can be estimated, the ratio of the distance by the time delay results in the estimation of the wave speed in undamaged structure (In this study cross-correlation

analysis is used to estimate the time delay). The estimated wave speed in undamaged waveguide will be considered as a basis for the comparison with the wave speed in damaged waveguide.

Once damage occurs, the time delay will be calculated for the damaged waveguide by using the cross-correlation analysis. This time delay consists of two parts:

1. The first part of this time delay relates to the portion of the structure which is subjected to damage. The ratio of the length of this portion and the wave speed in the damaged area provides the estimate of the time delay corresponding to the damaged part.
2. The second part of this time delay refers to the portion of the structure that is a part of propagation path but it is undamaged. So, the ration of this length and the wave speed in intact waveguide, defines the other part of time delay. If the damage length is known, this part can be calculated easily as the ratio of the undamaged length and the corresponding wave speed.

In order to estimate each of the two aforementioned parts of the time delay, the damage length should be known. Here two cases are considered:

Case 1: known damage length:

It is assumed here that the damage length can be estimated roughly before the analysis is carried out. In a known propagation path in a one dimensional waveguide, the corresponding undamaged length can be easily calculated.

Case 2: unknown damage length:

When a prior estimation of damage length is difficult, it is assumed that the entire propagation path of the wave is damaged (i.e. the second part of time delay discussed earlier is neglected). Hence it is assumed that wave travels the entire propagation path with the speed of damaged area. Obviously this is a crude approximation which can only serve as the first guess. For greater precision in identifying the damage location and the extent of damage more sensors at closer spacing would be needed.

Based on these assumptions, the wave speed in the damaged length can be evaluated. Comparison of this wave speed with that of the intact waveguide would provide the estimate of damage extent. It is worth mentioning that the estimated damage extent when the damage length is unknown leads to only an average estimation of damage severity as the entire path is as assumed to be damaged.

In summary, the proposed approach consists of the following steps:

Step 1:

In undamaged waveguide, the time delay between any response quantities (e.g. acceleration, velocity) of two measurement location can be estimated. From this time delay, the wave speed (axial or flexural) is calculated.

Step 2:

In damaged waveguide, the time delay of the same response is evaluated. An estimate of the damage length is obtained on the basis of measurements at two or more stations. The accuracy of this estimate depends on the number of measurement locations. Based on the

estimate of damage length, the wave speed in damaged portion of the waveguide is calculated.

Step 3:

The calculated wave speeds are compared and the extent of damage is estimated.

As mentioned previously, cross-correlation analysis is used to estimate the time delay. This methodology is explained in detail in Chapter 4 for both non-dispersive and dispersive wave propagation.

Finally, it should be mentioned that in the proposed approach a local parameter, namely wave speed, is used to infer local damages; therefore in this sense, the proposed approach can be considered as a non-destructive evaluation method. On the other hand, since the analysis is carried out on measured dynamic response of the structure, it can be considered as a VBDI technique.

1.4 Objectives of the Present Study

The objectives of the current investigation are as follow:

1. Efficiency of cross-correlation analysis for time delay estimation in non-dispersive and dispersive waveguides through numerical simulation.

In this study both analytical and numerical solutions for one dimensional wave propagation is considered to examine the efficiency of cross-correlation analysis for time delay estimation in structural waveguides.

2. Cross-correlation analysis for time delay estimation for stationary random and deterministic transient excitations.

The efficiency of cross-correlation analysis is studied for different types of excitations, namely stationary narrow and broad band random and transient excitations. The frequency selective filter design, as required for dispersive wave propagation, is considered.

3. The effect of reflected waves on cross-correlation analysis.

For both non-dispersive and dispersive waveguides, FEM models are constructed that permit simulation of different boundary conditions. The effects of different boundary conditions on time delay estimation are investigated in details.

4. Influence of measurement noise on cross-correlation analysis.

In order to study the feasibility of time delay estimation procedure in practice, the effects of the magnitudes of measurement noise are examined in depth.

5. Applicability of time delay estimation in damage detection for structural health monitoring.

Once the efficiency of cross-correlation analysis is validated, it is used for damage detection in non-dispersive and dispersive waveguides for different scenarios including damage location, damage extent and damage length.

1.5 Layout of the Thesis

The outline of thesis is as follows:

Chapter (1): It begins with the introduction of structural health monitoring. A literature survey on vibration based damage identification is presented. The proposed approach to damage detection is briefly described and the objectives of the study are presented.

Chapter (2): It includes theoretical background to random dynamical systems. The concept of cross-correlation function is elucidated. The relationships between random inputs and outputs of a linear system are derived

Chapter (3): It consists of mathematical derivation of cross-correlation coefficient for time delay estimation in non-dispersive and dispersive wave propagation paths. The derivation considers both narrow-band and broad-band force.

Chapter (4): It describes the analytical and FEM solutions of elementary rod equation. The spectral solution of Bernoulli-Euler beam is derived and the concepts of phase speed and group speed is introduced. Next, FEM solution of the beam is presented. Numerical implementation of both analytical solution in frequency domain and the time domain based FEM solution are described.

Chapter (5): It details the numerical illustration of cross-correlation analysis for time delay estimation in non-dispersive waveguide modeled by a rod. The model is validated by contrasting analytical solution with FEM solution. This model is used to examine the efficiency of cross-correlation analysis under different conditions i.e. different types of loadings, reflection from the boundaries and presence of noise. The analysis described in this study constitutes the basis for damage detection in non-dispersive waveguide.

Chapter (6): It begins with contrasting a frequency domain based analytical solution with FEM model. Next, the acceleration measurements of the bending waves in beam are used to estimate the time delay between two sensor locations. A parametric numerical study is conducted considering different types of excitations, wave propagation path length, presence of different boundary conditions and the effects of measurement noise levels. Finally the time delay estimation is used damage detection in dispersive waveguides.

Chapter (7): It summarizes the features of the current investigation culminating in conclusions and possible future research directions.

Chapter 2

Random Dynamical System

2.1 Introduction

The approach for structural health monitoring developed in this work relies on the estimation of time delay in the propagation of waves in a non-dispersive or dispersive travel path. Time delay estimates are closely linked to the many basic concepts of random dynamic analysis and in particular to correlation studies. Although such concepts are well known and are described in standard texts, it is useful to present a summary of those concepts that are relevant to this study, both for the sake of completeness and for ease of reference when their applications are presented in the subsequent chapters.

In this chapter, a brief introduction to random dynamical system is presented. The concepts of random processes are introduced and autocorrelation and cross-correlation functions of two stationary random processes are described. Next, some important characteristics of an ideal linear system are briefly mentioned. For the steady state, the relationship between input and output processes is described in details. A similar relationship between input and output of the system is also provided for transient case.

The subsequent sections of this chapter closely follow the references Bendat and Piersol (1986), Bendat (1958), Bendat and Piersol (1993) and Bendat (1985).

2.2 Random Data Analysis

2.2.1 Random Process

A random process (also called a time-series or a stochastic process) represents an ensemble of time functions $\{x_k(t)\}$, $-\infty < t < \infty$, $k=1, 2, 3, \dots$, where the ensemble is characterized through statistical properties (Bendat and Piersol, 1986).

2.2.2 Stationary Random Process

The stationarity of a random process $\{x_k(t)\}$ can be described in two senses (Huang et al., 1998):

- Weak sense stationarity
- Strict sense stationarity

1. *Weakly stationary random process*

A random process $\{x_k(t)\}$ is stationary in a weak sense if, for all t

$$E(|x_k(t)|^2) < \infty \quad (2.1)$$

$$E(x_k(t)) = m \quad (2.2)$$

$$\begin{aligned}
C(x_k(t_1), x_k(t_2)) &= C(x_k(t_1 + \tau), x_k(t_2 + \tau)) \\
&= C_{xx}(t_2 - t_1)
\end{aligned}
\tag{2.3}$$

where E is the expected value defined as the ensemble average of the quantity, and C is the covariance function.

2. Strictly stationary random process

A random process $\{x_k(t)\}$ is strictly stationary if, for all t_i and τ , the joint probability density function of $[x_k(t_1), x_k(t_2), \dots, x_k(t_n)]$ and $[x_k(t_1 + \tau), x_k(t_2 + \tau), \dots, x_k(t_n + \tau)]$ are the same.

2.2.3 Autocorrelation Function

For the stationary random process $\{x_k(t)\}$, the autocorrelation function is defined as

$$R_{xx}(\tau) = E[x_k(t)x_k(t + \tau)] \tag{2.4}$$

where E refers to the expected value of the associated random variable. The autocorrelation function of a stationary random process has two important properties:

- *Autocorrelation function is an even function.*

This property can be proved as follows:

$$R_{xx}(-\tau) = E[x_k(t)x_k(t - \tau)] \tag{2.5}$$

Due to stationarity of $x_k(t)$, one can replace t by $t + \tau$ in the above equation to obtain

$$R_{xx}(-\tau) = E[x_k(t + \tau)x_k(t + \tau - \tau)]. \quad (2.6)$$

Using Equation (2.6), the following relationships can be obtained as

$$\begin{aligned} R_{xx}(-\tau) &= E[x_k(t + \tau)x_k(t)] = E[x_k(t)x_k(t + \tau)] \\ &= R_{xx}(\tau) \end{aligned} \quad (2.7)$$

- *The autocorrelation function always has a peak at $\tau = 0$.*

This property will be proved in Section 2.2.4.

The Fourier transform of the autocorrelation function is called the *autospectral density function* and is defined as:

$$S_{xx}(\omega) = \frac{1}{2\pi} \int_{-\infty}^{+\infty} R_{xx}(\tau) e^{-i\omega\tau} d\tau \quad (2.8)$$

It is worth mentioning that $S_{xx}(\omega)$ is real and even. Next, the autocorrelation functions for two types of random processes are described (Bendat, 1985):

- I. Narrow-band white random process
- II. Broad-band white random process

I. Narrow-Band White Random Process

The autospectral density function of narrow-band white random process is defined as

$$S_{xx}(\omega) = \begin{cases} \frac{K}{2} & |\omega \pm \omega_0| \leq \frac{B}{2} \\ 0 & \text{otherwise} \end{cases} \quad (2.9)$$

where $\frac{K}{2}$ is the amplitude spectrum, ω_0 is the central frequency and B is the bandwidth.

The autospectral density function given by Equation (2.9) is plotted in Figure (2.1).

Using Equation (2.8), the autocorrelation function can be derived from autospectral density function as

$$R_{xx}(\tau) = \int_{-\infty}^{+\infty} S_{xx}(\omega) e^{i\omega\tau} d\omega = 2 \int_{\omega_0 - \frac{B}{2}}^{\omega_0 + \frac{B}{2}} \frac{K}{2} \cos \omega\tau d\omega \quad (2.10)$$

or

$$R_{xx}(\tau) = KB \frac{\sin\left(\frac{B\tau}{2}\right)}{\left(\frac{B\tau}{2}\right)} \cos \omega_0\tau \quad (2.11)$$

The autocorrelation of narrow-band white random process is shown in Figure (2.2).

Notice from the figure that the autocorrelation function is symmetric with respect to $\tau = 0$ and also has a peak at $\tau = 0$.

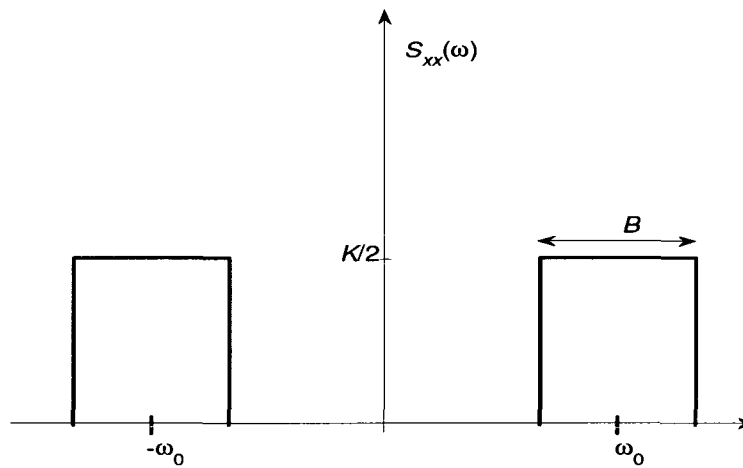


Figure (2.1): Autospectral density function of narrow-band white random process

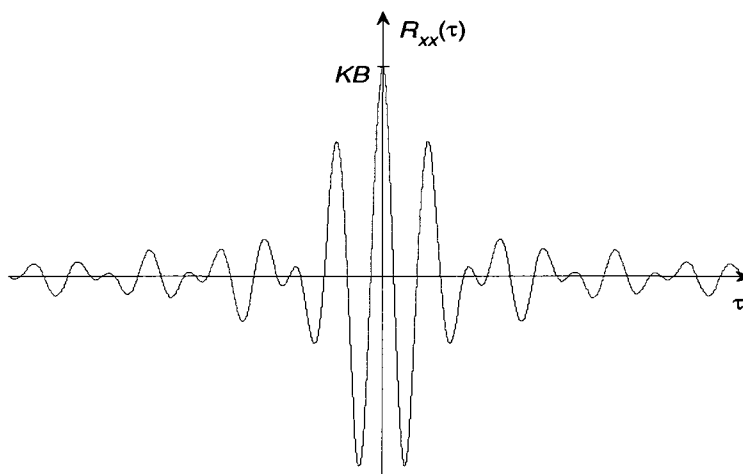


Figure (2.2): Autocorrelation function of narrow-band white random process

II. Broad-Band White Random Process

The autospectral density function of a broad-band white random process is given by

$$S_{xx}(\omega) = \begin{cases} \frac{K}{2} & |\omega| \leq B \\ 0 & \text{Otherwise} \end{cases} \quad (2.12)$$

The autospectral density function of broad-band white random process is presented in Figure (2.3). Using Equation (2.8), the autocorrelation function for broad-band white random process can be derived as

$$\begin{aligned} R_{xx}(\tau) &= \int_{-\infty}^{+\infty} S_{xx}(\omega) e^{i\omega\tau} d\omega \\ &= 2 \int_0^B \frac{K}{2} \cos \omega\tau d\omega = KB \frac{\sin B\tau}{B\tau} \end{aligned} \quad (2.13)$$

Figure (2.4) shows the autocorrelation function of broad-band white random process. The peak of this function, similar to narrow-band white random process, occurs at $\tau = 0$. Comparison of Figure (2.2) and Figure (2.4) reveals that the peak in the broad-band case is more distinct than the narrow-band case. The broader the band is, the sharper the peak is in autocorrelation function. Note that $\{x_k(t)\}$ and $\{x_k(t + \tau)\}$ are uncorrelated at $\tau = \frac{n\pi}{B}, n = 1, 2, \dots$.

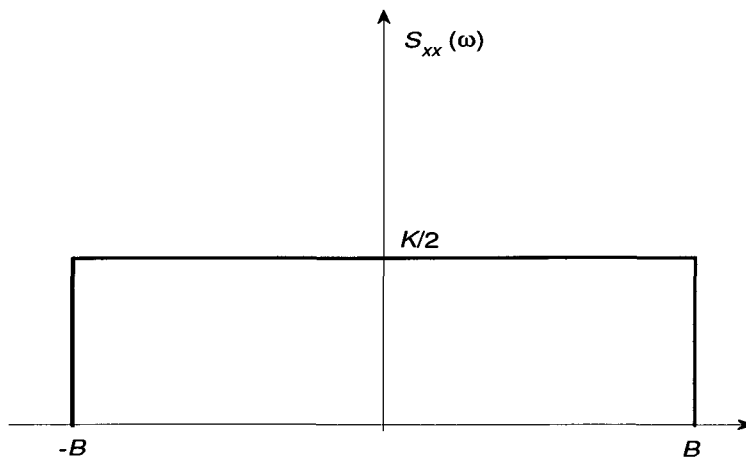


Figure (2.3): Autospectral density function for broad-band white random process

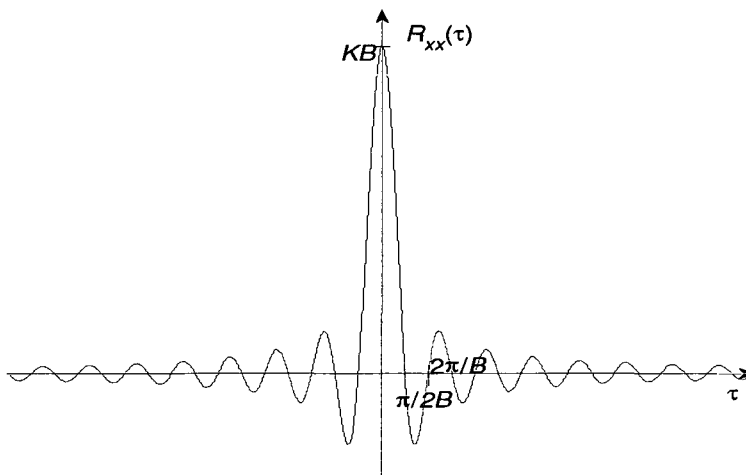


Figure (2.4): Autocorrelation function of broad-band white random process

2.2.4 Cross-Correlation Function

The cross-correlation function of the two stationary random processes $\{x_k(t)\}$ and $\{y_k(t)\}$ is given by:

$$R_{xy}(\tau) = E[x_k(t)y_k(t + \tau)] \quad (2.14)$$

The cross-spectral density function is defined as the Fourier transform of the cross-correlation function:

$$S_{xy}(\omega) = \frac{1}{2\pi} \int_{-\infty}^{+\infty} R_{xy}(\tau) e^{-i\omega\tau} d\tau \quad (2.15)$$

An important feature of the cross-correlation of two random processes is called the *cross-correlation inequality*, given by

$$|R_{xy}(\tau)|^2 \leq R_{xx}(0)R_{yy}(0) \quad (2.16)$$

This relationship is proved in the following (Bendat and Piersol, 1986):

For any real constants a and b the expected value $E[(ax(t) + by(t + \tau))^2]$ is always non-negative. Expanding this equation leads to

$$a^2R_{xx}(0) + 2abR_{xy}(\tau) + b^2R_{yy}(0) \geq 0 \quad (2.17)$$

The rearrangement of Equation (2.17) gives the following quadratic equation in (a/b) with $(b \neq 0)$

$$\left(\frac{a}{b}\right)^2 R_{xx}(0) + 2\left(\frac{a}{b}\right)R_{xy}(\tau) + R_{yy}(0) \geq 0 \quad (2.18)$$

Since this quadratic equation is always non-negative, its discriminant should be non-positive, leading to

$$4R_{xy}^2(\tau) - 4R_{xx}(0)R_{yy}(0) \leq 0 \quad (2.19)$$

Thus

$$R_{xy}^2(\tau) = |R_{xy}(\tau)|^2 \leq R_{xx}(0)R_{yy}(0) \quad (2.20)$$

Considering $\{x_k(t)\} = \{y_k(t)\}$, the special case of cross-correlation inequality leads to the *autocorrelation inequality*

$$|R_{xx}(\tau)| \leq R_{xx}(0) \quad (2.21)$$

Equation (2.21) proves one of the properties of autocorrelation function pointed out in Section (2.2.3). It states the fact that the autocorrelation function always has a peak at $\tau = 0$. It is also worth mentioning that $R_{xx}(\tau = 0)$ is the mean square value of the random process $\{x_k(t)\}$, one obtains

$$R_{xx}(0) = \psi_x^2 = \mu_x^2 + \sigma_x^2 \quad (2.22)$$

where μ_x and σ_x^2 are respectively the mean and variance of the process $\{x_k(t)\}$.

2.2.5 Cross-Correlation Coefficient

For zero mean random processes, cross-correlation inequality gives rise to a coefficient that is commonly called *cross-correlation coefficient* defined by

$$\rho_{xy}(\tau) = \frac{R_{xy}(\tau)}{\sqrt{R_{xx}(0)}\sqrt{R_{yy}(0)}} \quad (2.23)$$

On referring to Equation (2.22), one obtains

$$\rho_{xy}(\tau) = \frac{R_{xy}(\tau)}{\sigma_x \sigma_y} \quad (2.24)$$

where $|\rho_{xy}(\tau)| \leq 1$ for all τ . As mentioned before, both Equations (2.23) and (2.24) are valid only when $\{x_k(t)\}$ and $\{y_k(t)\}$ are zero mean stationary random processes. For non-zero mean processes, general form of cross-correlation coefficient is expressed as

$$\rho_{xy}(\tau) = \frac{R_{xy}(\tau) - \mu_x \mu_y}{(R_{xx}(0) - \mu_x^2)^{1/2} (R_{yy}(0) - \mu_y^2)^{1/2}} \quad (2.25)$$

where μ_x and μ_y are the mean values of random processes $\{x_k(t)\}$ and $\{y_k(t)\}$, respectively.

2.3 Single Input/Single Output Relationships

2.3.1 Ideal Dynamical System

In this study, the system is assumed to be an ideal system with the *impulse response function* $h(t)$. An ideal system is a system with four properties (Bendat and Piersol, 1993):

1. **Stable**

A system is called stable if for every bounded input, the output is bounded.

2. **Causal**

A system is causal if the output does not depend on the future value of input i.e. the output depends only on the input values up to the current time.

3. **Time-invariant**

A system is time-invariant if the output does not depend on the time at which the input is applied.

4. **Linear**

A system is linear if it satisfies *superposition rule*.

If $x(t)$ and $y(t)$ are the input and the corresponding output from an ideal system respectively, their relationship is given by the convolution integral as

$$y(t) = \int_{-\infty}^{+\infty} h(\tau)x(t - \tau) d\tau \quad (2.26)$$

Due to casual property, one obtains

$$y(t) = \int_0^{+\infty} h(\tau)x(t - \tau) d\tau \quad (2.27)$$

The *frequency response function* $H(\omega)$ of an ideal system is defined as the Fourier transform of the impulse response function and is given by

$$H(\omega) = \frac{1}{2\pi} \int_{-\infty}^{+\infty} h(t) e^{-i\omega t} dt \quad (2.28)$$

Taking the Fourier transform of Equation (2.26), the frequency domain relationship between the input and output of an ideal system is given by

$$Y(\omega) = H(\omega)X(\omega) \quad (2.29)$$

In general the Frequency Response Function (FRF) is complex valued function. FRF can be represented in the polar notation as a product of the amplitude and phase function as:

$$H(\omega) = |H(\omega)|e^{-i\phi(\omega)} \quad (2.30)$$

Figure (2.5) shows an ideal single input/single output system.

2.3.2 Stationary Input

In order to investigate the applications of the concepts discussed in the previous section, consider that the input $x(t)$ and the output $y(t)$ are the samples of stationary random processes $\{x_k(t)\}$ and $\{y_k(t)\}$. According to Equation (2.27), one can write (Bendat and Piersol, 1993)

$$y(t + \tau) = \int_0^{+\infty} h(\xi)x(t + \tau - \xi) d\xi \quad (2.31)$$

Multiplying both sides by $x(t)$ in Equation (2.31), one obtains

$$x(t)y(t + \tau) = \int_0^{+\infty} h(\xi)x(t)x(t + \tau - \xi) d\xi \quad (2.32)$$

Taking the expected values of both sides gives rise to an important relation called *input/output cross-correlation relation*

$$R_{xy}(\tau) = \int_0^{+\infty} h(\xi)R_{xx}(\tau - \xi) d\xi \quad (2.33)$$

Equation (2.33) is a convolution integral. Fourier transform of Equation (2.33) leads to another important relationship called *input/output cross-spectral relation*

$$S_{xy}(\omega) = H(\omega)S_{xx}(\omega) \quad (2.34)$$

Further, it can easily be proved that

$$S_{yy}(\omega) = H^*(\omega)S_{xy}(\omega) = |H(\omega)|^2S_{xx}(\omega) \quad (2.35)$$

where (*) denote the complex conjugate operation

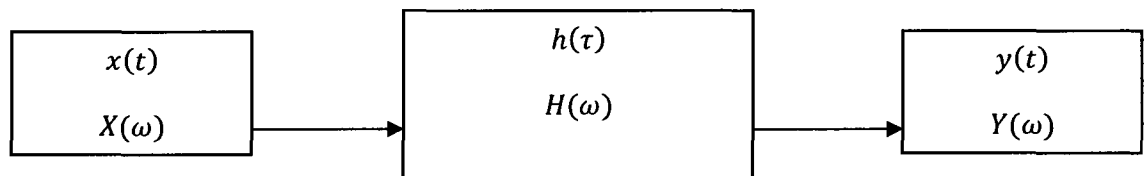


Figure (2.5): An ideal single input/single output system

2.3.3 Transient Input

The input/output relationships for stationary case can be directly extended to tackle transient cases. Instead of using autospectral and cross-spectral density functions, energy spectral functions are considered and defined as (Bendat and Piersol, 1993)

$$S_{xx}(\omega) = TS_{xx}(\omega) \quad (2.36)$$

$$\mathcal{S}_{yy}(\omega) = T\mathcal{S}_{yy}(\omega) \quad (2.37)$$

where $\mathcal{S}_{xx}(\omega)$ and $\mathcal{S}_{yy}(\omega)$ are auto-energy spectral density functions of the transient records $x(t)$ and $y(t)$ for the duration of T . For cross-energy spectral density function $\mathcal{S}_{xy}(\omega)$, the following relationships exist

$$\mathcal{S}_{xy}(\omega) = T\mathcal{S}_{xy}(\omega) \quad \omega > 0 \quad (2.38)$$

$$\mathcal{S}_{xy}(\omega) = \mathcal{S}_{xy}^*(-\omega) \quad \omega < 0 \quad (2.39)$$

By a process similar to that used in deriving Equations (2.34) and (2.35), one obtains

$$\mathcal{S}_{xy}(\omega) = H(\omega)\mathcal{S}_{xx}(\omega) \quad (2.40)$$

$$\mathcal{S}_{yy}(\omega) = H^*(\omega)\mathcal{S}_{xy}(\omega) = |H(\omega)|^2\mathcal{S}_{xx}(\omega) \quad (2.41)$$

It should be mentioned that for simplicity, all the expressions presented in this chapter are for continuous input and output obtained from a continuous system. Since in practical problems, only discrete data are available, the discrete versions of all aforementioned expressions can be obtained using discrete operators such as Fast Fourier Transform (FFT).

Chapter 3

Time Delay Estimation and Path Identification

3.1 Introduction

The procedure of estimating the time that it takes a wave to travel a specific distance along its propagation path is commonly referred to as Time Delay Estimation. Time delay estimation arises in a class of engineering problems such as sonar and radar processing, acoustic noise, vibration control engineering and seismic data processing related to oil reservoir modeling etc. The time delay estimation techniques are developed to tackle wave propagation through both non-dispersive and dispersive media. The relevant characteristics of non-dispersive and dispersive waves are explained in the subsequent chapters in the details.

The correlation techniques detailed in the previous chapter are extensively used for time delay estimation when measured input and output are corrupted by measurement noise. The first part of this chapter is therefore devoted to the application of cross-correlation analysis for time delay estimation of non-dispersive waves while the second part covers the analysis for a dispersive path. The subsequent sections of this chapter closely follow

the references Bendat and Piersol (1993), Bendat (1985), Bendat and Piersol (1986) and White (1969).

3.2 Non-Dispersive Propagation Path Identification

3.2.1 Noise Free Case

For certain type of wave propagation problems, the speed of wave does not depend on its frequency. This type of wave propagation is referred as to *Non-dispersive wave propagation*. Because the wave speed does not depend on the frequency, the waveform does not change its shape during propagation. As a result for any input applied to a non-dispersive medium, the corresponding output is merely a delayed and attenuated version of the input. Mathematically, this phenomenon can be represented as

$$y(t) = \alpha x(t - \tau) \quad (3.1)$$

where $x(t)$ is the input (transmitted signal), $y(t)$ is the output (received signal), α is the attenuation factor and τ is the time delay between the input and output waves. Note that both α and τ are assumed to be independent of frequency. The time delay τ can be represented in terms of distance between the measurement locations of $x(t)$ and $y(t)$, and the wave speed, so that

$$\tau = \frac{d}{c} \quad (3.2)$$

where d is the distance and c is the wave speed. The methodology to estimate the time delay τ is commonly referred to as *time delay estimation*. When the dynamic characteristics of the system are well known, the estimation of time delay provides an estimate of the length of propagation path. On the other hand, when the propagation path is known, time delay estimation reveals the dynamic characteristics of the system. As alluded previously, the correlation analysis is extensively used for time delay estimation as detailed next.

Using Equation (3.1) the cross-correlation between the input and output is given by

$$\begin{aligned} R_{xy}(\tau) &= E[x(t)y(t + \tau)] = E[(x(t))(\alpha x(t + \tau - \tau_0))] \\ &= \alpha E[x(t)x(t + \tau - \tau_0)] \end{aligned} \quad (3.3)$$

which gives

$$R_{xy}(\tau) = \alpha R_{xx}(\tau - \tau_0) \quad (3.4)$$

This relationship shows that $R_{xy}(\tau)$ is similar to the autocorrelation function $R_{xx}(\tau)$, but delayed by τ_0 and attenuated by α . Calculation of the cross-correlation function at $\tau = \tau_0$ results in

$$R_{xy}(\tau_0) = \alpha R_{xx}(0) \quad (3.5)$$

Since autocorrelation function peaks at $\tau = 0$ (based on autocorrelation inequality of Equation (2.21)), the cross-correlation function will also peak at $\tau = \tau_0$. Assuming that $x_k(t)$ and $y_k(t)$ are zero mean random processes, normalization of Equation (3.4) by the mean square values of these processes gives the cross-correlation coefficient described in Section (2.2.5),

$$\rho_{xy}(\tau) = \frac{\alpha R_{xx}(\tau - \tau_0)}{\sqrt{R_{xx}(0)}\sqrt{R_{yy}(0)}} = \frac{\alpha R_{xx}(\tau - \tau_0)}{\sigma_x \sigma_y} \quad (3.6)$$

The autocorrelation of the output $\{y_k(t)\}$ is given by

$$\begin{aligned} R_{yy}(\tau) &= E[y(t)y(t + \tau)] \\ &= E[(\alpha x(t - \tau_0))(\alpha x(t + \tau - \tau_0))] \\ &= \alpha^2 E[x(t - \tau_0)x(t + \tau - \tau_0)] = \alpha^2 R_{xx}(\tau) \end{aligned} \quad (3.7)$$

In summary, it can be stated that:

The cross-correlation coefficient function between two measurements along a non-dispersive propagation path has a peak that identifies the time needed for the wave to travel the distance between these measurement locations.

In order to have a distinct peak in the cross-correlation function, it is necessary that the waves have acceptable bandwidth. However, in most cases, correlation analysis of non-

dispersive wave propagation has a distinct peak from which the time delay can be readily detected. For detailed investigation of the important features of the cross-correlation coefficient, two types of random processes are considered:

- I. Narrow-band white random process
- II. Broad-band white random process

I. Narrow-Band White Random Process

As discussed in Section 2.2.3, the autocorrelation of a narrow-band white random input $\{x_k(t)\}$, is given by

$$R_{xx}(\tau) = KB \frac{\sin\left(\frac{B\tau}{2}\right)}{\left(\frac{B\tau}{2}\right)} \cos \omega_0 \tau \quad (3.8)$$

Applying Equation (3.4), one obtains

$$R_{xy}(\tau) = \alpha KB \frac{\sin\left(\frac{B(\tau - \tau_0)}{2}\right)}{\left(\frac{B(\tau - \tau_0)}{2}\right)} \cos \omega_0(\tau - \tau_0) \quad (3.9)$$

$$R_{xx}(0) = KB \quad (3.10)$$

$$R_{yy}(0) = \alpha^2 KB \quad (3.11)$$

Substitution in Equation (3.6) yields

$$\rho_{xy}(\tau) = \frac{\sin\left(\frac{B(\tau - \tau_0)}{2}\right)}{\left(\frac{B(\tau - \tau_0)}{2}\right)} \cos \omega_0(\tau - \tau_0) \quad (3.12)$$

Figure (3.1) shows the cross-correlation coefficient between a narrow-band white input and the corresponding output for typical non-dispersive waves. There are some interesting features in this figure that are worth mentioning (Bendat and Piersol, 1986):

1. There are two terms in Equation (3.12): $\cos \omega_0(\tau - \tau_0)$ is the carrier function and $\frac{\sin\left(\frac{B(\tau - \tau_0)}{2}\right)}{\left(\frac{B(\tau - \tau_0)}{2}\right)}$ is the modulation function or *envelope* of $\rho_{xy}(\tau)$.
2. The peaks of carrier function occur at $\tau_n = \tau_0 \pm \left(\frac{2\pi n}{\omega_0}\right)$; where n is any integer.
3. At the time delay $\tau_0 = \frac{d}{c}$, the peak value of the cross-correlation coefficient coincides with the peak value of the envelope.

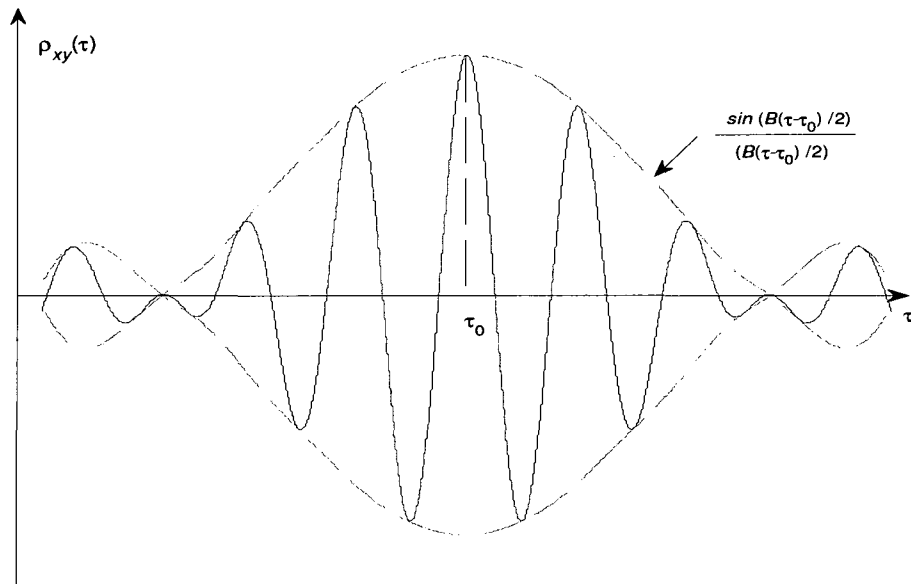


Figure (3.1): Cross-correlation coefficient of narrow-band white input and output of a non-dispersive path

II. *Broad-Band White Random Process*

The autocorrelation of a broad-band white random input $\{x_k(t)\}$ is defined in Equation (2.13) as

$$R_{xx}(\tau) = KB \frac{\sin B\tau}{B\tau} \quad (3.13)$$

Applying Equation (3.4), one obtains

$$R_{xy}(\tau) = \alpha KB \frac{\sin B(\tau - \tau_0)}{B(\tau - \tau_0)} \quad (3.14)$$

$$R_{xx}(0) = KB \quad (3.15)$$

$$R_{yy}(0) = \alpha^2 KB \quad (3.16)$$

Substitution in Equation (3.6) yields

$$\rho_{xy}(\tau) = \frac{\sin B(\tau - \tau_0)}{B(\tau - \tau_0)} \quad (3.17)$$

Cross-correlation coefficient of broad-band input and its output from a non-dispersive path is depicted in Figure (3.2). As shown in Equation (3.17), the cross-correlation coefficient is a *sinc* function that has a peak at the time delay $\tau = \tau_0$. Comparison of Figures (3.1) and (3.2) shows that as the bandwidth of the random process becomes wider, the peak in cross-correlation function becomes sharper, and thus the peak detection becomes easier. This property is one of the interesting features of the cross-correlation in non-dispersive wave propagation. As it will be discussed in following sections, this property is not valid for dispersive wave propagation due to the dispersion effect.

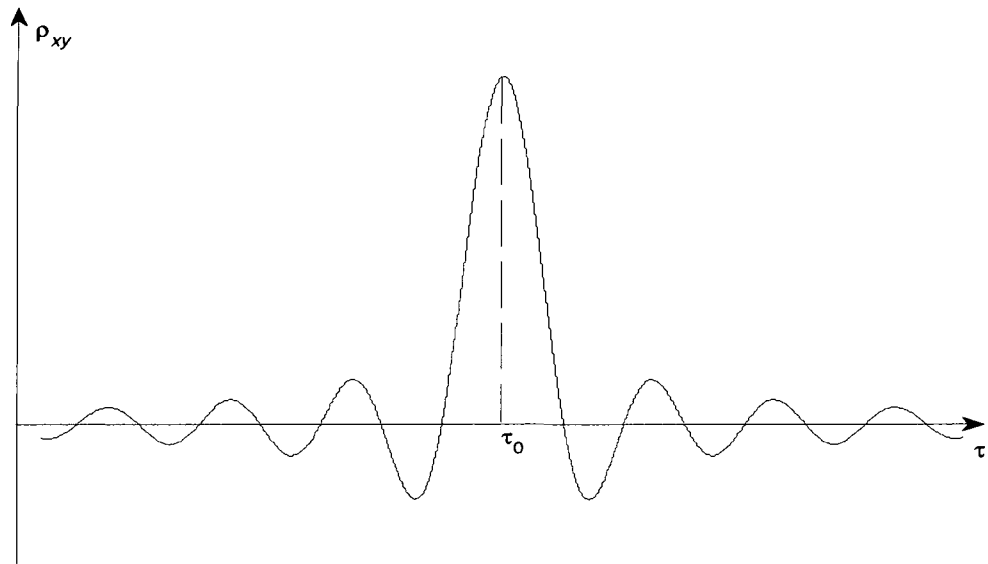


Figure (3.2): Cross-correlation coefficient of broad-band white input and output of a non-dispersive path

3.2.2 Noisy Case

In general, all the measurements are corrupted by noise. In this section the effect of measurement noise in cross-correlation analysis will be investigated (Bendat, 1985).

Assume that $x(t)$ and $y(t)$ are two noisy measured samples of the random processes $\{x_k(t)\}$ and $\{y_k(t)\}$, which represent single input and single output in a non-dispersive propagation path. The two samples can be expressed as

$$x(t) = s(t) + m(t) \quad (3.18)$$

$$y(t) = r(t) + n(t) = \alpha s(t - \tau_0) + n(t) \quad (3.19)$$

in which $s(t)$ and $r(t)$ are clean measurements, and $m(t)$ and $n(t)$ represent the extraneous measurement noise. Cross- correlation of $x(t)$ and $y(t)$ is

$$\begin{aligned} R_{xy}(\tau) &= E[x(t)y(t + \tau)] = \\ &E[(s(t) + m(t))(\alpha s(t + \tau - \tau_0) + n(t + \tau))] \end{aligned} \quad (3.20)$$

or

$$\begin{aligned} R_{xy}(\tau) &= \alpha E[s(t)s(t + \tau - \tau_0)] + E[s(t)n(t + \tau)] \\ &+ \alpha E[s(t + \tau - \tau_0)m(t)] + E[m(t)n(t + \tau)] \end{aligned} \quad (3.21)$$

Assuming that the extraneous noises are uncorrelated to each other and to the clean input, one obtains

$$R_{xy}(\tau) = \alpha E[s(t)s(t + \tau - \tau_0)] = \alpha R_{ss}(\tau - \tau_0) \quad (3.22)$$

This is an interesting result; it shows that if the noises are uncorrelated to each other and to the quantities to be measured, there is no effect of noise in the cross-correlation. On the other hand, the effect of noise appears when the cross-correlation coefficient is obtained; this is because the cross-correlation coefficient depends on mean square value of the

measured quantities. To explore this property, both $R_{xx}(\tau)$ and $R_{yy}(\tau)$ are needed, one obtains

$$\begin{aligned} R_{xx}(\tau) &= E[(s(t) + m(t))(s(t + \tau) + m(t + \tau))] \\ &= R_{ss}(\tau) + R_{mm}(\tau) \end{aligned} \quad (3.23)$$

and

$$\begin{aligned} R_{yy}(\tau) &= E[(\alpha s(t - \tau_0) + n(t))(\alpha s(t + \tau - \tau_0) + n(t \\ &\quad + \tau))] = \alpha^2 R_{ss}(\tau) + R_{nn}(\tau) \end{aligned} \quad (3.24)$$

where $s(t)$, $m(t)$ and $n(t)$ are mutually uncorrelated. The cross-correlation coefficient is now given by

$$\rho_{xy}(\tau) = \frac{\alpha R_{ss}(\tau - \tau_0)}{\sqrt{R_{ss}(0) + R_{mm}(0)} \sqrt{\alpha^2 R_{ss}(0) + R_{nn}(0)}} \quad (3.25)$$

If $s(t)$, $m(t)$ and $n(t)$ have zero mean, one obtains

$$\rho_{xy}(\tau) = \frac{\alpha R_{ss}(\tau - \tau_0)}{\sqrt{\sigma_{ss}^2 + \sigma_{mm}^2} \sqrt{\alpha^2 \sigma_{ss}^2 + \sigma_{nn}^2}} \quad (3.26)$$

where σ_{mm}^2 and σ_{nn}^2 are variances of the measurement noise $m(t)$ and $n(t)$. Clearly $\rho_{xy}(\tau)$ depends on the measurement noise in Equation (3.26). It is worth emphasizing

that the correlation analysis discussed in this section is applicable to other fields of engineering that deal with non-dispersive wave propagation, such as, electromagnetic radiation, longitudinal waves in air, water and structures (Bendat and Piersol, 1993). One example of longitudinal structural wave is axial wave propagation in a rod.

3.3 Dispersive Propagation Path Identification

A type of propagation other than non-dispersive propagation is the so called *dispersive wave propagation*. In dispersive wave propagation, the wave speed depends on the frequency. Let us examine this property by recalling the following relation, which is a model of non-dispersive wave propagation,

$$R_{xy}(\tau) = \alpha R_{xx}(\tau - \tau_0) \quad (3.27)$$

Taking Fourier transform of both sides leads to

$$S_{xy}(\omega) = \frac{1}{2\pi} \int_{-\infty}^{+\infty} \alpha R_{xx}(\tau - \tau_0) e^{-i\omega\tau} d\tau \quad (3.28)$$

Setting $\tau' = \tau - \tau_0$, one obtains

$$S_{xy}(\omega) = \frac{\alpha}{2\pi} \int_{-\infty}^{+\infty} R_{xx}(\tau') e^{-i\omega(\tau'+\tau_0)} d\tau' \quad (3.29)$$

or

$$\begin{aligned}
 S_{xy}(\omega) &= \frac{\alpha}{2\pi} e^{-i\omega\tau_0} \int_{-\infty}^{+\infty} R_{xx}(\tau') e^{-i\omega\tau'} d\tau' \\
 &= \frac{\alpha}{2\pi} e^{-i\omega\tau_0} S_{xx}(\omega)
 \end{aligned} \tag{3.30}$$

Hence FRF is given by

$$H(\omega) = \frac{S_{xy}(\omega)}{S_{xx}(\omega)} = \frac{\alpha}{2\pi} e^{-i\omega\tau_0} \tag{3.31}$$

In polar notations, the FRF is defined as

$$|H(\omega)| = \frac{\alpha}{2\pi} \tag{3.32}$$

$$\phi(\omega) = \omega\tau_0 = \omega \frac{d}{c} \tag{3.33}$$

From Equations (3.32) and (3.33), two important conclusions can be drawn:

1. The amplitude of the FRF of a non-dispersive propagation path is constant and independent of frequency.
2. The phase of the FRF of a non-dispersive propagation path is a linear function of frequency and the constant of proportionality is the time delay.

Unlike non-dispersive waves, the speed of dispersive waves depends on the frequency.

Hence the phase function of the FRF of a dispersive path is a non-linear function of time.

Also, the amplitude of this function depends on frequency. Thus the FRF of a dispersive path can be represented as

$$H(\omega) = \frac{S_{xy}(\omega)}{S_{xx}(\omega)} = A(\omega)e^{-i\varphi(\omega)} \quad (3.34)$$

According to Equation (3.34), each frequency component has different attenuation factor and time delay. This phenomenon introduces some difficulties because when a well defined wave packet propagates, its waveform deforms as it travels through the medium. After some time the wave packet will lose its correlation with the original wave. This property is called *dispersion effect* (White, 1969).

Due to dispersion effect, the cross-correlation of two broad-band waves does not provide any meaningful result. In order to resolve this difficulty, the waves should be filtered within certain band of frequency (Bendat and Piersol, 1993). This bandwidth and the other properties of cross-correlation analysis in dispersive wave propagation are discussed under the following two categories

- I. Narrow-band random process
- II. Broad-band random process

It should be emphasized that the correlation analysis in narrow-band random process closely follows the reference by White (1969).

1. Narrow-band random process

The frequency response function of the dispersive wave propagation is defined as in Equation (3.34), namely,

$$H(\omega) = A(\omega)e^{-i\varphi(\omega)} \quad (3.35)$$

Use of input/output cross-spectrum relation gives

$$S_{xy} = S_{xx}(\omega)H(\omega) = S_{xx}(\omega)A(\omega)e^{-i\varphi(\omega)} \quad (3.36)$$

Hence the cross-correlation is given by

$$\begin{aligned} R_{xy}(\tau) &= \int_{-\infty}^{+\infty} S_{xx}(\omega) A(\omega) e^{-i\varphi(\omega)} e^{i\omega\tau} d\omega \\ &= \int_{-\infty}^{+\infty} S_{xx}(\omega) A(\omega) \cos[\omega\tau - \varphi(\omega)] d\omega \end{aligned} \quad (3.37)$$

It should be noted that the second equality in Equation (3.37) is valid because autospectral density function $S_{xx}(\omega)$ of a real quantity is real. In Equation (3.37), $\varphi(\omega)$ can be written in terms of wave speed and distance as

$$\varphi(\omega) = \omega\tau = \omega \frac{d}{c} \quad (3.38)$$

where τ is the time delay and c is the wave speed. In dispersive wave propagation two types of speeds are defined: (1) phase speed, and (2) group speed. The definition of each type and the differences between them will be discussed in details in Chapter 4. It is however worth mentioning that the general relationship between phase speed and group speed is defined as

$$c_g = (1 - n)c_p \quad (3.39)$$

where c_g is the group speed, c_p is the phase speed and n is defined as $c_p \propto k^{-n}$, where k is the wave number. In the current investigation $n = -1$, leading to

$$c_g = 2c_p \quad (3.40)$$

$$c_p \propto \omega^{1/2} \quad (3.41)$$

Equation (3.41) is explained in greater details in Chapter 4. The time delay for the phase and group speed are defined as

$$\tau_p = \frac{d}{c_p} = \frac{a}{\omega^{1/2}}, \tau_g = \frac{d}{c_g} = \frac{a}{2\omega^{1/2}} \quad (3.42)$$

where a is the constant of proportionality. Substitution for τ_p in Equation (3.37) gives

$$R_{xy}(\tau) = \int_{-\infty}^{+\infty} S_{xx}(\omega) A(\omega) \cos \left[\omega \left(\tau - \frac{a}{\omega^2} \right) \right] d\omega \quad (3.43)$$

Normalizing Equation (3.43), one obtains the following cross-correlation coefficient

$$\rho_{xy}(\tau) = \int_{-\infty}^{+\infty} S'_{xx}(\omega) \cos \left[\omega \left(\tau - \frac{a}{\omega^2} \right) \right] d\omega \quad (3.44)$$

where $S'_{xx}(\omega)$ is given by

$$S'_{xx}(\omega) = \frac{S_{xx}(\omega)A(\omega)}{\left(\int_{-\infty}^{+\infty} S_{xx}(\omega)d\omega \int_{-\infty}^{+\infty} A^2(\omega) S_{xx}(\omega)d\omega \right)^{\frac{1}{2}}} \quad (3.45)$$

In order to find the analytical solution of Equation (3.44), $S'_{xx}(\omega)$ should be restricted to a special type of random process. Based on the difficulties in correlation analysis for broad-band process, which are discussed in earlier paragraphs, $S'_{xx}(\omega)$ is assumed to be a narrow-band random process given by

$$S'_{xx}(\omega) = \begin{cases} \frac{1}{2B} & |\omega \pm \omega_0| \leq \frac{B}{2} \\ 0 & \text{otherwise} \end{cases} \quad (3.46)$$

Using Equation (3.44), the cross-correlation coefficient becomes

$$\rho_{xy}(\tau) = \frac{1}{B} \int_{\omega_0 - \frac{B}{2}}^{\omega_0 + \frac{B}{2}} \cos \left[\omega \left(\tau - \frac{a}{\omega^{\frac{1}{2}}} \right) \right] d\omega \quad (3.47)$$

This integral can be evaluated exactly but that is not convenient for engineering applications. Suggested by White (1969), one octave (the upper frequency limit is twice the lower limit) has become a widely acceptable bandwidth for the application of the cross-correlation technique. Cross-correlation of such filtered waves provides an estimate of the time delay that is fully consistent with the prediction of analytical formulas. Based on this suggestion, if the frequency band is an octave or less, several approximations can be applied to Equation (3.47). The most useful one comes by setting

$$\omega = \omega_0(1 + \varepsilon) \quad (3.48)$$

where for one octave band ε is equal to 1/3. The argument of the *cos* function in Equation (3.47) is replaced by

$$\begin{aligned} \omega \left(\tau - \frac{a}{\omega^{\frac{1}{2}}} \right) &= \omega_0(1 + \varepsilon) \left(\tau - \frac{a}{(\omega_0(1 + \varepsilon))^{\frac{1}{2}}} \right) \\ &= \omega_0(1 + \varepsilon)\tau - a(\omega_0)^{1/2}(1 + \varepsilon)^{1/2} \end{aligned} \quad (3.49)$$

Using Taylor series

$$(1 + \varepsilon)^{1/2} = 1 + \frac{\varepsilon}{2} - \frac{\varepsilon^2}{8} + \dots \quad (3.50)$$

Hence one obtains

$$\begin{aligned} & \omega_0(1 + \varepsilon)\tau - a(\omega_0)^{\frac{1}{2}}(1 + \varepsilon)^{\frac{1}{2}} \\ & \approx \omega_0(1 + \varepsilon)\tau - a\omega_0^{\frac{1}{2}}\left(1 + \frac{\varepsilon}{2}\right) \\ & \approx \omega_0\left(\tau - \frac{a}{\omega_0^{\frac{1}{2}}}\right) + \omega_0\left(\tau - \frac{a}{2\omega_0^{\frac{1}{2}}}\right)\varepsilon \end{aligned} \quad (3.51)$$

For one octave bandwidth this expression introduces one percent error, and for the bandwidth less than one octave, the error is even less. On referring to Equation (3.47), the cross-correlation coefficient becomes

$$\rho_{xy}(\tau) = \frac{\omega_0}{B} \int_{-\frac{B}{2\omega_0}}^{\frac{B}{2\omega_0}} \cos[\omega_0(\tau - \tau_p) + \omega_0(\tau - \tau_g)\varepsilon] d\varepsilon \quad (3.52)$$

Expanding the *cos* function, one obtains

$$\rho_{xy}(\tau) = \frac{\omega_0}{B} \cos \omega_0(\tau - \tau_p) \int_{-\frac{B}{2\omega_0}}^{\frac{B}{2\omega_0}} \cos \omega_0(\tau - \tau_g)\varepsilon d\varepsilon \quad (3.53)$$

The final analytical solution for the cross-correlation coefficient of narrow-band random process is

$$\rho_{xy}(\tau) = \cos \omega_0(\tau - \tau_p) \frac{\sin\left(\frac{B(\tau - \tau_g)}{2}\right)}{\left(\frac{B(\tau - \tau_g)}{2}\right)} \quad (3.54)$$

Figure (3.3) shows a typical cross-correlation coefficient of narrow-band random process in a single dispersive path. There are some interesting features that are worthy of note (Bendat and Piersol, 1986):

1. There are two terms in Equation (3.54): $\cos \omega_0(\tau - \tau_p)$ is the carrier function and

$\frac{\sin\left(\frac{B(\tau - \tau_g)}{2}\right)}{\left(\frac{B(\tau - \tau_g)}{2}\right)}$ is the modulation function or *envelope* of $\rho_{xy}(\tau)$.

2. The peaks of carrier function occur at $\tau_n = \tau_p \pm \left(\frac{2\pi n}{\omega_0}\right)$; where n is any integer.
3. The peak value of the envelope occurs at group wave time delay $\tau_g = \frac{d}{c_g}$ which, unlike non-dispersive wave propagation, does not generally coincide with the peak value of the cross-correlation coefficient.

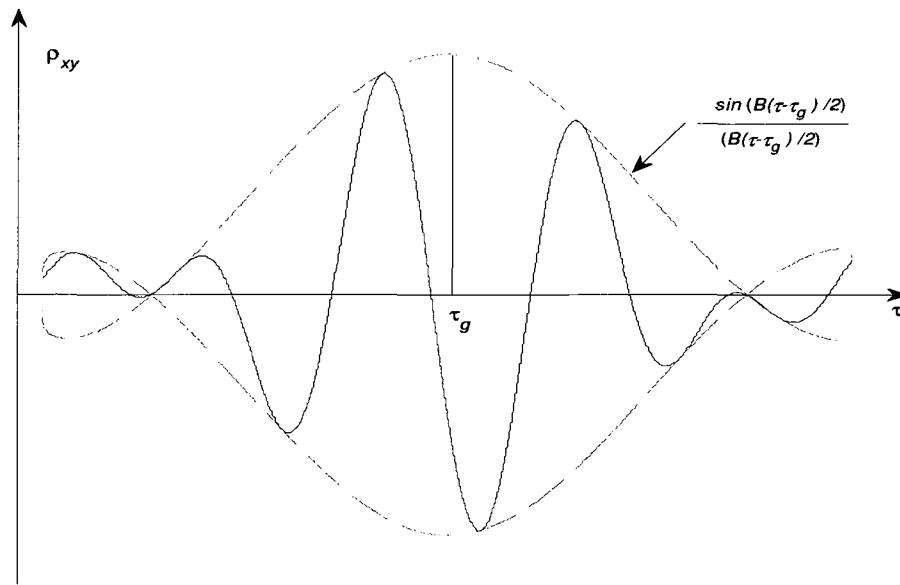


Figure (3.3): Cross-correlation coefficient of narrow-band white input and output of a dispersive path.

As shown in Figure (3.3), the peak of the envelope of the cross-correlation coefficient reveals the time delay of group wave. The envelope of the cross-correlation coefficient can be obtained by using the Hilbert transform. An introduction to Hilbert transform can be found in Bendat (1985). Applying this transformation, the envelope of Equation (3.54) can be derived as follows:

The criterion imposed on the Equation (3.54) was that the bandwidth of the wave is one octave or less. In the limit let us assume that the bandwidth is one octave. For one octave bandwidth with the upper limit ω_u , the lower limit ω_l , the central frequency ω_0 and the bandwidth B , one obtains:

$$\omega_u = \frac{4}{3} \omega_0, \omega_l = \frac{2}{3} \omega_0 \quad (3.55)$$

and

$$B = \frac{2}{3} \omega_0 \quad (3.56)$$

Since $B < \omega_0$, the Bedrosian theorem (Bedrosian, 1963) can be applied to the following equation

$$\rho_{xy}(\tau + \tau_g) = \cos \omega_0(\tau - (\tau_p + \tau_g)) \frac{\sin\left(\frac{B\tau}{2}\right)}{\left(\frac{B\tau}{2}\right)} \quad (3.57)$$

which gives

$$\tilde{\rho}_{xy}(\tau + \tau_g) = \sin \omega_0(\tau - (\tau_p + \tau_g)) \frac{\sin\left(\frac{B\tau}{2}\right)}{\left(\frac{B\tau}{2}\right)} \quad (3.58)$$

where $\tilde{\rho}_{xy}(\tau + \tau_g)$ is the Hilbert transform of $\rho_{xy}(\tau + \tau_g)$. Using the *shift property* of Hilbert transform in Equation (3.58), gives

$$\tilde{\rho}_{xy}(\tau) = \sin \omega_0(\tau - \tau_p) \frac{\sin\left(\frac{B(\tau - \tau_g)}{2}\right)}{\left(\frac{B(\tau - \tau_g)}{2}\right)} \quad (3.59)$$

Hence the analytical signal of the cross-correlation of Equation (3.54) is given by

$$z(t) = \rho_{xy}(\tau) + i\tilde{\rho}_{xy}(\tau) \quad (3.60)$$

or

$$z(t) = \frac{\sin\left(\frac{B(\tau - \tau_g)}{2}\right)}{\left(\frac{B(\tau - \tau_g)}{2}\right)} \left(\cos \omega_0(\tau - \tau_p) + i \sin \omega_0(\tau - \tau_p) \right) \quad (3.61)$$

It follows that the envelope of Equation (3.61) is

$$A_{xy} = \frac{\sin\left(\frac{B(\tau - \tau_g)}{2}\right)}{\left(\frac{B(\tau - \tau_g)}{2}\right)} \quad (3.62)$$

This is fully consistent with Figure (3.3).

II. Broad-band random process

As mentioned previously, broad-band correlation analysis does not provide any meaningful result. In order to resolve this difficulty, the broad-band wave should be filtered within certain band of frequency. This band of frequency is one octave or less. Here in this study, a frequency selective filter is designed to extract the desirable waveform from a broad-band wave. The general procedure, implemented in this study, is illustrated in Figure (3.4). As shown in Figure (3.4), the application of Fast Fourier Transform (FFT) to the broad-band wave provides its Fourier spectrum. The product of the Fourier transform of the wave by the designed filter results in the desirable form of wave in frequency domain. In this study the designed filter, $H(\omega)$ is defined as

$$H(\omega) = \begin{cases} 1 & |\omega \pm \omega_0| \leq \frac{B}{2} \\ 0 & \text{otherwise} \end{cases} \quad (3.63)$$

This filter sets all the undesirable frequency components equal to zero, and preserves only the desirable part. In the last step, the time domain representation of the wave is obtained by applying the Inverse Fast Fourier transform (iFFT). After filtering the waveforms within the specific band of frequency (which is an octave or less) the cross-correlation coefficient of Equation (3.54) can be evaluated as explained in the preceding sections.

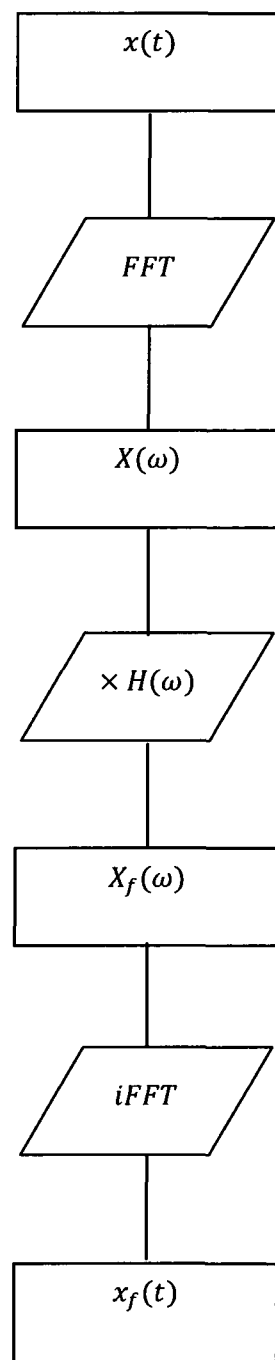
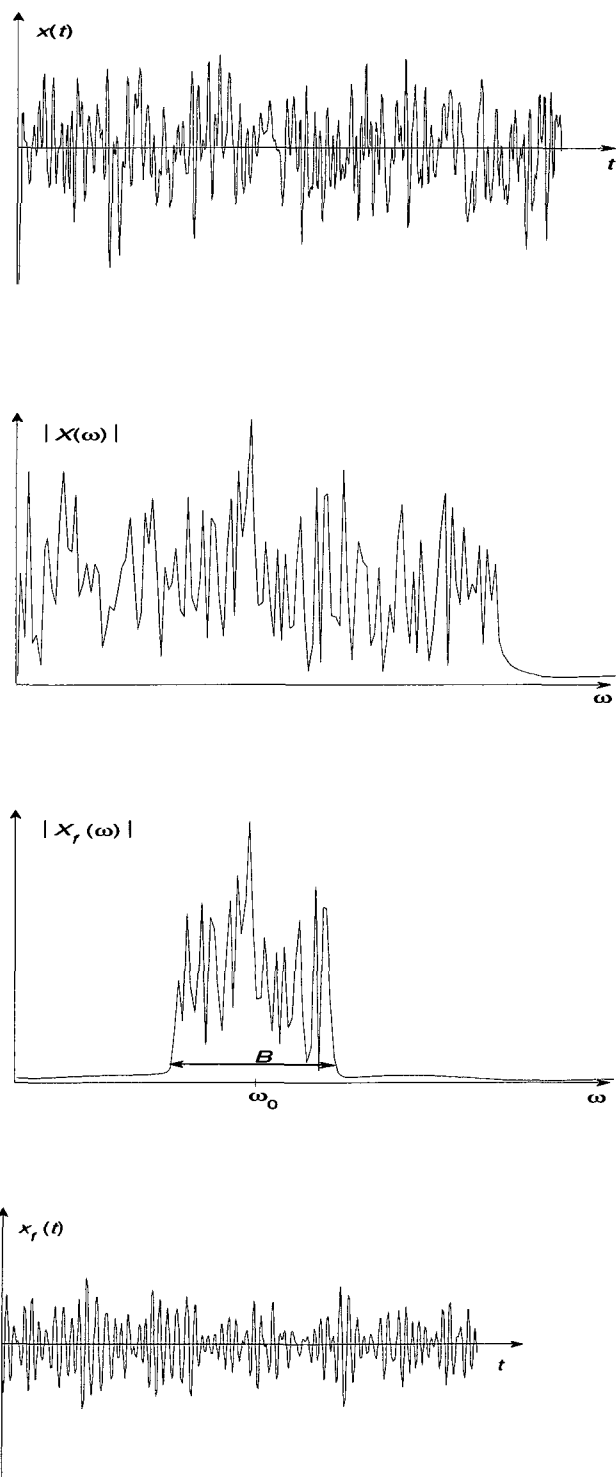


Figure (3.4) Frequency selective band-pass filter

Chapter 4

Wave Propagation

4.1 Introduction

In the frequency domain perspective, two types of waves exist: non-dispersive and dispersive. The speed of propagation of non-dispersive wave is frequency independent while dispersive wave propagation speed depends on frequency.

In the first part of this chapter, longitudinal wave propagation in a rod, which is an example of non-dispersive wave propagation, is considered. Spectral and finite element solutions of the vibration of a rod are derived. In the second part, flexural wave propagation in a beam, which is an example of dispersive wave propagation, is discussed. The notions of phase speed and group speed in the spectral representation of wave propagation in a beam are explained. At the end the finite element solution is investigated.

In the last part of this chapter, numerical implementations of spectral and Finite Element solutions are presented. The subsequent sections of this chapter closely follow Doyle (1997) and Humar (2002).

4.2 Non-dispersive Wave Propagation

The following assumptions are made in the elementary rod theory (Doyle, 1997):

- The rod is long and slender.
- The rod supports only axial stress.
- The Poisson's ratio effect is negligible.

The equation of motion of rod is given by

$$\frac{\partial}{\partial x} \left(EA \frac{\partial u}{\partial x} \right) - \bar{m} \frac{\partial^2 u}{\partial t^2} - \bar{c} \frac{\partial u}{\partial t} = P(t) \quad (4.1)$$

in which $u(x)$ is the axial displacement, E is the modulus of elasticity, A is the cross-sectional area of the rod, \bar{m} and \bar{c} are mass and viscous damping per unit length and $P(t)$ is the force per unit length. In the following sections, spectral and FEM derivations of this equation are discussed.

4.2.1 Spectral Derivation

Spectral representation of equation (4.1) yields

$$\frac{d}{dx} \left[EA \frac{d\hat{u}}{dx} \right] + (\omega^2 \bar{m} - i\omega \bar{c}) \hat{u} = \hat{P} \quad (4.2)$$

If the area and modulus of elasticity do not change along the length of the rod, the homogenous form of Equation (4.2) is given by

$$EA \frac{d^2 \hat{u}}{dx^2} + (\omega^2 \bar{m} - i\omega \bar{c}) \hat{u} = 0 \quad (4.3)$$

Since this equation has constant coefficients, the general solution has the following form (Doyle, 1997)

$$\hat{u}(x) = A e^{-ikx} + B e^{+ikx} \quad (4.4)$$

in which k is defined as

$$k = \sqrt{\frac{\omega^2 \bar{m} - i\omega \bar{c}}{EA}} \quad (4.5)$$

This relation is called the *spectrum relation* (Doyle, 1997). When damping is small, the spectrum relation can be approximated as (Doyle, 1997)

$$k = \sqrt{\left(\frac{\bar{m}}{EA}\right) \left[\left(\omega - i \frac{\bar{c}}{2\bar{m}}\right)^2 - \left(i\omega \frac{\bar{c}}{2\bar{m}}\right)^2 \right]} \cong \sqrt{\frac{\bar{m}}{EA}} \left(\omega - i \frac{\bar{c}}{2\bar{m}}\right) \quad (4.6)$$

Based on the general definition of dispersion relations, that is the relationship between group speed and frequency, and phase speed and frequency given by (Doyle, 1997)

$$c_p = \frac{\omega}{k}, c_g = \frac{d\omega}{dk} \quad (4.7)$$

one can derive expressions for the group speed and phase speed (for the small damping case) as

$$c_p = c_g = c \cong \sqrt{\frac{EA}{\bar{m}}} \quad (4.8)$$

Clearly the group speed and phase speed in the vibration of a rod are equal and independent of frequency. Consequently, the entire frequency band of the wave packet travels at the same speed and hence the wave packet is not distorted. As mentioned previously, this type of wave propagation is referred to as *non-dispersive wave propagation*.

Figure (4.1) shows the typical velocity response of a rod subjected to a triangular impulsive force at the middle of the rod, that is, at $x = 0 \text{ m}$.

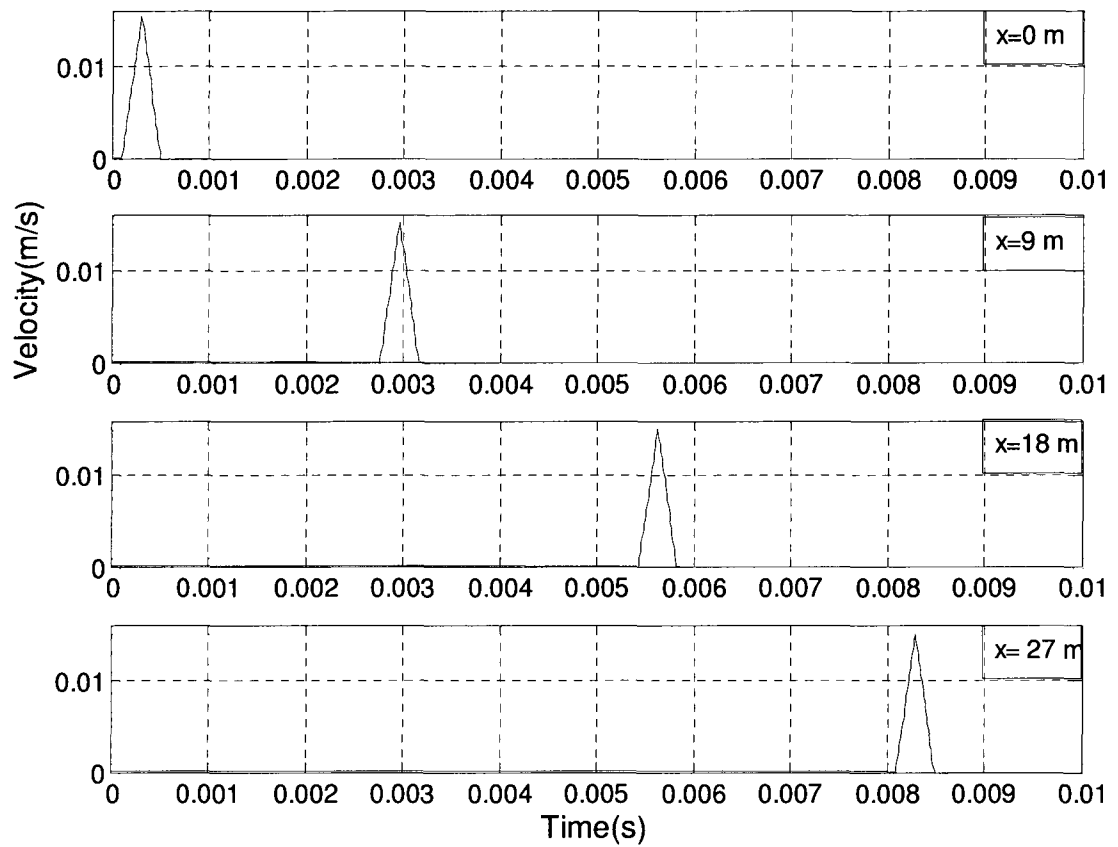


Figure (4.1): Typical velocity response of an impacted rod

As illustrated in Figure (4.1), the traveling wave packet is not distorted. Thus it can be concluded that the entire frequency band of the velocity wave is traveling with a constant speed.

4.2.2 FEM Derivation

In this section FEM formulation for wave propagation in a rod is considered. Equation (4.1) for a uniform rod yields to the following equation when the inertia, damping and forcing are neglected

$$\frac{\partial^2 u}{\partial x^2} = 0 \quad (4.9)$$

The solution of Equation (4.9) is simply

$$u(x) = a_0 + a_1 x \quad (4.10)$$

The constants a_0 and a_1 are obtained based on the displacements at the ends of the element. The displacement $u(x)$ at any location can therefore be written in terms of the nodal displacements u_1 and u_2 as

$$u(x) = \left(1 - \frac{x}{L}\right) u_1 + \left(\frac{x}{L}\right) u_2 \quad (4.11)$$

where L is the length of the element. Based on this expression the interpolation functions are:

$$\psi_1(x) = 1 - \frac{x}{L} \quad (4.12)$$

$$\psi_2(x) = \frac{x}{L} \quad (4.13)$$

The element stiffness matrix coefficients can be derived as (Humar, 2002)

$$\bar{k}_{ij} = EA \int_0^L \psi_i'(x) \psi_j'(x) dx \quad (4.14)$$

Substitution of interpolation functions into Equation (4.14) gives the element stiffness matrix, \bar{K} , as follows

$$\bar{K} = \frac{EA}{L} \begin{bmatrix} 1 & -1 \\ -1 & 1 \end{bmatrix} \quad (4.15)$$

There are several ways of constructing the element mass matrices. The method, which is discussed here, leads to a consistent mass matrix. The coefficients of consistent mass matrix can be derived by using the virtual work principle as follows (Humar, 2002):

$$\bar{m}_{ij} = \bar{m} \int_0^L \psi_i(x) \psi_j(x) dx \quad (4.16)$$

The element mass matrix is given by

$$\bar{M} = \frac{\bar{m}L}{6} \begin{bmatrix} 2 & 1 \\ 1 & 2 \end{bmatrix} \quad (4.17)$$

The equation of for deriving the viscous damping coefficients is similar to that used for the mass matrix coefficients, that is

$$\bar{c}_{ij} = \bar{c} \int_0^L \psi_i(x) \psi_j(x) dx \quad (4.18)$$

Thus one obtains

$$\bar{c} = \frac{\bar{c}L}{6} \begin{bmatrix} 2 & 1 \\ 1 & 2 \end{bmatrix} \quad (4.19)$$

Matrices \bar{K} , \bar{M} and \bar{C} are element stiffness, mass and damping matrices, respectively. In order to obtain the stiffness, mass and damping matrices of the system, \bar{K} , \bar{M} and \bar{C} of different elements should be assembled. This procedure leads to the assembled global stiffness matrix K , mass matrix M and damping matrix C . The governing equation of motion given by

$$M\ddot{u} + C\dot{u} + Ku = P \quad (4.20)$$

in which P is the vector of applied loads at the nodes.

4.3 Dispersive Wave Propagation

The following assumptions are made in the derivation of Bernoulli-Euler beam theory (Doyle, 1997):

- The beam is long and narrow.
- The deflection of the centerline of the beam is small and only in the transverse direction.
- Shear deformation is negligible.

The equation of motion of the beam is given by

$$\frac{\partial^2}{\partial x^2} \left(EI \frac{\partial^2 u}{\partial x^2} \right) + \bar{m} \frac{\partial^2 u}{\partial t^2} + \bar{c} \frac{\partial u}{\partial t} = P(t) \quad (4.21)$$

where $u(x)$ is the vertical displacement, E is the modulus of elasticity, I is the moment of inertia of the beam, \bar{m} and \bar{c} are respectively the mass and viscous damping per unit length and $P(t)$ is the force. In the following sections, spectral and FEM derivation of this equation are presented.

4.3.1 Spectral Derivation

Spectral representation of Equation (4.21) is given by

$$\frac{d^2}{dx^2} \left[EI \frac{d^2 \hat{u}}{dx^2} \right] + (\omega^2 \bar{m} - i\omega \bar{c}) \hat{u} = \hat{P} \quad (4.22)$$

Assuming that the beam has constant properties along its length, the simplified form of equation (4.22) becomes

$$EI \frac{d^4 \hat{u}}{dx^4} + (\omega^2 \bar{m} - i\omega \bar{c}) \hat{u} = 0 \quad (4.23)$$

Since this equation has constant coefficients, the solution is in the form of exponentials of kx or $-kx$, given by

$$\hat{u} = A e^{-ikx} + B e^{-kx} + C e^{ikx} + D e^{kx} \quad (4.24)$$

where k is

$$k = \sqrt[4]{\frac{\omega^2 \bar{m} - i\omega \bar{c}}{EI}} \quad (4.25)$$

Equation (4.25) is the spectrum relation for beams. Based on the general definitions of group speed and phase speed given in Equation (4.7), the dispersion relations, for the cases of no damping (and for small damping), are

$$c_p \cong \sqrt{\omega} \left[\frac{EI}{\bar{m}} \right]^{1/4} \quad (4.26)$$

$$c_g \cong 2\sqrt{\omega} \left[\frac{EI}{m} \right]^{1/4} \quad (4.27)$$

Note from equations (4.26) and (4.27), the phase and group speeds of waves in beam are dependent on the frequency. Hence different wave trains travel at different wave speeds. This phenomenon makes the shape of the wave packet to be distorted. Consequently, this type of wave propagation is referred to as *dispersive wave propagation*. The example of a dispersive wave is deep water ocean wave (Bendat and Piersol, 1993). Figure (4.2) shows a typical velocity response of a beam subjected to an impact force at its middle ($x = 0$). As the wave speed is frequency dependent, the propagating wave packet deforms as it travels, as shown by Figure (4.2). The speed of each frequency component is called the *phase speed*. However it is the superposition of these frequency components that make an observed wave. Thus the behavior of the superposition of some neighboring components is investigated. These neighboring components of the wave are collectively called *group waves* or *wave packets* (Brillouin, 1960). The speed associated with this group of waves is called *group speed*. The notion of group speed is discussed in more details (Doyle, 1997).

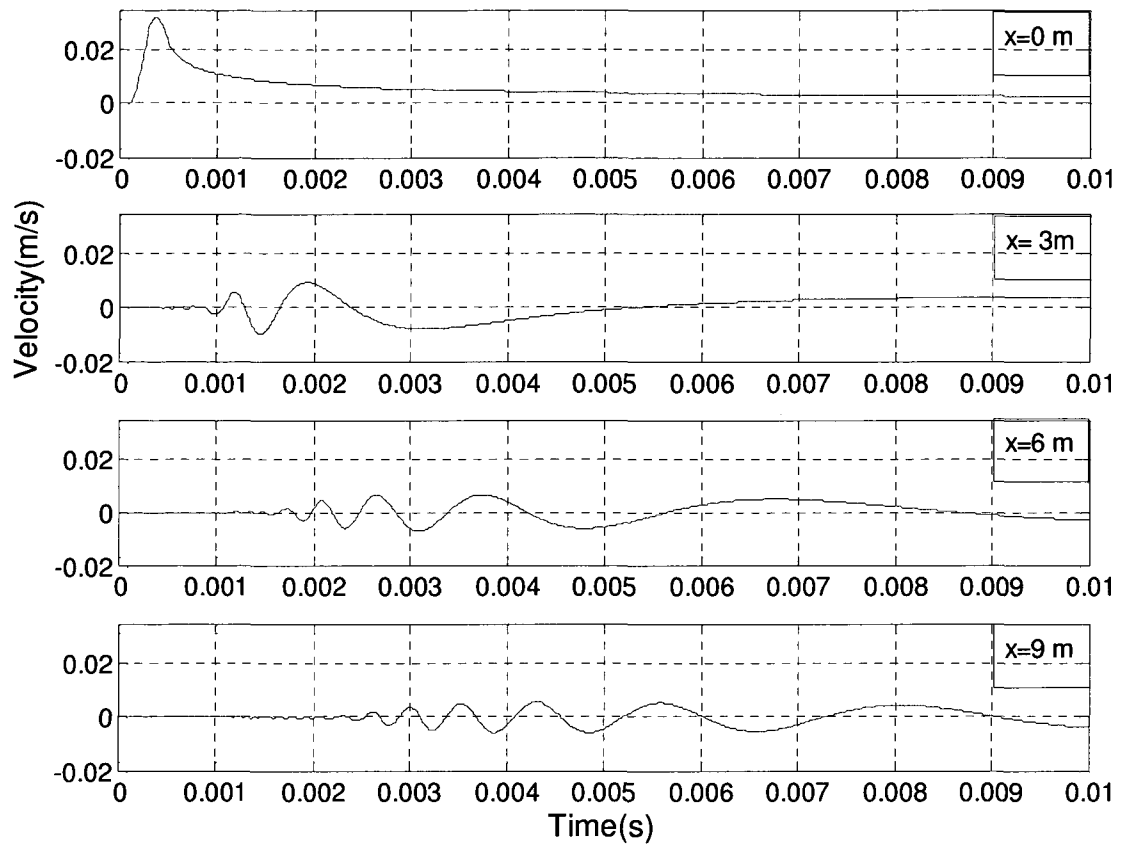


Figure (4.2): Typical velocity response of an impacted beam

Let us consider Equation (4.28), as the general solution of dispersive wave propagation (Doyle, 1997):

$$u(x, t) = \sum \hat{P}_n \hat{G}_n(k_n x) e^{i\omega_n t} \quad (4.28)$$

in which $u(x)$ is displacement, \hat{P}_n is the Fourier transform of the force and $\hat{G}_n(k_n x)$ is the frequency response function. For simplicity, we assume that the frequency response function has a simple exponential form with real wave number so that

$$u(x, t) = \sum \hat{P}_n e^{-ik_n x} e^{i\omega_n t} = \sum \hat{P}_n e^{-i(k_n x - \omega_n t)} \quad (4.29)$$

This solution given by Equation (4.29) has two terms:

1. The amplitude spectrum of the force: \hat{P}_n
2. The harmonic wave trains with different speeds given by $c_p = \frac{\omega_n}{k_n}$.

As mentioned earlier, the speed of each propagating harmonic wave, is called *phase speed*. In order to define the group wave, two neighboring harmonic components are considered as

$$u(x, t) = \hat{P}_n e^{-ik_n x} e^{i\omega_n t} + \hat{P}_{n+1} e^{-ik_{n+1} x} e^{i\omega_{n+1} t} \quad (4.30)$$

Assuming $\hat{P}_n \cong \hat{P}_{n+1}$, rewriting equation (4.30) in terms of *sin* and *cos*, and using the summation rules of *sin* and *cos*, yields

$$u(x, t) = \hat{P}_n [2 \cos(\Delta\omega t - \Delta k x) (\cos(\omega^* t - k^* x) + i \sin(\omega^* t - k^* x))] \quad (4.31)$$

In differential form, one obtains

$$u(x, t) = 2\hat{P}^* e^{-i(k^*x - \omega^*t)} \cos\left(\Delta k \left(x - \frac{d\omega}{dk} t\right)\right) \quad (4.32)$$

in which

$$\hat{P}^* = (\hat{P}_n + \hat{P}_{n+1})/2 \quad (4.33)$$

$$k^* = (k_n + k_{n+1})/2 \quad (4.34)$$

$$\omega^* = (\omega_n + \omega_{n+1})/2 \quad (4.35)$$

$$\Delta k = (k_{n+1} - k_n)/2 \quad (4.36)$$

$$\Delta\omega = (\omega_{n+1} - \omega_n)/2 \quad (4.37)$$

Equation (4.32) consists of three terms:

1. The first term, \hat{P}^* , is the average amplitude spectrum.
2. The second term, $e^{-i(k^*x - \omega^*t)}$, is called the *carrier wave*. The carrier wave is a sinusoid that is traveling with the average phase speed equal to $c_p^* = \frac{\omega^*}{k^*}$.
3. The third term, $\cos\left(\Delta k \left(x - \frac{d\omega}{dk} t\right)\right)$, is called the *group wave* or the *wave packet*.

This wave is the modulation of the carrier wave and includes the characteristics of the group of waves (in this example, the group of waves consists of two sinusoids). The phase speed of the modulated wave is called the *group speed* and is defined by

$$c_p = \frac{d\omega}{dk} \quad (4.38)$$

The notions of group speed and the phase speed can be easily understood in the movement of a caterpillar (Elmore and Heals, 1985). As the caterpillar moves forward, the ripples in its body move backward from head to tail. The movement of caterpillar's body shows an example of group wave behavior. The body is moving forward with the group speed while the ripples are moving in the opposite direction with a speed equal to the phase speed. Figure (4.3) illustrates the comparison between the carrier wave and group wave (Brillouin, 1960).

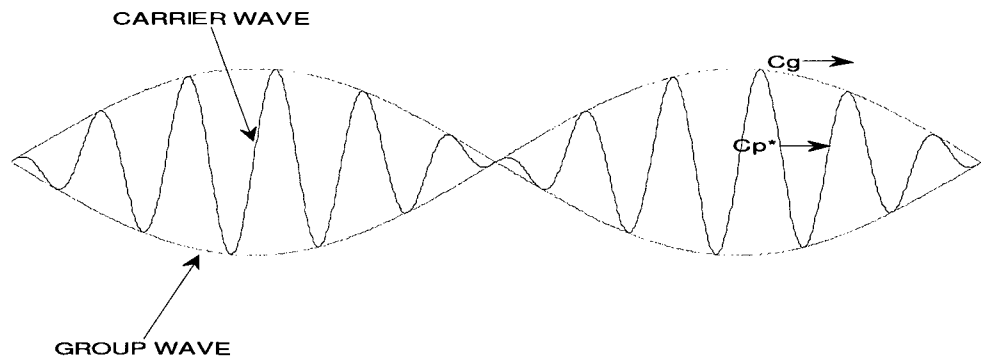


Figure (4.3): Carrier wave and group wave in dispersive wave propagation

4.3.2 FEM Derivation

The equation of motion of a uniform beam is given by

$$EI \frac{\partial^4 u}{\partial x^4} + \bar{m} \frac{\partial^2 u}{\partial t^2} + \bar{c} \frac{\partial u}{\partial t} = P(t) \quad (4.39)$$

Neglecting the inertia, damping and applied force, Equation (4.39) becomes

$$\frac{\partial^4 u}{\partial x^4} = 0 \quad (4.40)$$

The solution of Equation (4.40) is simply

$$u(x) = a_0 + a_1 x + a_2 x^2 + a_3 x^3 \quad (4.41)$$

The constants a_0 , a_1 , a_2 and a_3 are obtained based on the translation u and rotations ϕ of the ends of the element. The displacement can be written in terms of the nodal displacements as follows:

$$\begin{aligned} u(x) = & \left[1 - 3 \left(\frac{x}{L} \right)^2 + 2 \left(\frac{x}{L} \right)^3 \right] u_1 \\ & + \left(\frac{x}{L} \right) \left[1 - 2 \left(\frac{x}{L} \right) + \left(\frac{x}{L} \right)^2 \right] L \phi_1 \\ & + \left(\frac{x}{L} \right)^2 \left[3 - 2 \left(\frac{x}{L} \right) \right] u_2 \\ & + \left(\frac{x}{L} \right)^2 \left[-1 + \left(\frac{x}{L} \right) \right] L \phi_2 \end{aligned} \quad (4.42)$$

in which the interpolation functions are:

$$\psi_1(x) = 1 - 3 \left(\frac{x}{L} \right)^2 + 2 \left(\frac{x}{L} \right)^3 \quad (4.43)$$

$$\psi_2(x) = (x) \left[1 - 2 \left(\frac{x}{L} \right) + \left(\frac{x}{L} \right)^2 \right] \quad (4.44)$$

$$\psi_3(x) = \left(\frac{x}{L} \right)^2 \left[3 - 2 \left(\frac{x}{L} \right) \right] \quad (4.45)$$

$$\psi_4(x) = \left(\frac{x^2}{L} \right) \left[-1 + \left(\frac{x}{L} \right) \right] \quad (4.46)$$

Application of the principle of virtual work leads to the following expression for the coefficients of the stiffness matrix (Humar, 2002)

$$\bar{k}_{ij} = EI \int_0^L \psi_i''(x) \psi_j''(x) dx \quad (4.47)$$

Hence, one obtains

$$\bar{K} = \frac{EI}{L^3} \begin{bmatrix} 12 & 6L & -12 & 6L \\ 6L & 4L^2 & -6L & 2L^2 \\ -12 & -6L & 12 & -6L \\ 6L & 2L^2 & -6L & 4L^2 \end{bmatrix} \quad (4.48)$$

where \bar{K} is the element stiffness matrix.

Among different ways of defining the mass matrix, the consistent mass matrix method is chosen in this study. The coefficients of the consistent mass matrix are obtained from (Humar, 2002)

$$\bar{m}_{ij} = \bar{m} \int_0^L \psi_i(x) \psi_j(x) dx \quad (4.49)$$

Substitution of interpolation functions into equation (4.49) yields the element mass matrix, \bar{M} , as follows:

$$\bar{M} = \frac{\bar{m}L}{420} \begin{bmatrix} 156 & 22L & 54 & -13L \\ 22L & 4L^2 & 13L & -3L^2 \\ 54 & 13L & 156 & -22L \\ -13L & -3L^2 & 22L & 4L^2 \end{bmatrix} \quad (4.50)$$

As in the case of stiffness and mass coefficients, the viscous damping coefficients can be obtained from

$$\bar{c}_{ij} = \bar{c} \int_0^L \psi_i(x) \psi_j(x) dx \quad (4.51)$$

The element damping matrix is

$$\bar{C} = \frac{\bar{c}L}{420} \begin{bmatrix} 156 & 22L & 54 & -13L \\ 22L & 4L^2 & 13L & -3L^2 \\ 54 & 13L & 156 & -22L \\ -13L & -3L^2 & 22L & 4L^2 \end{bmatrix} \quad (4.52)$$

\bar{K} , \bar{M} and \bar{C} are element stiffness, mass and damping matrices respectively. In order to obtain the stiffness and mass matrices of the system, \bar{K} and \bar{M} of different elements should be assembled. The assemblage procedure leads to the assembled stiffness K ,

assembled mass M and assembled damping C matrices of the entire system and the following governing equation of motion

$$M\ddot{u} + C\dot{u} + Ku = P \quad (4.53)$$

in which P is the vector of applied loads at finite element nodes.

4.4 Numerical Implementation

4.4.1 Spectral Approach

The unknown coefficients of equations (4.4) and (4.24) should be evaluated based on the information about the force and boundary conditions of any problem. Finding the coefficient, the (FRF) of force and displacement i.e. $H_{f-d}(\omega)$ can be constructed. Next, in order to evaluate the analytical solution at different time steps and at discrete spatial locations, the numerical scheme of Figure (4.4) can be used (Doyle, 1997).

As shown in Figure (4.4), the force history is first transformed to the frequency domain using Fast Fourier Transform. In the next step, the product of force function and FRF ($H_{f-d}(\omega)$) is taken to obtain the response in the frequency domain. This step is performed in a loop over all frequency components. At the final step, the time history of displacements is obtained by taking the Inverse Fourier Transform of the frequency response.

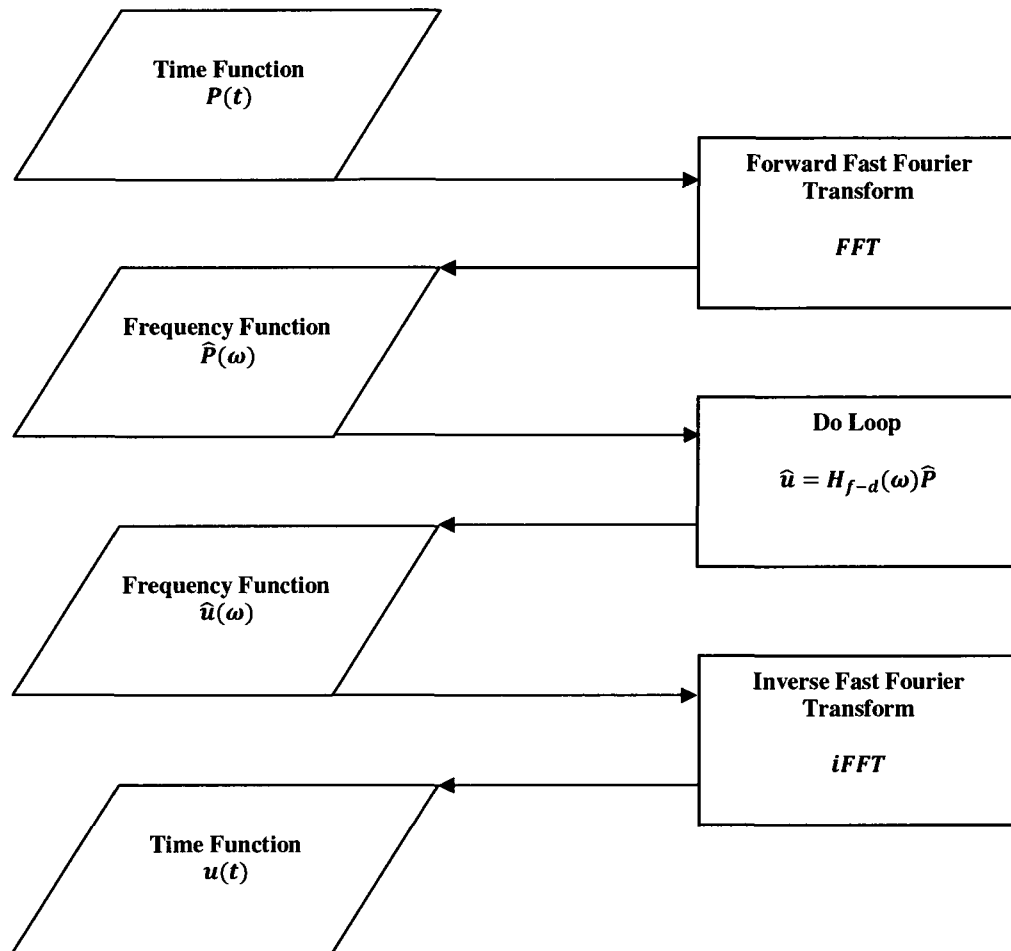


Figure (4.4): Numerical scheme of spectral solution

In relation to the procedure described here, it is necessary to mention two important points.

1. The product of FRF and the force history in frequency domain ($H_{f-d}(\omega)\hat{P}$) is performed only up to the Nyquist frequency, that is, over the first half of the

transformed force history. Since the time domain response should be real, the second half of the signal is considered as the complex conjugate of the initial part.

2. The zero frequency component (DC term) does not propagate. In order to have meaningful result for the DC term, Doyle (1997) has suggested the following value for the DC term:

$$\hat{u}_0 = - \sum_{n=1}^{N-1} \hat{u}_n \quad (4.54)$$

Choosing this value for the DC term, makes the first value of the time response equal to zero. This property is consistent with the fact that the system is quiescent before the arrival of the traveling wave.

4.4.2 FEM Approach

The numerical scheme implemented in FEM analysis is the Average Acceleration method. This method is unconditionally stable. The steps of this method are briefly illustrated in Figure (4.5). In Figure (4.5), \ddot{u}_i , \dot{u}_i and u_i are respectively the acceleration, velocity and displacement at time step i , and h is the time step. Following this scheme, at the first step acceleration is calculated from the known values of initial displacement and velocity by using the equations of motion. Next, given the force history, displacement at the next time step is evaluated, and then, the velocity and acceleration are calculated. This iteration is continued until the response at the final step is obtained.

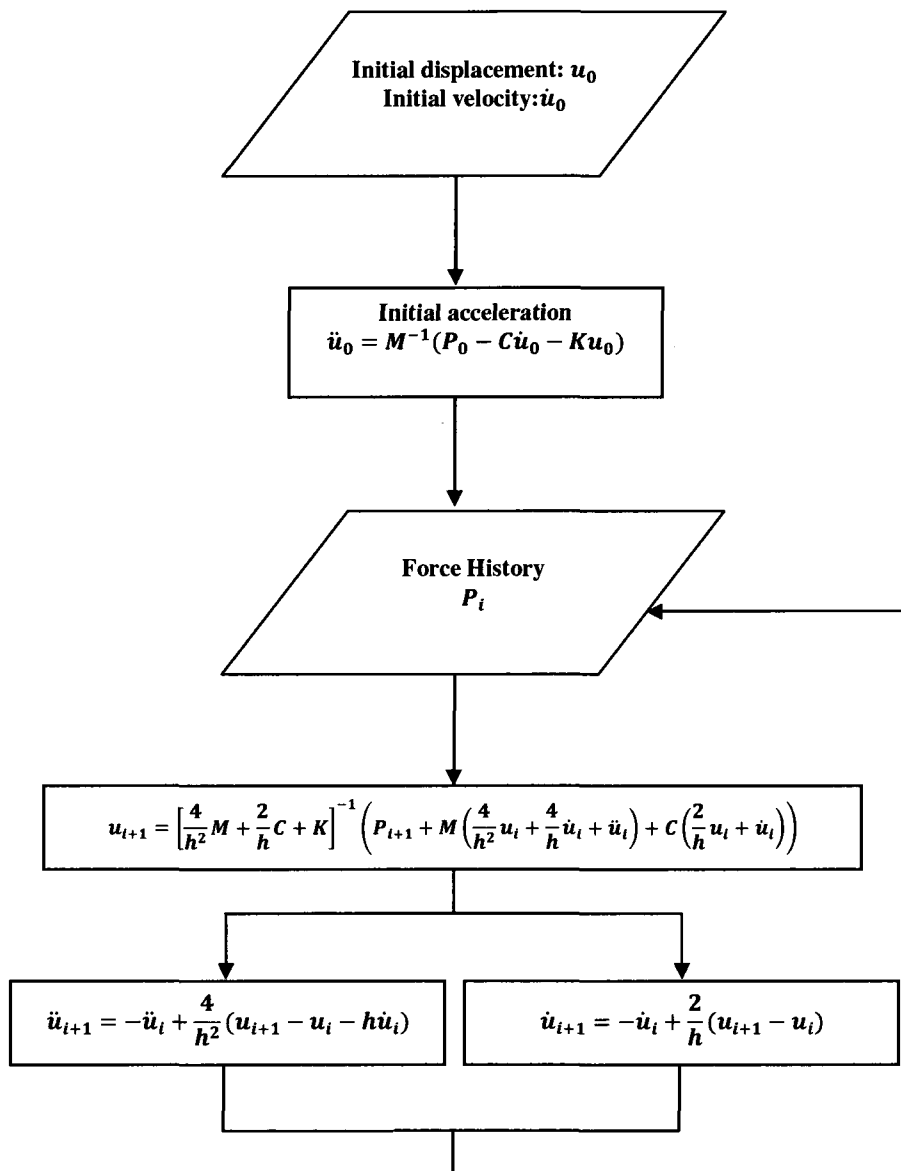


Figure (4.5): Numerical scheme of FEM solution

Chapter 5

Numerical Illustration:

Non-Dispersive Wave Propagation

5.1 Introduction

This chapter is devoted to numerical illustration of the non-dispersive wave propagation analysis discussed in previous chapters. In the first part of this chapter, an FEM model is chosen to simulate the response of a rod to impulsive loading. This model is validated by an analytical solution. In the second part, correlation analysis is implemented to estimate the time delay between two measurements on the rod. The effect of different types of loading, reflection from boundaries and noise are investigated in detail.

In the final part of the chapter, cross-correlation analysis is used as a tool to predict the presence of damage, its location, and its severity in non-dispersive wave propagation problems.

5.2 Model Validation

In the first section of this part, the analytical solution for an infinite rod is obtained. This solution is used as a benchmark to validate the FEM model presented in the second section.

5.2.1 Analytical Model

I. Problem Description

As shown in Figure (5.1), the infinite rod with the modulus of elasticity E and the uniform cross-sectional area A , is subjected to a force history P at the center of the rod $x = 0$.

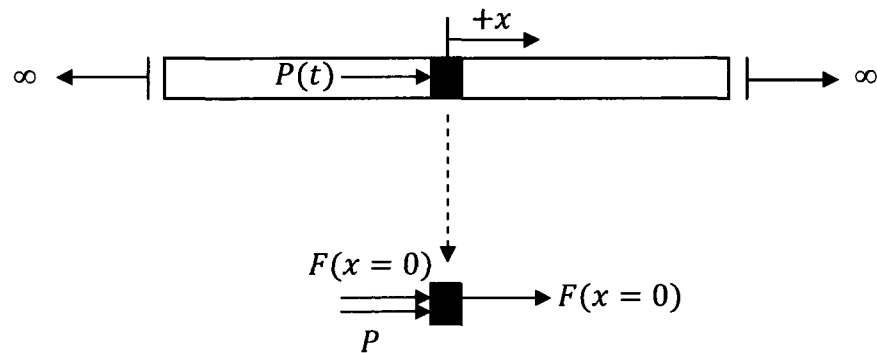


Figure (5.1): Analytical model: infinite rod impacted at the center

The material chosen for this study is concrete with the properties presented in Table (5.1). Viscous damping density of concrete given in this table corresponds to 7% damping ratio. This relationship will be explained in Section 5.2.2.

Material Property	Value
Elasticity Modulus (E)	27.4 GN/m^2
Mass Density	2400 kg/m^3
Viscous Damping Density	178000 N.s/m^4

Table (5.1): Material properties of the rod model

For $A = .04 \text{ m}^2$, Table (5.2) shows the properties per unit length.

Material Property	Value
Mass per Unit Length (\bar{m})	96 kg/m
Viscous Damping per Unit Length (\bar{c})	7000 N.s/m^2

Table (5.2): Material properties of rod model per unit length

As shown in Equation (4.8), for a small magnitude of damping the longitudinal wave speed can be approximated as:

$$c \cong \sqrt{\frac{EA}{\bar{m}}} = 3379 \text{ m/s} \quad (5.1)$$

The rod is excited by a triangular impulsive force at the middle. The force history is depicted in Figure (5.2). The Fourier spectrum of the force, which is shown in Figure (5.3), is obtained using a time step of 0.00001 s in a period of 0.01 s . This time step results in a Nyquist frequency of 50 kHz, which completely contains the frequency content of the force.

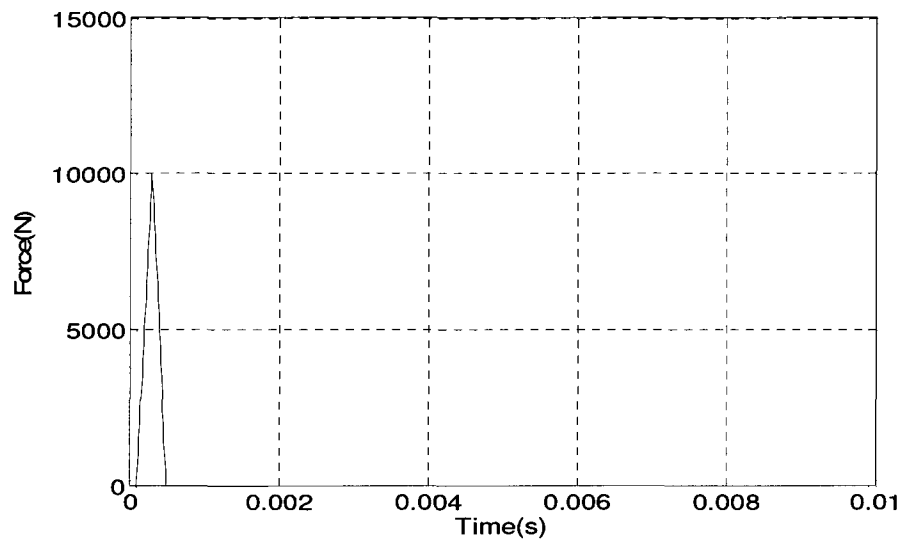


Figure (5.2): Triangular impulsive force applied at the center of infinite rod

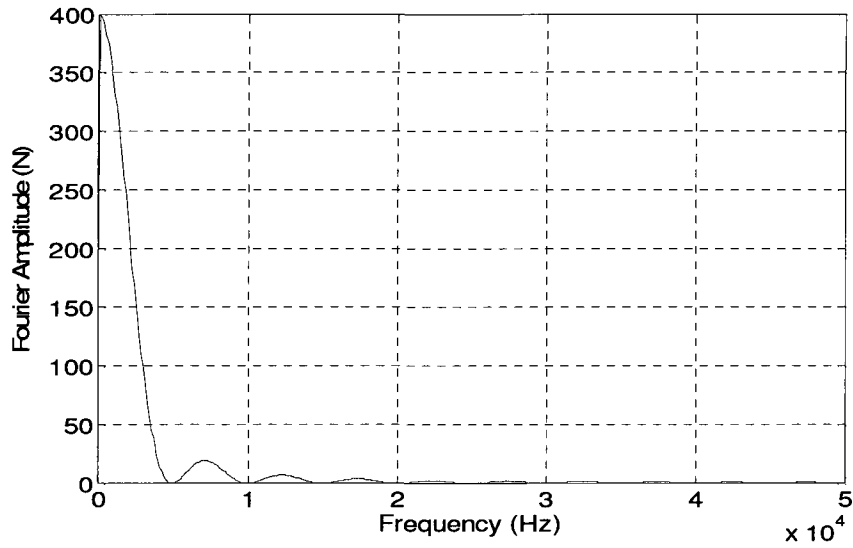


Figure (5.3): Fourier spectrum of impulsive force

II. Analytical Solution

As shown in Equation (4.4), the general spectral solution of the equation of motion for the rod is:

$$u(x, t) = \sum A e^{-i(kx - \omega t)} + \sum B e^{+i(kx + \omega t)} \quad (5.2)$$

Hence the general solution for $x > 0$ is given by

$$u(x, t) = \sum A e^{-i(kx - \omega t)} \quad (5.3)$$

Coefficient A , should be selected so as to satisfy the boundary condition. For satisfying the boundary condition, the equilibrium equation for an infinitesimal element at the impacting site is considered. The Free Body Diagram (FBD) of this element is depicted in Figure (5.1). Based on the symmetry of the rod, the two internal axial forces, which are acting on the element, are equal. Hence, one obtains (Doyle, 1997)

$$2F = 2EA \frac{\partial u(x, t)}{\partial x} = -P(t) \quad (5.4)$$

Expressing all the functions in their spectral representation, the boundary condition is given by

$$2EA \frac{d}{dx} \sum \hat{u}(x) e^{i\omega t} = - \sum \hat{P} e^{i\omega t} \quad (5.5)$$

Since this equation is valid for all times, one obtains

$$2EA \frac{d\hat{u}}{dx} = -\hat{P} \quad (5.6)$$

Substitution of spectral displacement from Equation (5.3) in Equation (5.6) results in the following equation at $x = 0$:

$$2EA(-ikA) = -\hat{P} \quad (5.7)$$

or

$$A = \frac{\hat{P}}{2EAik} \quad (5.8)$$

The complete solution is therefore given by (Doyle, 1997)

$$u(x, t) = \frac{1}{2EA} \sum \frac{\hat{P}}{ik} e^{-i(kx - \omega t)} \quad (5.9)$$

Based on Equation (5.9), the FRF that relates force to displacement can easily be derived

as

$$H_{f-d}(x, \omega) = \frac{1}{2EAik} e^{-ikx} \quad (5.10)$$

III. Analytical Results

The analytical solution of Equation (5.9) is numerically obtained using the scheme described in Section 4.4.1. Figure (5.4) shows the resulting velocity response of the rod at different locations.

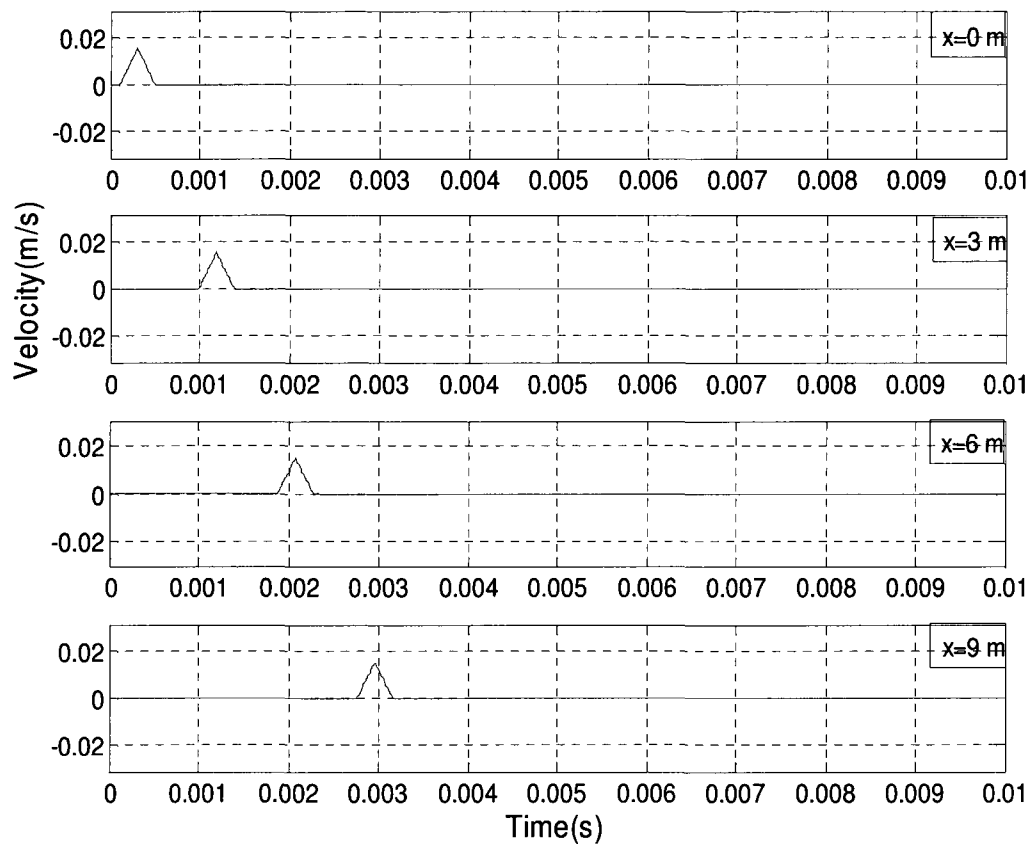


Figure (5.4): Velocity response of an infinite rod impacted at the center

Some interesting properties observed in Figure (5.4) are worth mentioning:

1. The wave packet is traveling with a constant travel speed $c = 3379 \text{ m/s}$. This speed can be calculated from the time delay between the arrivals of velocity waves at different locations of the rod.
2. Because all the frequency components are traveling at the same speed, there is no distortion in the shape of the wave packet.
3. Because the axial wave in a rod does not disperse while it propagates, rods are categorized as non-dispersive waveguides.

5.2.2 FEM Model

I. Problem Description

As shown in Figure (5.5), the finite rod with modulus of elasticity E , uniform cross-sectional area A and length L , is subjected to a force history P at the center of the rod $x = 0$. The boundary condition at each end is represented by a spring and a dashpot. Different cases with different values of the stiffness of spring and damping of dashpot are simulated.

The material properties, geometric properties and force history used in this example are exactly the same as in Section 5.2.1, except that instead of an infinite rod, a finite rod with total length of 20 m is chosen. Here some considerations about the damping properties should be mentioned.

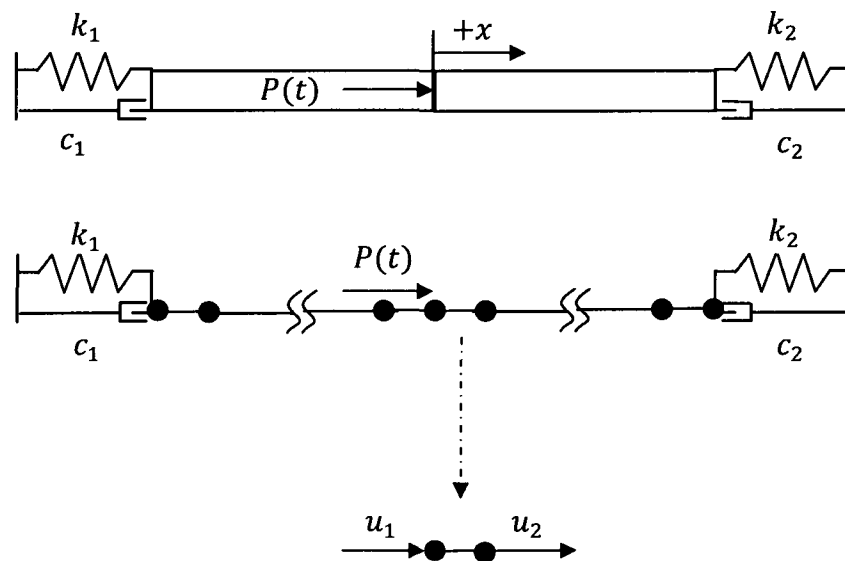


Figure (5.5): FEM model: rod impacted at the center

The constant of proportionality of damping and mass per unit length is denoted by α , namely

$$\alpha = \frac{\bar{c}}{\bar{m}} \quad (5.11)$$

From modal analysis, one obtains

$$\alpha = 2\zeta\omega_n \quad (5.12)$$

in which ζ is the damping ratio and ω_n is the n th modal frequency. From equations (5.11) and (5.12), a relationship for the damping ratio can be derived as

$$\zeta = \frac{\bar{c}}{2\omega_n\bar{m}} \quad (5.13)$$

For a fixed-fixed rod the natural frequency is defined as

$$\omega_n = \frac{n\pi}{L} \sqrt{\frac{EA}{\bar{m}}} \quad (5.14)$$

If the damping ratio is evaluated for the first natural frequency, one obtains

$$\zeta = \frac{\bar{c}L}{2\pi\sqrt{\bar{m}EA}} \quad (5.15)$$

Using Tables (5.1) and (5.2) gives

$$\zeta \cong 7\% \quad (5.16)$$

Thus the damping ratio is 7%.

II. FEM Mesh

The properties of the finite element mesh are presented in Table (5.3)

Properties	Value
Length of the rod	20 m
Length of elements	5 cm
Number of elements	400
Number of degrees of freedom	401

Table (5.3): FEM mesh properties

Let us assume that the wavelength of the response is captured by n finite elements, namely, $\lambda = ne_l$, where e_l is the element length. , The relationship between wavelength and wavenumber yields

$$k = \frac{2\pi}{\lambda} = \frac{2\pi}{ne_l} \quad (5.17)$$

Using the spectrum relation defined in Equation (4.6), one obtains

$$\omega \sqrt{\frac{\bar{m}}{EA}} = \frac{2\pi}{ne_l} \quad (5.18)$$

or

$$n = \frac{1}{e_l f} \sqrt{\frac{EA}{\bar{m}}} \quad (5.19)$$

Assuming that the maximum frequency needs to be captured is 17 *kHz*, substitution of the values given in Tables (5.2) and (5.3) in Equation (5.19) gives

$$n \cong 4 \quad (5.20)$$

The calculated value for n shows that the wavelength corresponding to the maximum frequency needs to be captured is represented by four finite elements. This is a reasonable representation and shows that the FEM mesh is fine enough to capture the wave phenomena quite accurately.

III. FEM Results

In this example numerical results for the problem described in the previous sections are presented for three different boundary conditions:

1. Rod with absorbing boundary conditions.
2. Rod with free boundary condition.
3. Rod with fixed boundary condition.

1. Rod with absorbing boundary condition

In this case, the values of c_1 and c_2 are adjusted such that the dashpots prevent any reflection from the boundaries. This value, which is obtained by simulated experiments, is $3.25 \times 10^5 \frac{N.s}{m}$.

Figure (5.6) shows the velocity response of the rod at different locations. This figure exactly matches with the response of impacted infinite rod in Figure (5.4). This analogy validates the FEM model and numerical scheme used in this simulation. It also shows the capability of FEM mesh to fully capture the wave phenomena.

2. Rod with free boundary condition

In order to investigate the effect of free boundary conditions on the propagation of wave packet, free boundary conditions are simulated here by setting stiffness and damping of springs and dashpots equal to zero. Response of rod under this condition is illustrated in Figure (5.7). Some interesting features of Figure (5.7) are worth mentioning:

1. In all subfigures of Figure (5.7), except the first one, the first wave packet is related to the incident wave, the second one corresponds to the reflected wave from right support and the third one shows the reflected wave from the left support. But in the subfigure for location $x = 0$, due to the symmetry of rod at that location, the reflected waves from left and right supports arrive at the same time and are superposed.
2. The reflected wave packet has the same shape as the incident one. This is the effect of free boundary conditions.

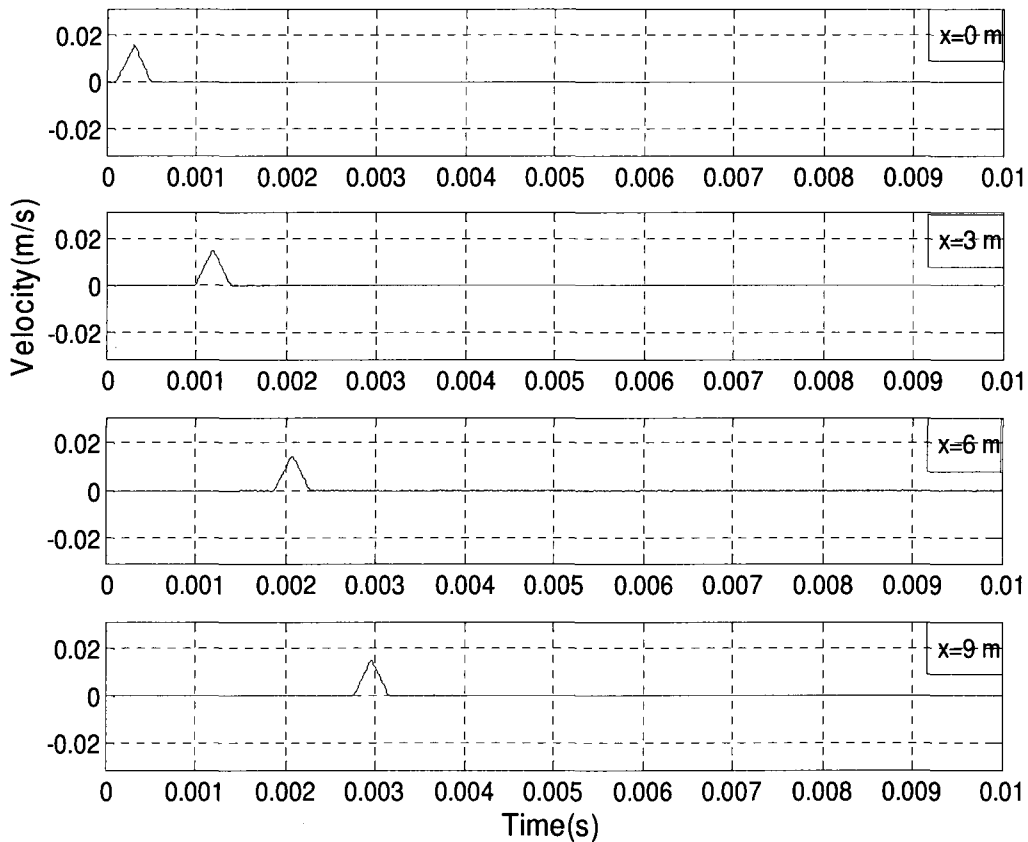


Figure (5.6): Velocity response of impacted rod with absorbing boundary condition

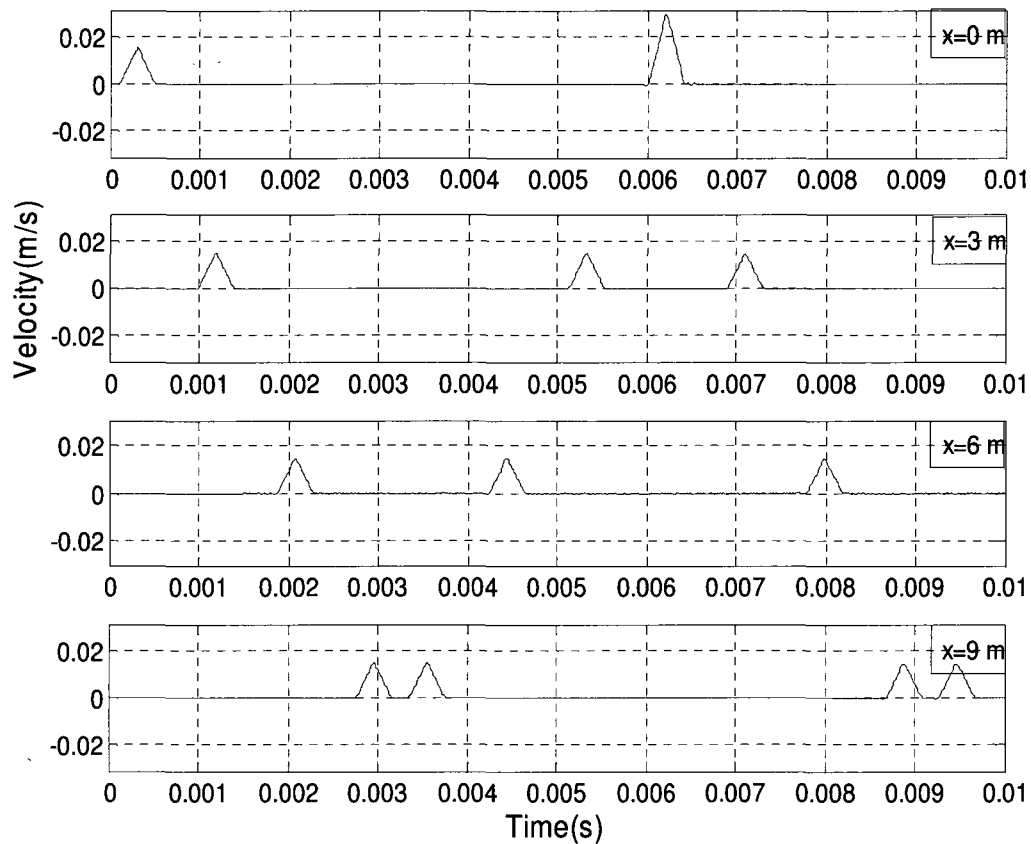


Figure (5.7): Velocity response of impacted rod with free boundary condition

3. Rod with fixed boundary condition

Fixed supports at the boundaries are simulated by inserting large values for k_1 and k_2 .

Figure (5.8) shows the velocity response for the rod with fixed supports to a triangular impact at the center. Interesting features are

1. Similar to Figure (5.7), first wave packet shows the incident wave, second one is related to reflected wave from the right support and the third wave packet represents the reflected wave from the left support. At location $x = 0$, the incident and reflected waves are superposed.

2. Reflected waves from fixed support have a shape that is similar to an inverted incident wave.

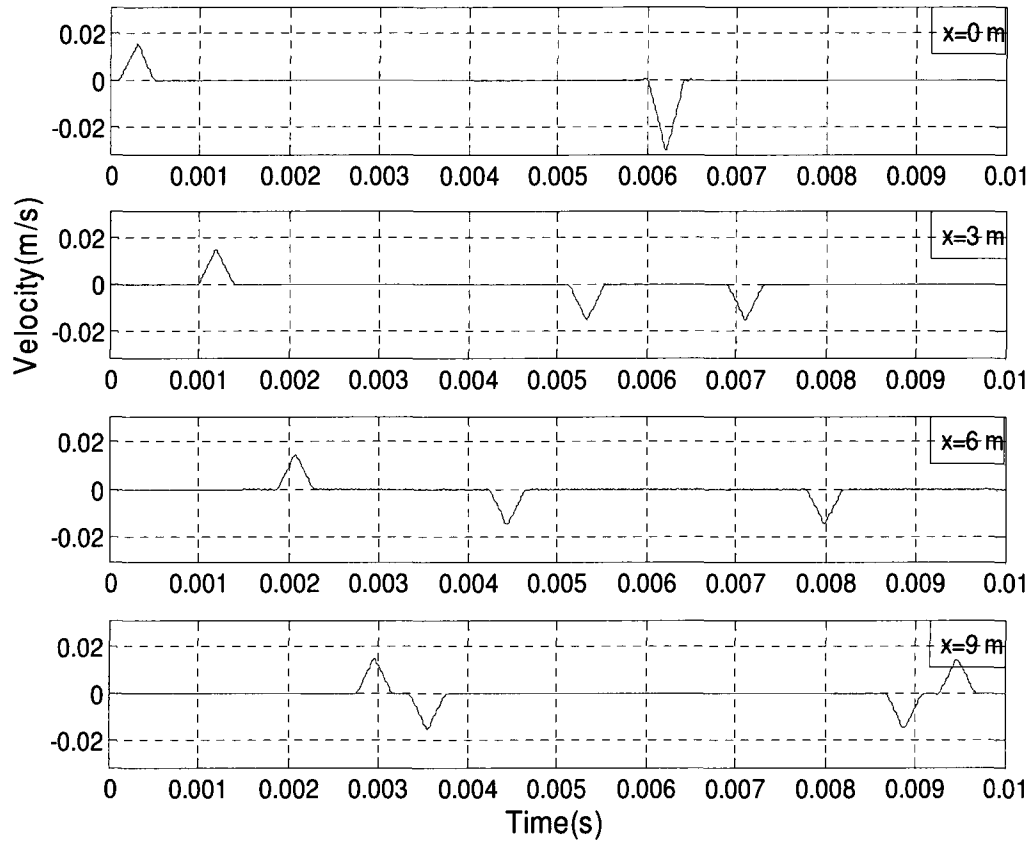


Figure (5.8): Velocity response of impacted rod with fixed boundary condition

5.3 Time Delay Estimation

In this part of Chapter 5, the time delay estimation for a rod, which is an example of a non-dispersive waveguide, is investigated. The effects of different types of loading, reflection from boundaries and presence of noise on the estimated time delay are explored.

5.3.1 Problem Description

The non-dispersive model is a rod shown in Figure (5.9). The material and geometric properties are exactly the same as given in Section 5.2.1. The rod is excited at the center and two sensors measure its velocity and acceleration responses. In the following parts of this thesis whenever reference is made to measurements, they are in fact simulated measurements. The locations of the load and the sensors are shown in Figure (5.9). The speed of the longitudinal wave for this problem is given by

$$c \cong \sqrt{\frac{EA}{\bar{m}}} = 3379 \text{ m/s} \quad (5.21)$$

Since the length of the path, that is the distance between sensors A and B, is 4 m, the time delay will be:

$$\tau = \frac{d}{c} = 0.0118 \text{ s} \quad (5.22)$$

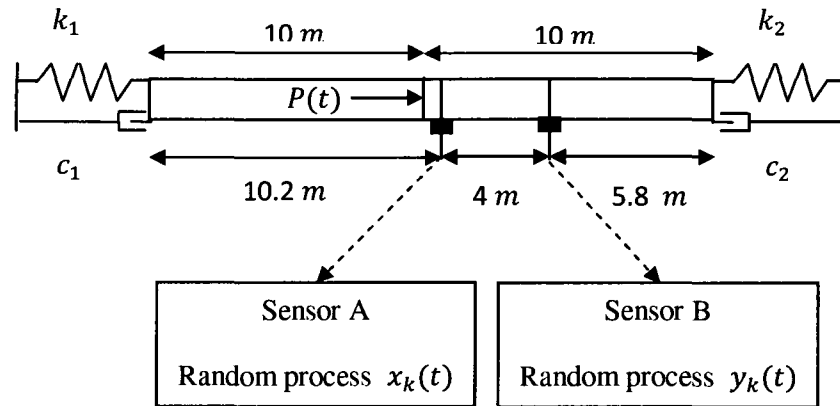


Figure (5.9): Rod model for time delay estimation problem

5.3.2 Effect of Loading

In this section the influence of the type of loading on the efficiency of the cross-correlation analysis in estimating the time delay between measurements at A and B is evaluated. As in Section 5.2.2, c_1 and c_2 are chosen such that the supports provide absorbing boundary conditions. Because of this, reflection of waves has no effect in the responses.

The effects of three types of loading are explored:

- I. Narrow-band force
- II. Broad-band force
- III. Transient force

I. Narrow-band force

The narrow-band force used in this analysis is a narrow-band white random process with central frequency $\omega_0 = 2\pi \times 6000 \text{ rad/s}$ and a bandwidth $B = 2\pi \times 4000 \text{ rad/s}$.

Figure (5.10) illustrates a sample of the force history and Figure (5.11) shows the autospectral density function of the force.

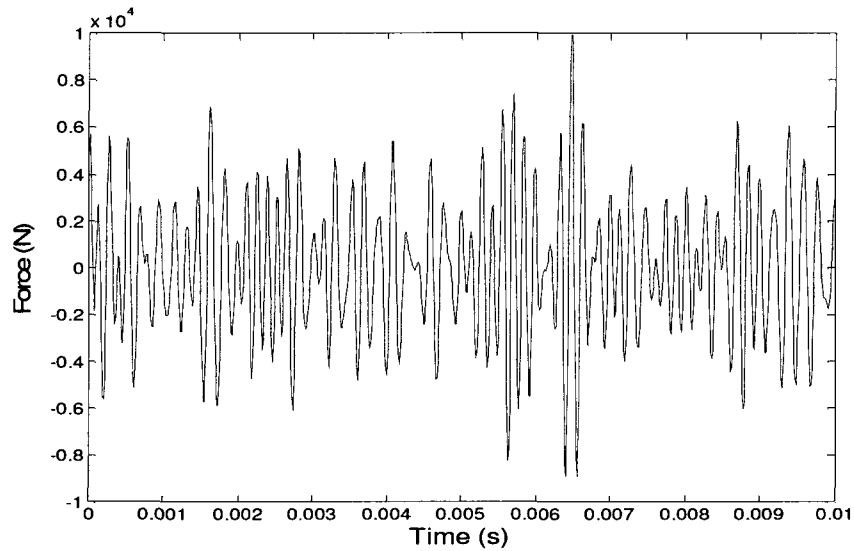


Figure (5.10): A sample of the narrow-band force history

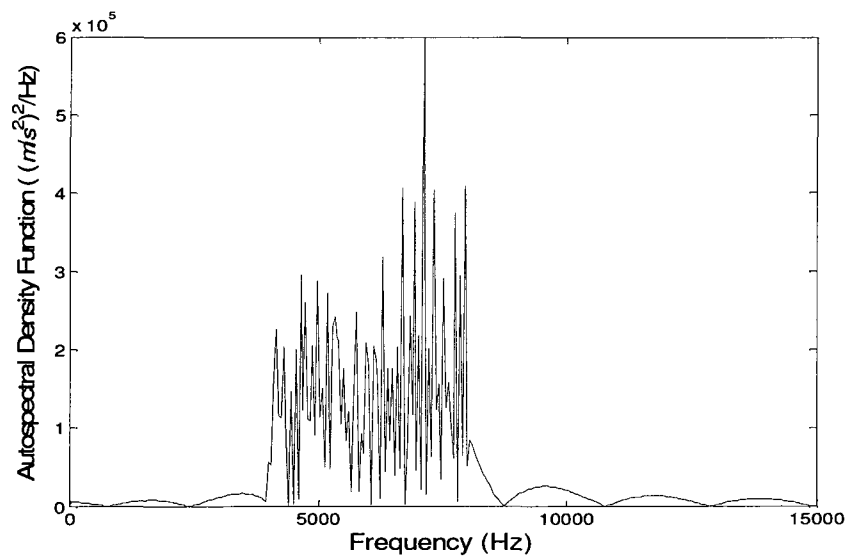


Figure (5.11): Autospectral density function of narrow-band force

One sample of each of the simulated measurements at sensors A and B obtained by using FEM model is depicted in Figure (5.12). Additional samples of simulated measurements are obtained by using different samples of narrow-band force histories. These measurements are noise free; and that is the reason the time delay can be readily detected from the figures. But in real problems, the responses are always corrupted by noise. The noisy cases will be explained in Section 5.3.4.

Figure (5.13) shows autospectral density functions of the measurements at sensors A and B. It can be noted from this figure that the frequency range of the response is similar to that of the force. This is because all traveling waves are damped out at the boundaries. Even if there were some reflection from the boundaries, the short time window, in which the response is obtained, does not allow standing waves to be produced.

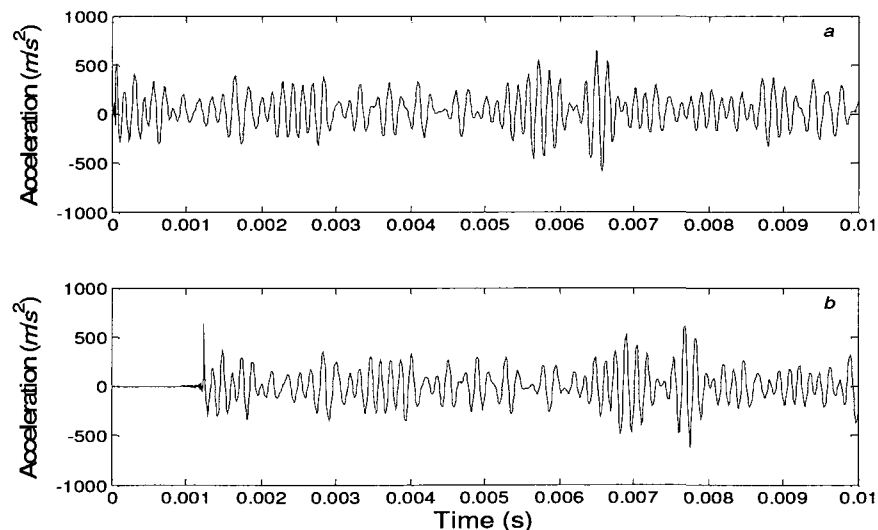


Figure (5.12): Acceleration response a) at sensor A b) at sensor

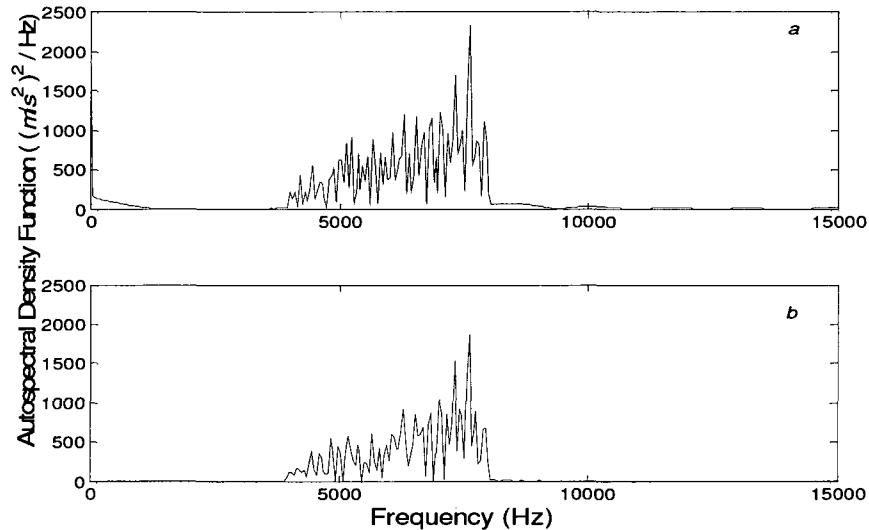


Figure (5.13): Autospectral density function of acceleration responses

a) at sensor A b) at sensor B

Cross-correlation coefficient of the measurements is given in Figure (5.14). Some important points may be noted by reference to this figure:

1. The peak of the experimental cross-correlation coefficient coincides with analytically calculated cross-correlation coefficient given by Equation (3.12).
2. As the rod is a non-dispersive waveguide, the peak of the experimental cross-correlation coefficient exactly coincides with the peak of its envelope.
3. In Figure (5.14), the ensemble average is performed using 10 samples. Increasing the number of samples does not improve the solution very much (in comparison to the exact solution) meaning the statistical sampling error is not significant here. This is mainly due to the existence of spurious frequency components in the high frequency range. Use of velocity response shows better match with the exact

solution as evident in Figure (5.15). This is due to the fact that the influences of spurious high frequency components are less severe for velocity than acceleration response.

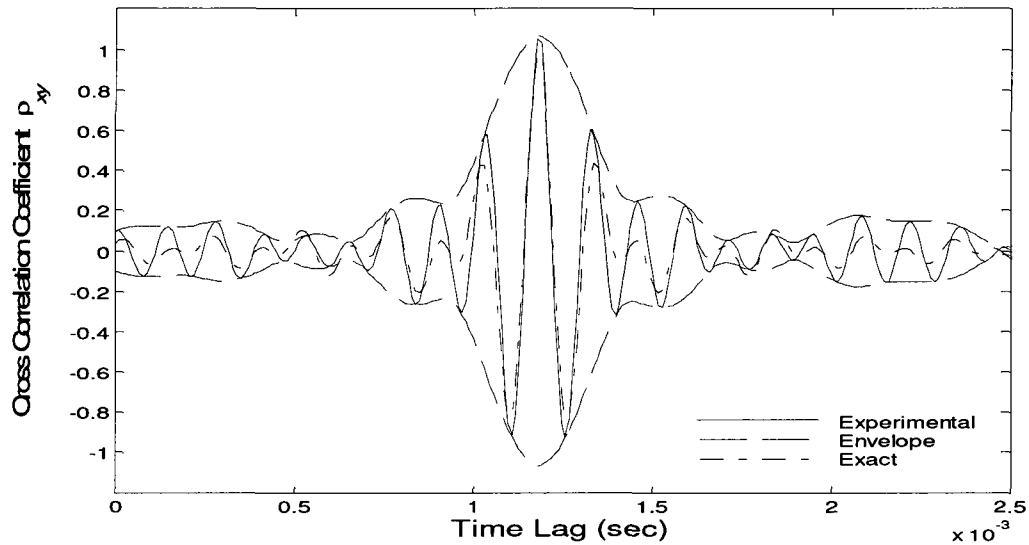


Figure (5.14): Cross-correlation coefficient of acceleration response to narrow-band force

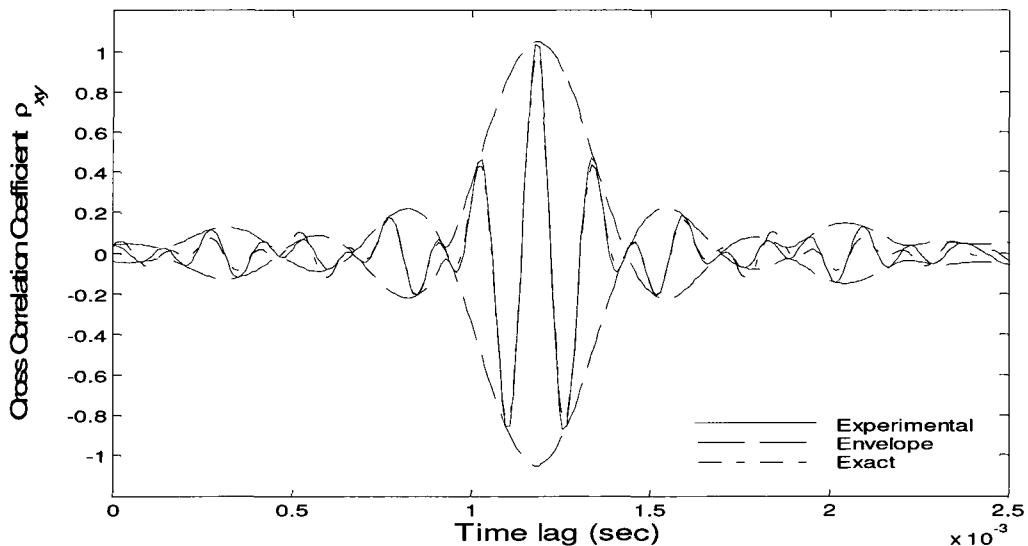


Figure (5.15): Cross-correlation coefficient of velocity response to narrow-band force

II. Broad-band force

In this section, cross-correlation analysis of broad-band force is investigated. The broad-band force, implemented in this analysis, is a broad-band white random process with central frequency $\omega_0 = 2\pi \times 6000 \text{ rad/s}$ and a bandwidth of $B = 2\pi \times 12000 \text{ rad/s}$. Figure (5.16) shows the cross-correlation coefficient between the acceleration measurements at sensors A and B, while Figure (5.17) presents the same quantity for the velocity measurements. As shown by these figures, in both cases the time delay is accurately detected. The cross-correlation of velocity measurements shows better agreement with the exact solution than acceleration response. This is due to the sensitivity of acceleration measurements to spurious high frequency response.

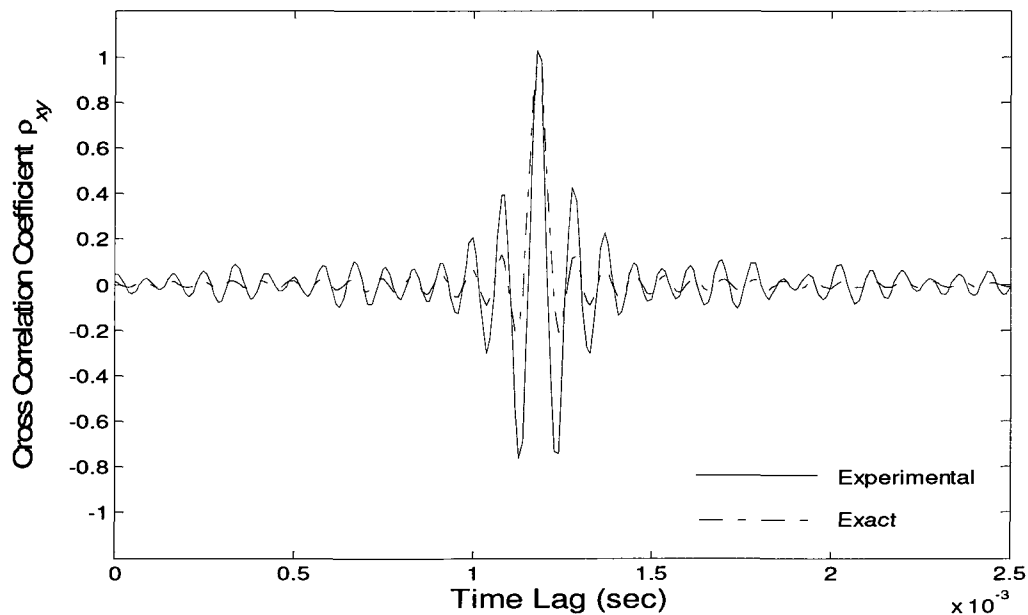


Figure (5.16): Cross-correlation coefficient of acceleration response to broad-band force

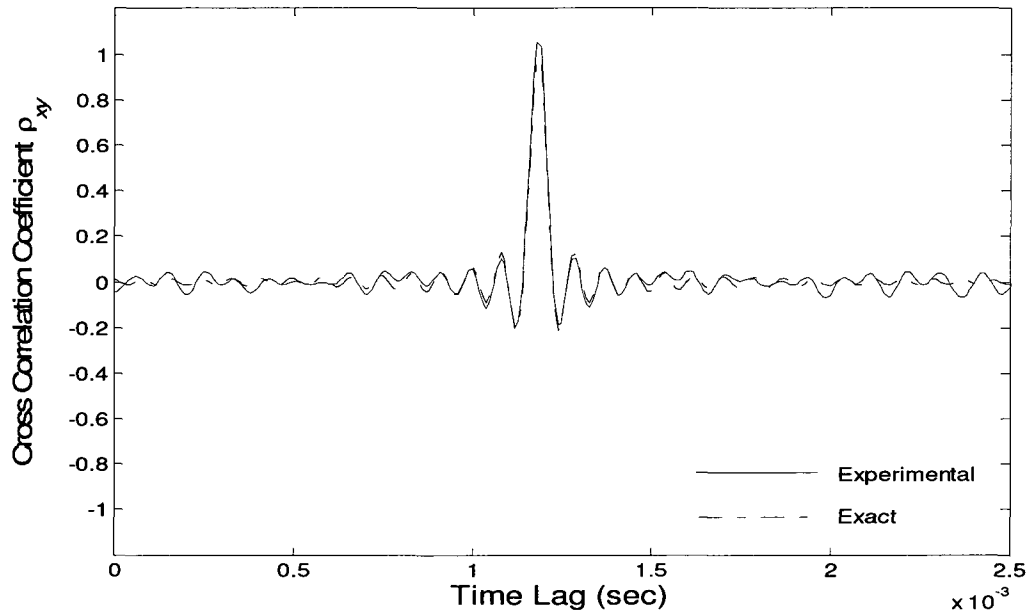


Figure (5.17): Cross-correlation coefficient of velocity response to broad-band force

III. Transient force

The transient force used in this section is a triangular impulsive force shown by Figure (5.18). Figure (5.19) illustrates the Fourier spectrum of the triangular force. As can be noticed from this figure, the main lobe of the Fourier spectrum appears in the bandwidth $B = 2\pi \times 5000 \text{ rad/s}$. Acceleration responses at sensors A and B are shown in Figure (5.20). This figure shows that the acceleration wave packet travels with axial wave speed $c = 3379 \text{ m/s}$.

According to discussion in Section 2.3.3, all concepts of correlation analysis are applicable even when the input and output of the system are transient. Figure (5.21) and Figure (5.22) show the results of correlation analysis. In both figures the time delay is accurately estimated with less than 1% error.

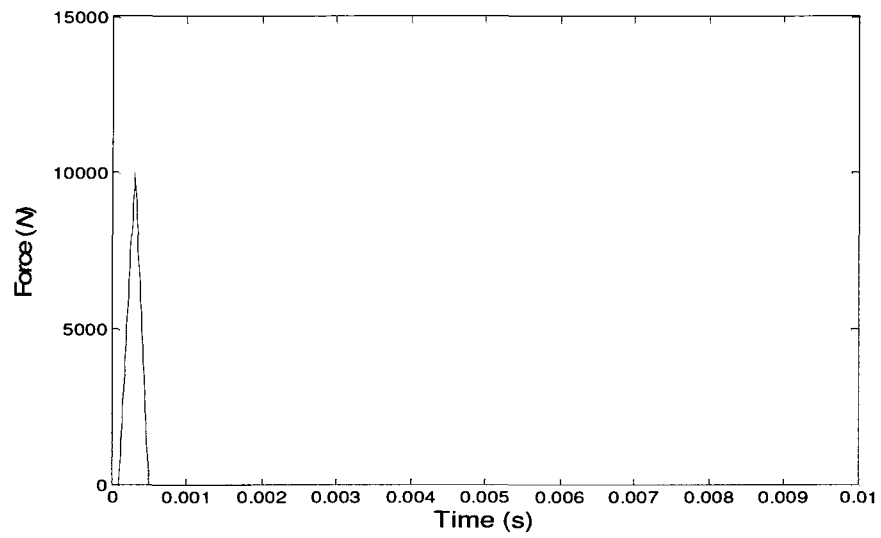


Figure (5.18): Triangular impulsive force

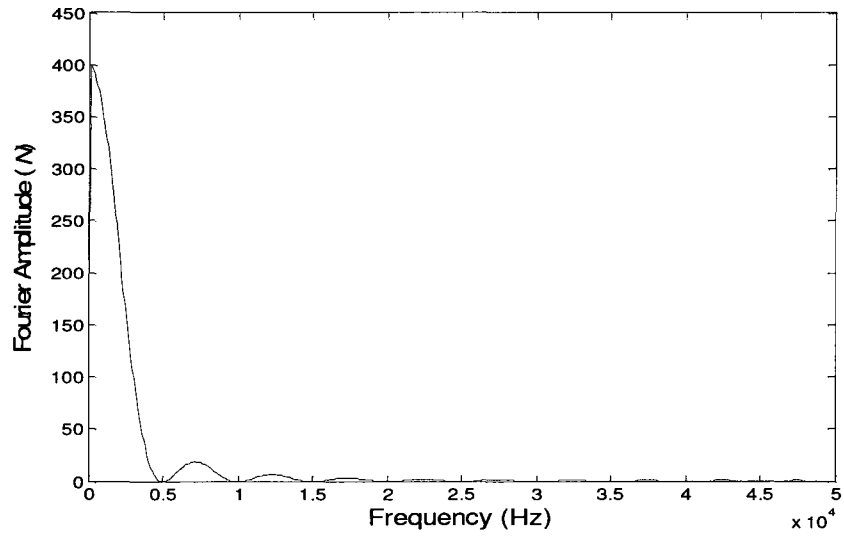


Figure (5.19): Fourier spectrum of the triangular impulsive force

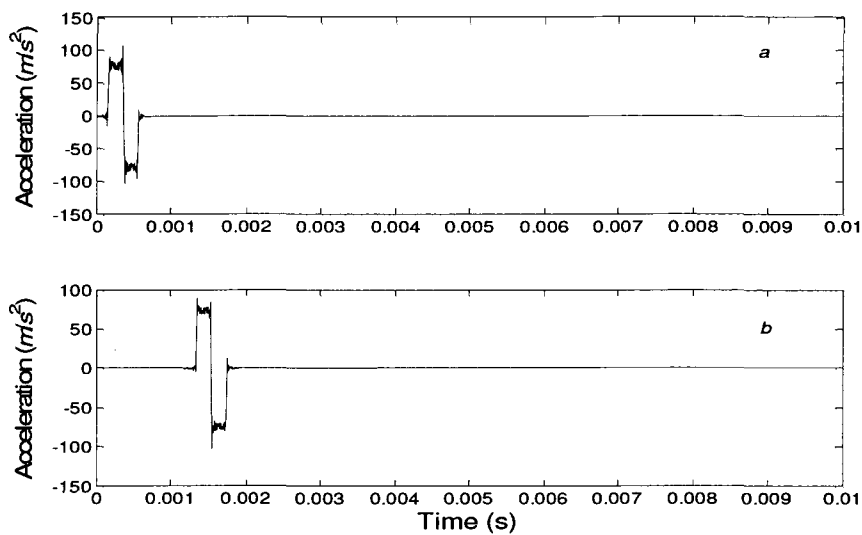


Figure (5.20): Acceleration response due to triangular impulsive force

a) at sensor A b) at sensor B

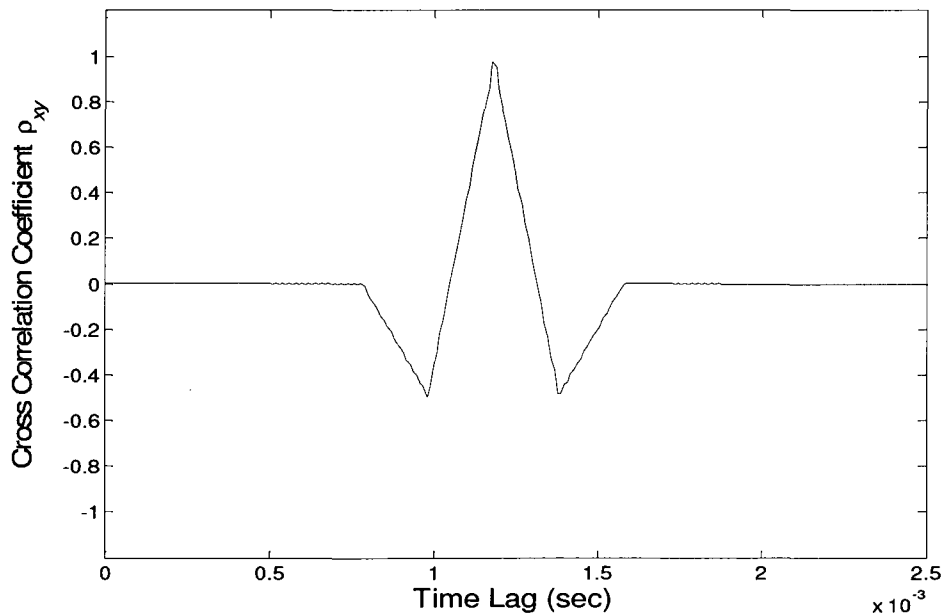


Figure (5.21): Cross-correlation coefficient of acceleration response to transient force

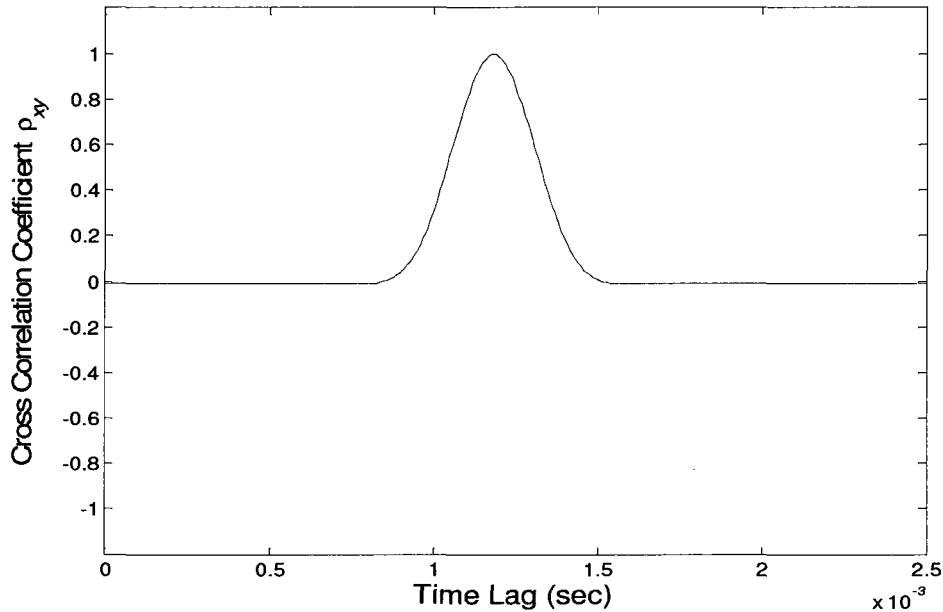


Figure (5.22): Cross-correlation coefficient of velocity response to transient force

5.3.3 Effect of Reflection

In the previous section, the responses were measured on a rod with absorbing boundary conditions. Hence the responses contained only the incident waves. In this section the effect of reflected waves on the cross-correlation analysis is explained. Three different boundary conditions are considered in this analysis:

- I. Rod with absorbing-fixed ends
- II. Rod with fixed-absorbing ends
- III. Rod with fixed-fixed ends

It should be mentioned that the force used in this analysis is a narrow-band force with central frequency $\omega_0 = 2\pi \times 6000$ and bandwidth $B = 2\pi \times 4000$, applied at the center of the rod.

I. Rod with absorbing-fixed ends

In this analysis c_1 is adjusted such that there is no reflection from the left boundary, and the value of k_2 is set to a very large number in order to simulate the fixity of the right support. Figure (5.23) shows the aforementioned configuration.

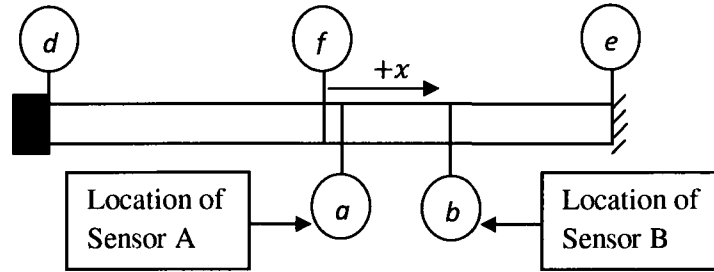


Figure (5.23): Model of rod with absorbing-fixed ends

As the force is applied at f , two non-dispersive waves start propagating: the forward wave ($x > 0$) and the backward wave ($x < 0$). The forward wave passes through ab , is reflected at e , again travels through ab and is damped out at d . The backward wave does not pass through path ab and is absorbed by the left support. Table (5.4) shows the calculations for the arrival time of incident and reflected waves at sensors A and B.

	Arrival of incident wave	Arrival of reflected wave
Sensor A	$fa/c = 0.00006 \text{ s}$	$(fe+ea)/c = 0.00586 \text{ s}$
Sensor B	$fb/c = 0.00124 \text{ s}$	$(fe+eb)/c = 0.00468 \text{ s}$

Table (5.4): Arrival time of incident and reflected waves in a rod with absorbing-fixed ends

In Table (5.4) c denotes the axial wave speed defined in Equation (5.21). Figure (5.24) shows the cross-correlation coefficient between the measurements at sensors A and B.

There are two peaks in this figure:

The first peak shows the time delay between the arrival of incident wave at sensors A and B. This peak also shows the time delay between the arrival of reflected wave at sensors A and B. This value, which is 0.00118 s, completely matches the calculated value shown in Table (5.4). The details of this peak are illustrated in Figure (5.25). One interesting aspect of this peak is the reduction of magnitude of the cross-correlation coefficient. This reduction happens because the incident wave travels from A to B while the reflected wave travels in the opposite direction.

The second peak, which is depicted in Figure (5.26) in more detail, occurs at .00462 s. This value is related to the time delay between the arrival of reflected wave at B and the incident wave at A. One interesting feature of Figure (5.26) is that the peak in it is negative: as the right end is a fixed support, the incident wave is reflected with a similar shape but inverted. Hence the cross-correlation coefficient of the incident wave and the reflected wave has a negative peak.

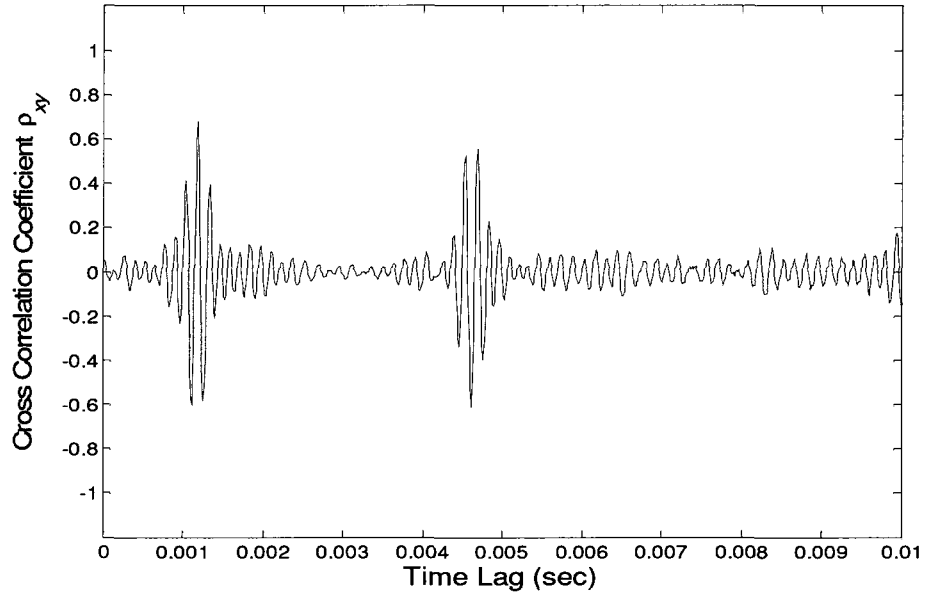


Figure (5.24): Cross-correlation coefficient of acceleration response in rod with absorbing-fixed ends

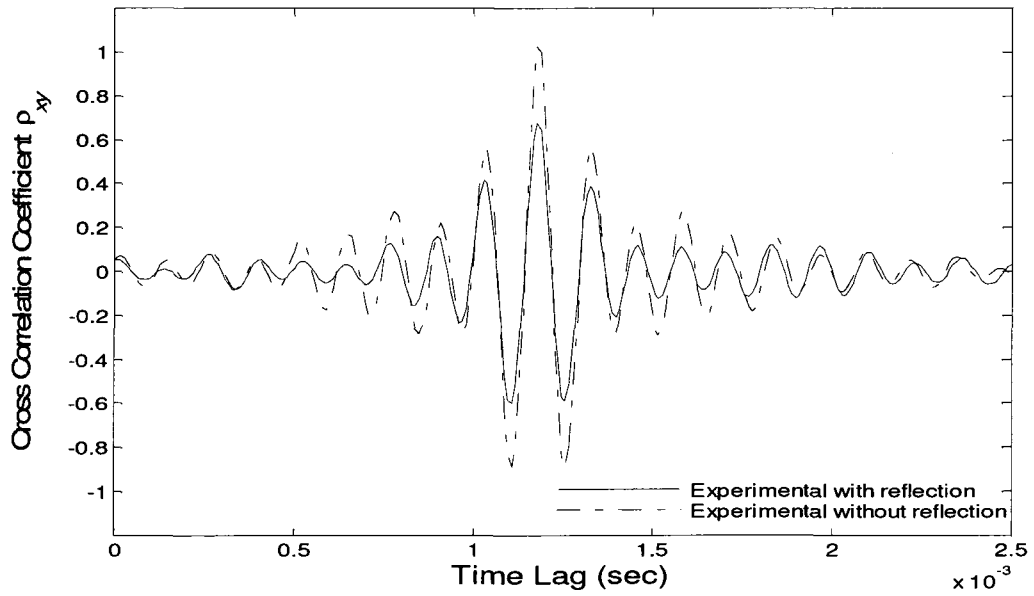


Figure (5.25): Cross-correlation coefficient of acceleration responses (first peak): comparison of rod with absorbing-absorbing and absorbing-fixed ends

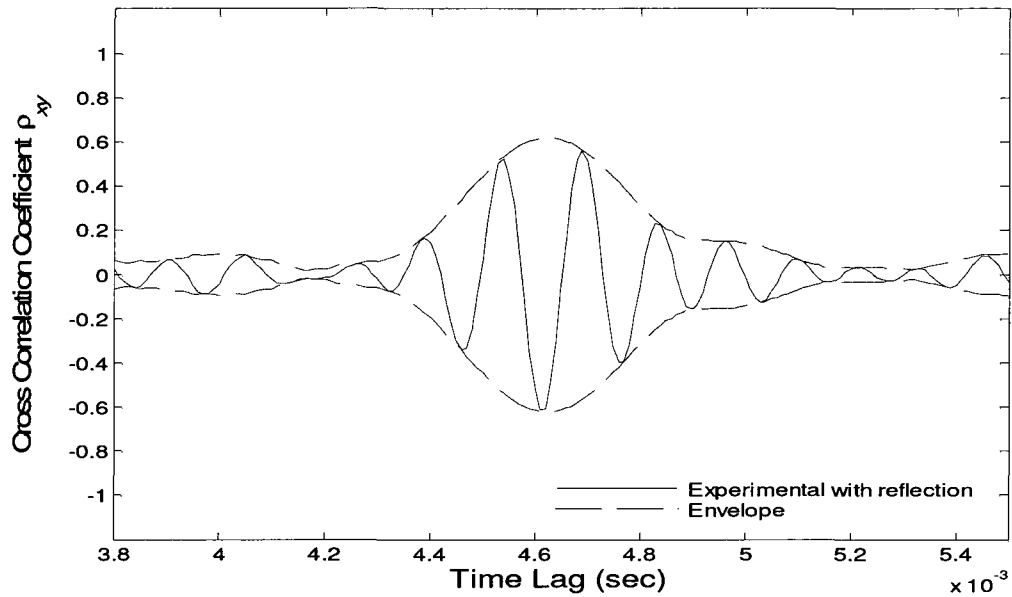


Figure (5.26): Cross-correlation coefficient of acceleration response in rod with absorbing-fixed ends (second peak)

II. Rod with fixed-absorbing ends

In this case the cross-correlation analysis is carried out on the responses of a rod with fixed-absorbing ends. The configuration of the rod is shown in Figure (5.27). When the rod is subjected to the given force at the middle, a forward wave ($x > 0$) starts progressing to the right side. This wave passes through the path ab once and is damped out at e . A backward wave ($x < 0$) reflects from the boundary at d , travels through ab and is absorbed at the right support. Table (5.5) shows the evaluation of time delay between locations a and b .

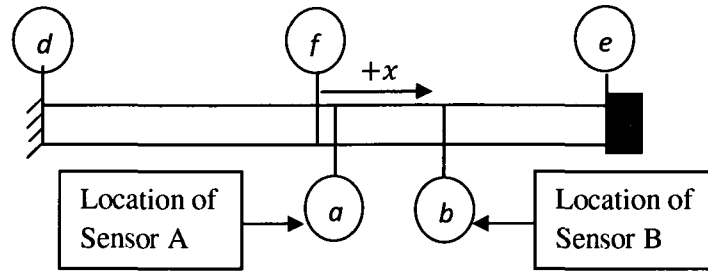


Figure (5.27): Model of rod with fixed-absorbing ends

	Arrival of incident wave	Arrival of reflected wave
Sensor A	$fa/c = 0.00006 \text{ s}$	$(fd+da)/c = 0.00598 \text{ s}$
Sensor B	$fb/c = 0.00124 \text{ s}$	$(fd+db)/c = 0.00716 \text{ s}$

Table (5.5): Arrival time of incident and reflected waves in a rod with fixed-absorbing ends

Figure (5.28) shows the cross-correlation coefficient of acceleration responses at A and B. This analysis reveals two distinct peaks.

The first peak identifies the time delay between the arrival of incident as well as reflected wave at locations a and b . The peak is located approximately at 0.00118 s, closely corresponding to the estimated time delay given in Table (5.5). The only difference with the previous case is in the amplitude of cross-correlation coefficient. Unlike the previous case, this amplitude does not show any change in magnitude because both the incident and reflected waves travel the path ab from sensor A to B. This fact is clarified in the Figure (5.29).

The second peak, which is at time 0.00710 s, occurs at the time lag between the arrival of the reflected wave at B and the incident wave at A. Like the previous case, as the reflected wave has the inverted form compared to the incident wave, the cross-correlation coefficient peak is negative. This fact is evident from Figure (5.30).

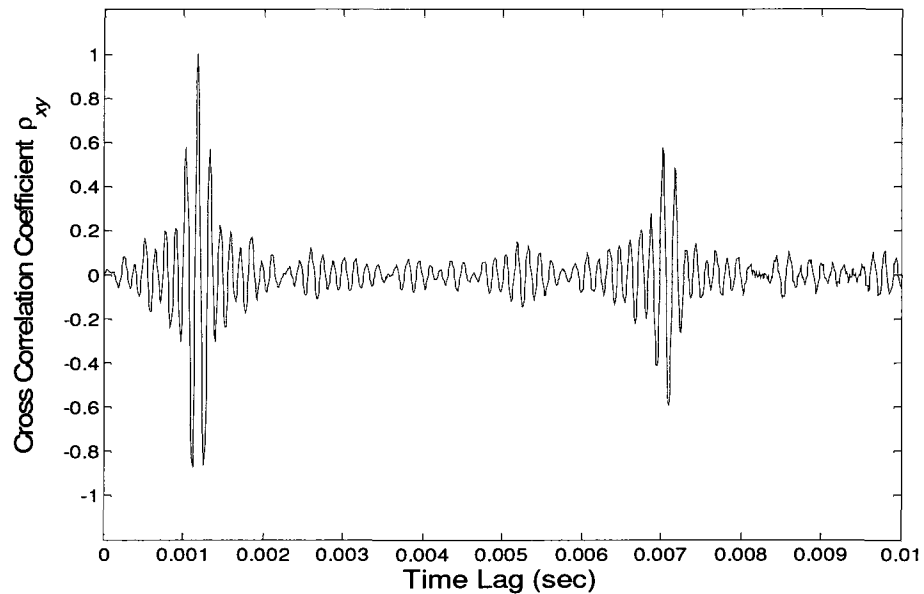
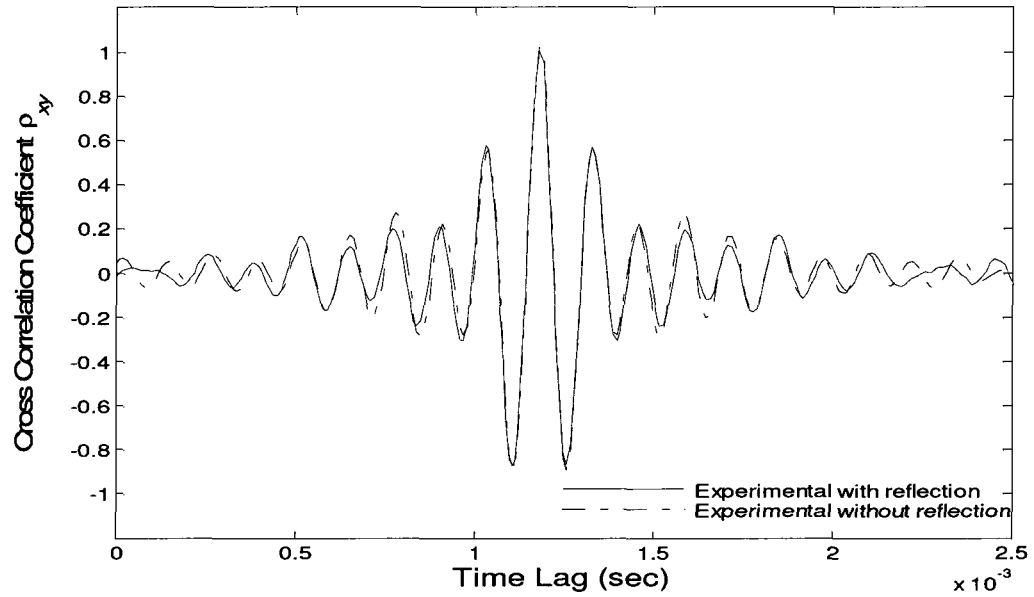


Figure (5.28): Cross-correlation coefficient of acceleration response in rod with fixed-absorbing ends



**Figure (5.29): Cross-correlation coefficient of acceleration responses (first peak):
comparison of rod with absorbing-absorbing and fixed-absorbing ends**

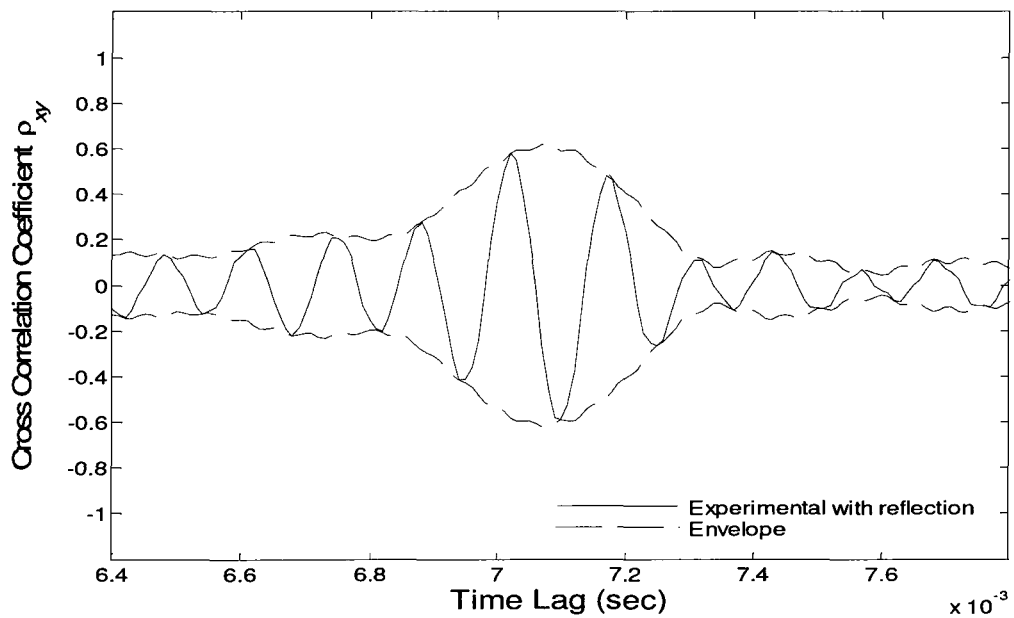


Figure (5.30): Cross-correlation coefficient of acceleration response in rod with fixed-absorbing ends (second peak)

III. Rod with fixed-fixed ends

In this section, cross-correlation analysis of acceleration responses of a rod with fixed-fixed ends is presented. The model of the rod is shown in Figure (5.31). As the rod starts vibrating, two incident waves are generated: the forward incident wave passes through ab and is reflected from supports e , while the backward wave travels the path fd and is reflected at d . Both reflected waves progress towards the center of the rod with inverted shapes. Table (5.6) shows the evaluation of time delay between acceleration measurements at sensors A and B.

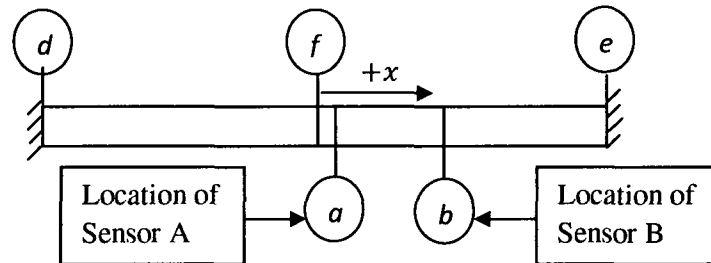


Figure (5.31): Model of rod with fixed-fixed ends

	Arrival of incident wave	Arrival of reflected wave	
		From left support	From right support
Sensor A	$fa/c = 0.00006 \text{ s}$	$(fd+da)/c = 0.00598 \text{ s}$	$(fe+ea)/c = 0.00586 \text{ s}$
Sensor B	$fb/c = 0.00124 \text{ s}$	$(fd+db)/c = 0.00716 \text{ s}$	$(fe+eb)/c = 0.00468 \text{ s}$

Table (5.6): Arrival time of incident and reflected waves in a rod with fixed-fixed ends

Figure (5.32) shows the results of cross-correlation between acceleration measurements at a and b . There are three peaks in that figure:

1. A positive peak at 0.00118 s which shows the time delay between the arrival of incident waves at sensors A and B. This value also corresponds to the time delay between arrivals of reflected waves at the sensors.
2. A negative peak at 0.00462 s which shows the time delay between the arrivals of reflected wave from right support at sensor B and the incident wave at sensor A.
3. A negative peak at 0.0071 s which shows the time delay between the arrivals of the reflected wave from left support at sensor B and the incident wave at sensor A.

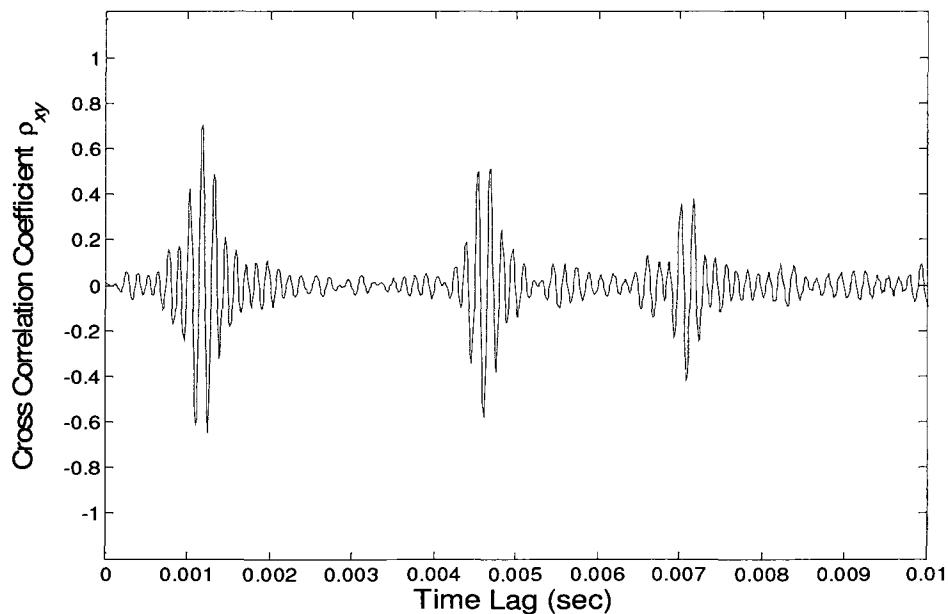


Figure (5.32): Cross-correlation coefficient of acceleration response in rod with fixed-fixed end

5.3.4 Effect of Noise

In this section the effect of noise on cross-correlation analysis is discussed. The noise level associated with the measurements is expressed by

$$R = \frac{\sigma}{\max(x(t))} \quad (5.23)$$

in which $x(t)$ is the measurement, σ is the rms value of the measurement noise and R is the noise level. The measurement noise obtained by using the function *randn* in MATLAB software is one sample of normally distributed random variable. Any two samples of generated random noise are expected to be almost uncorrelated. Fully uncorrelation may not be achieved because the samples represent finite and discrete measurement noise. The low degree of correlation forms the basis for formulation derived in chapter 3.

The model chosen in this section is a fixed-fixed rod as depicted in Figure (5.31). It may be recalled that Figure (5.32) shows the results of cross-correlation analysis of the clean acceleration responses at sensors A and B. In order to compare the effect of noise two different levels of noise, $R=15\%$ and $R=30\%$, are considered here. Figure (5.33) illustrates a sample of the acceleration response at sensor A, while Figure (5.34) shows the same quantity for sensor B. Figure (5.35) shows the corresponding autospectral density functions.

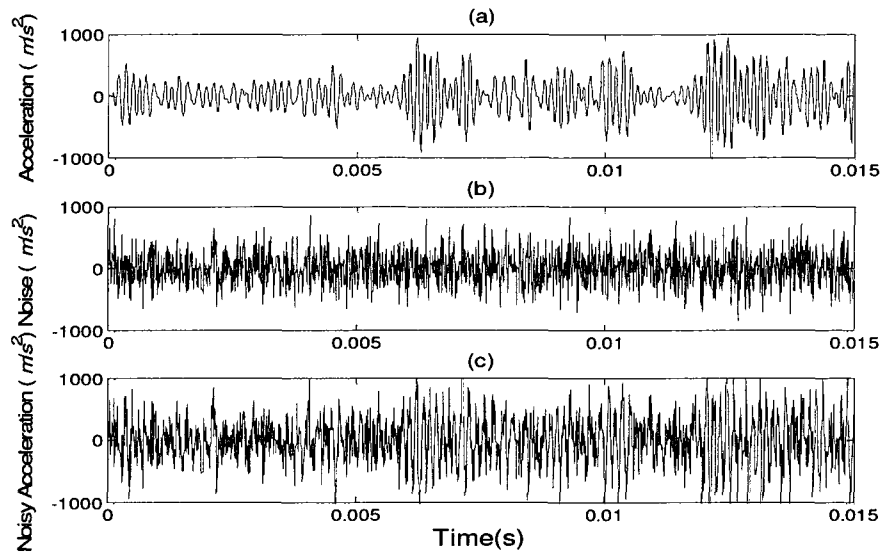


Figure (5.33): Response at sensor A a) acceleration b) noise (R=30%) c) noisy acceleration

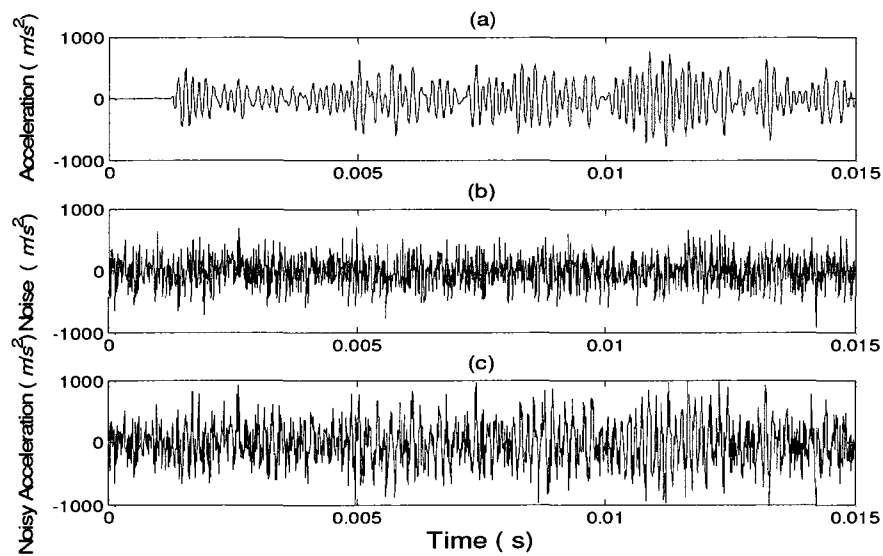
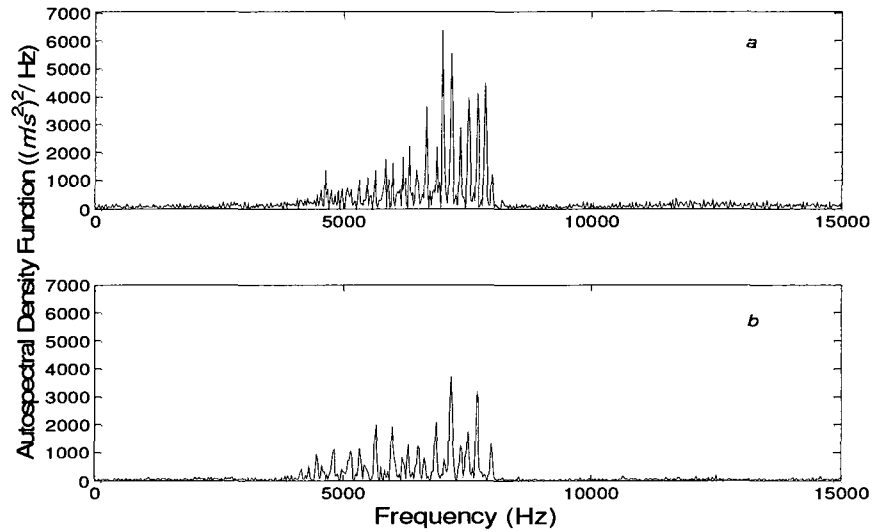


Figure (5.34): Response at sensor B a) acceleration b) noise (R=30%) c) noisy acceleration



**Figure (5.35): Autospectral density function of noisy acceleration ($R=30\%$) response at
a) sensor A b) sensor B**

Cross-correlation coefficient of the acceleration measurements with 30% noise is given in Figure (5.36). As can be noted from the figure, even in the presence of 30% noise, the time delays are accurately estimated with less than 1% error. Figures (5.37), (5.38) and (5.39) show the identified peaks in more detail. These figures also compare the effect of different levels of noise on the cross-correlation coefficients. The following important conclusion can be drawn from the results shown:

As the level of noise increases, the amplitude of the cross-correlation coefficient decreases but the time delay is accurately predicted.

In order to remove the effect of noise, the cross-correlation function can be used instead of the cross-correlation coefficient. As discussed in Section 3.2.2, the normalization factors in the cross-correlation coefficient depend on the level of noise while the

cross-correlation function is independent of noise. Figures (5.40), (5.41) and (5.42) clarify this fact.

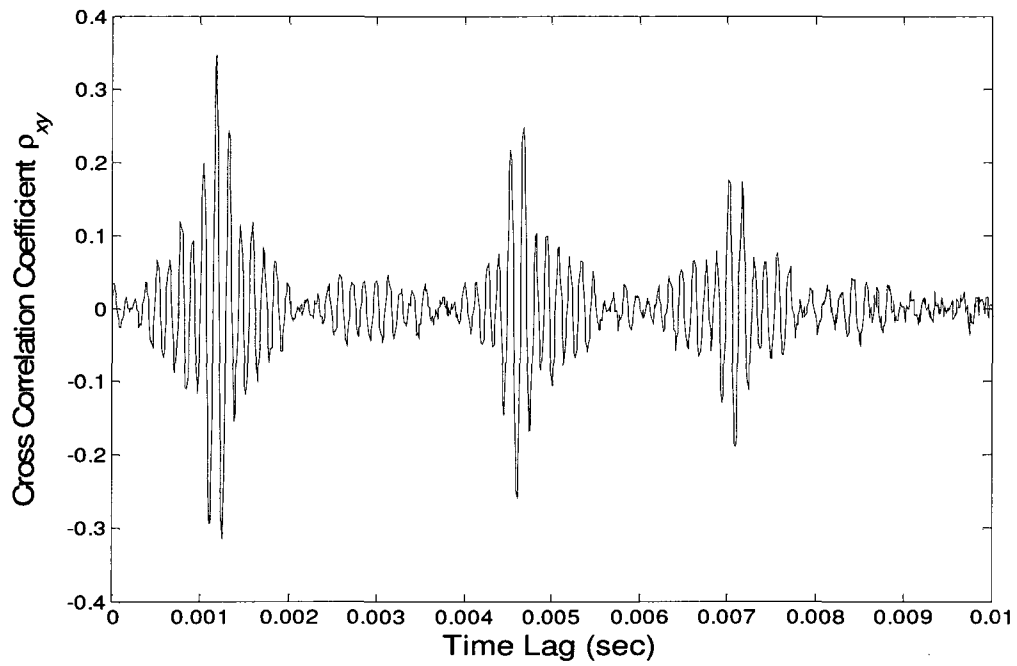


**Figure (5.36): Cross-correlation coefficient of acceleration response
in presence of 30% noise**

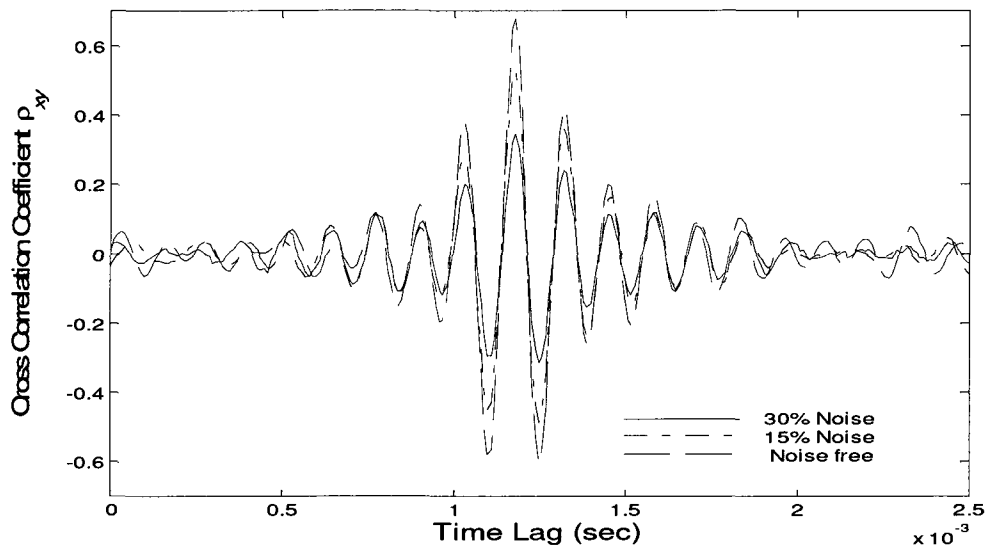


**Figure (5.37): Cross-correlation coefficient between noisy acceleration measurements:
comparison of the effect of different levels of noise on first peak**

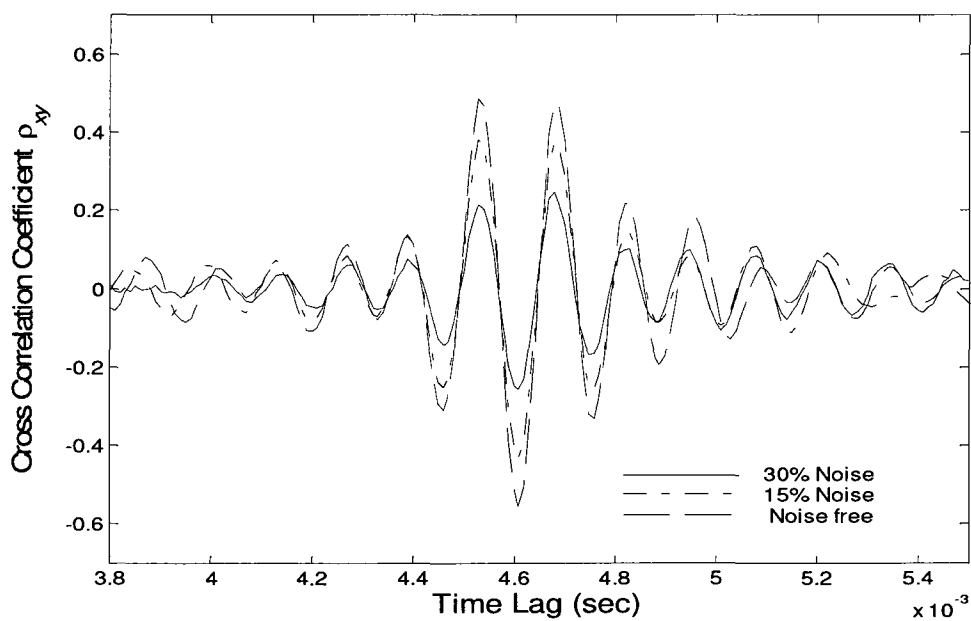


**Figure (5.38): Cross-correlation coefficient between noisy acceleration measurements:
comparison of the effect of different levels of noise on second peak**

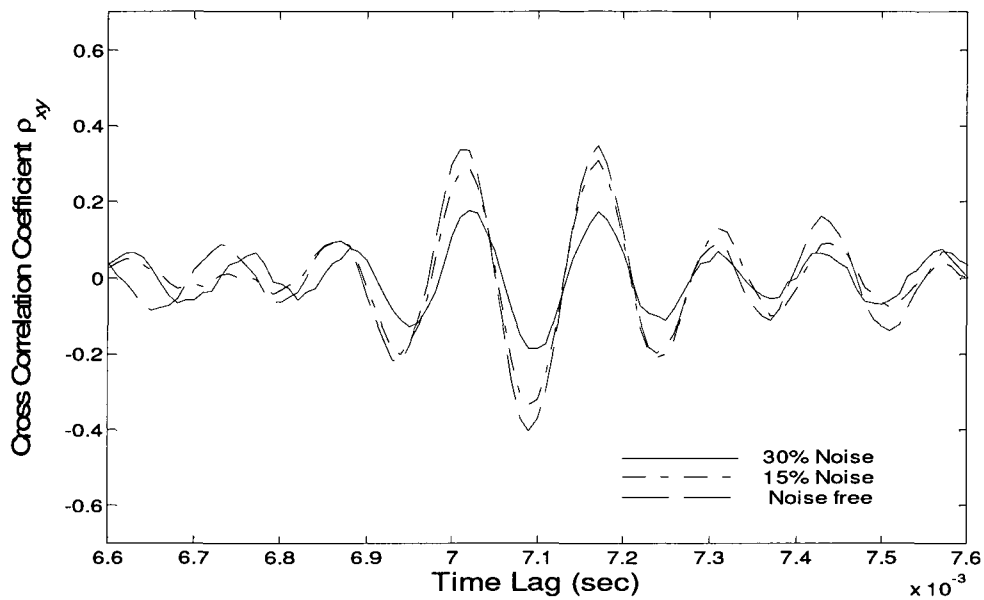


**Figure (5.39): Cross-correlation coefficient between noisy acceleration measurements:
comparison of the effect of different levels of noise on third peak**

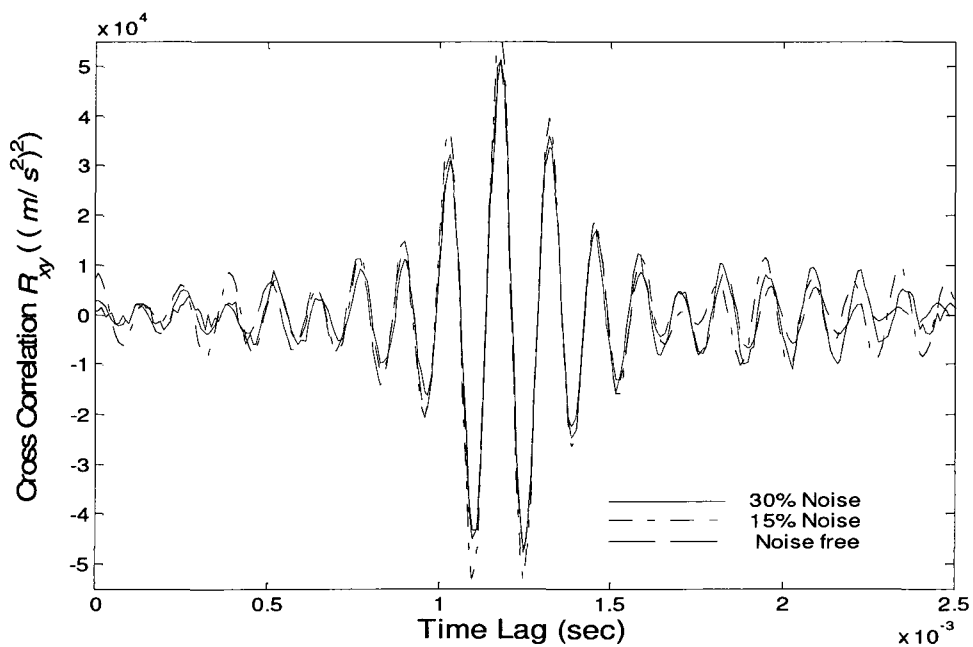


**Figure (5.40): Cross-correlation function between noisy acceleration measurements:
comparison of the effect of different levels of noise on first peak**

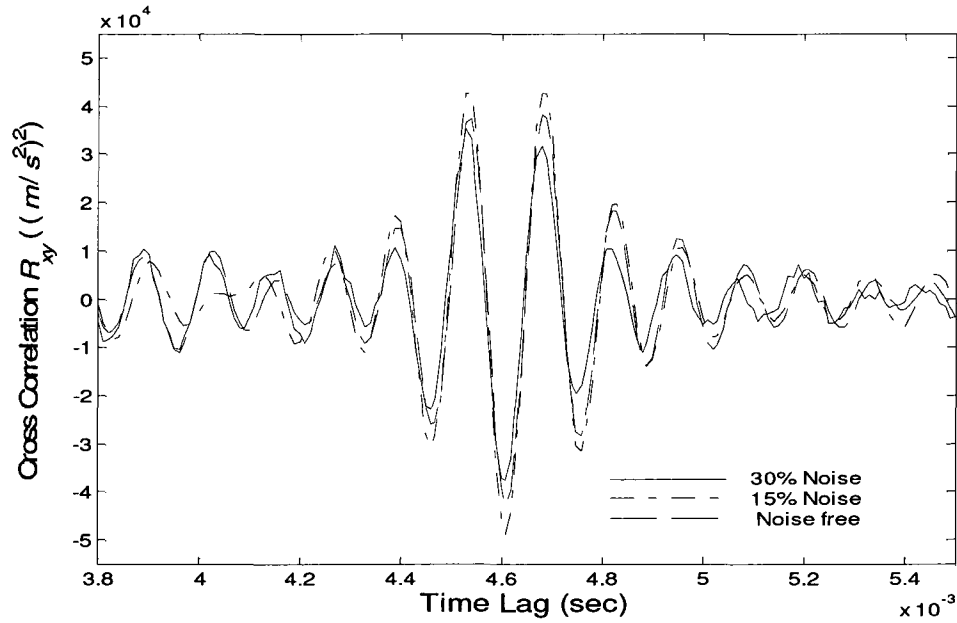


**Figure (5.41): Cross-correlation function between noisy acceleration measurements:
comparison of the effect of different levels of noise on second peak**

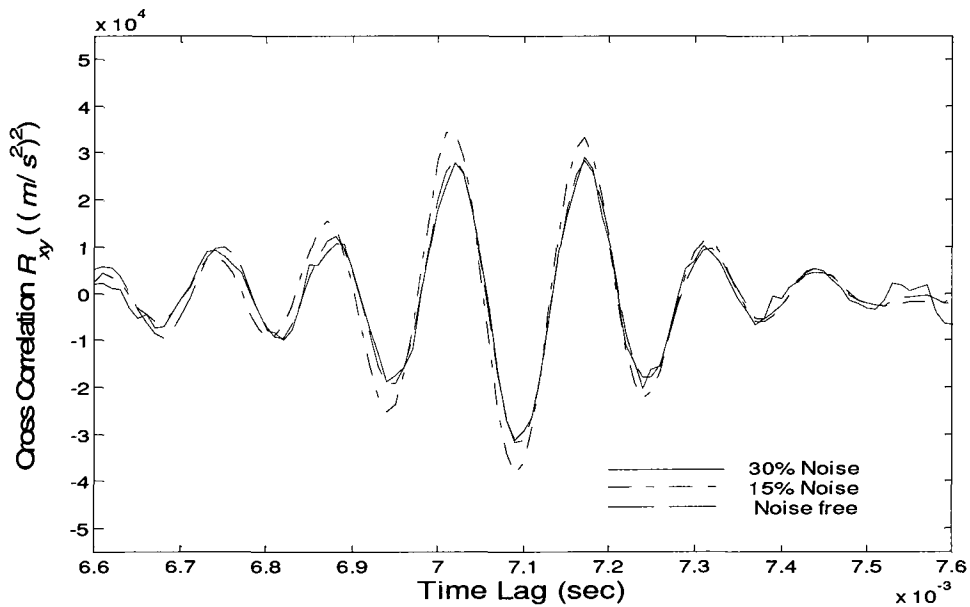


**Figure (5.42): Cross-correlation function between noisy acceleration measurements:
comparison of the effect of different levels of noise on third peak**

5.4 Damage Detection

In this section, cross-correlation analysis is used as a tool to detect damage in a rod. The responses of the rod with fixed supports are measured at two sensors A and B, which are shown in Figure (5.9). It is assumed that the damage occurs at three different locations:

- Left side of sensor A
- Right side of sensor B
- Between sensors A and B

The damage is characterized by the length L_d denoting the spatial extent of damage and the quantity of damage s , that refers to the percentage of reduction in the axial stiffness of the rod within the damage length L_d . In this analysis, it is assumed that there is no change in the mass of the rod. Based on these assumptions, the wave speed in the length L_d is given by

$$c_d = \sqrt{\frac{(EA)_d}{\bar{m}}} = \sqrt{\frac{(1-s)EA}{\bar{m}}} = \sqrt{1-s} \cdot c \quad (5.24)$$

where c and c_d are the axial wave speed in the undamaged and damaged area of rod respectively. It should be mentioned that all the measurements used in this analysis are corrupted by 30% noise.

5.4.1 Damage on the Left Side of Sensor A

The model used in this analysis is shown in Figure (5.43). The location where the force is applied is close to sensor A, so it is assumed that damage occurs to the left of this location.

In this analysis, two scenarios are considered:

- I. Damage length is 2.5 m ($L_d = 2.5$ m).
- II. Damage length is 1 m ($L_d = 1$ m).

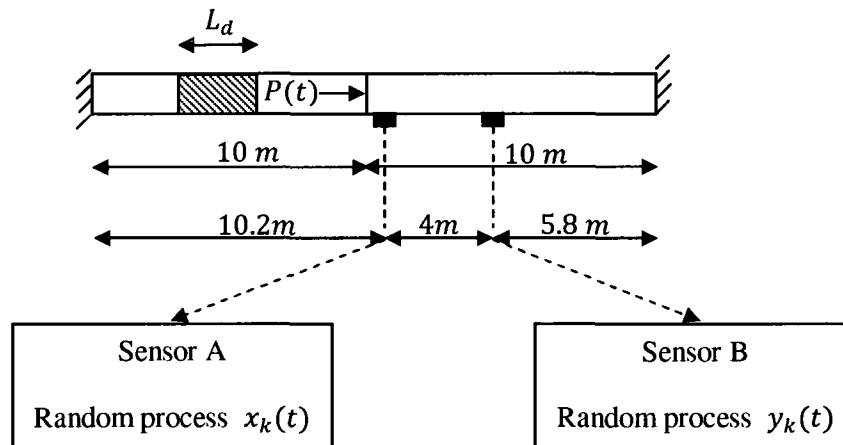


Figure (5.43): Model of rod with damage at left side of sensor A

I. Damage length 2.5 m

The cross-correlation function for the acceleration measurements at sensors A and B with 10% damage and in presence of 30% noise is illustrated in Figure (5.44). This figure shows three distinct peaks. These peaks are illustrated in greater detail in Figures (5.45), (5.46) and (5.47). These figures also show a comparison of the effect of different amounts of damage.

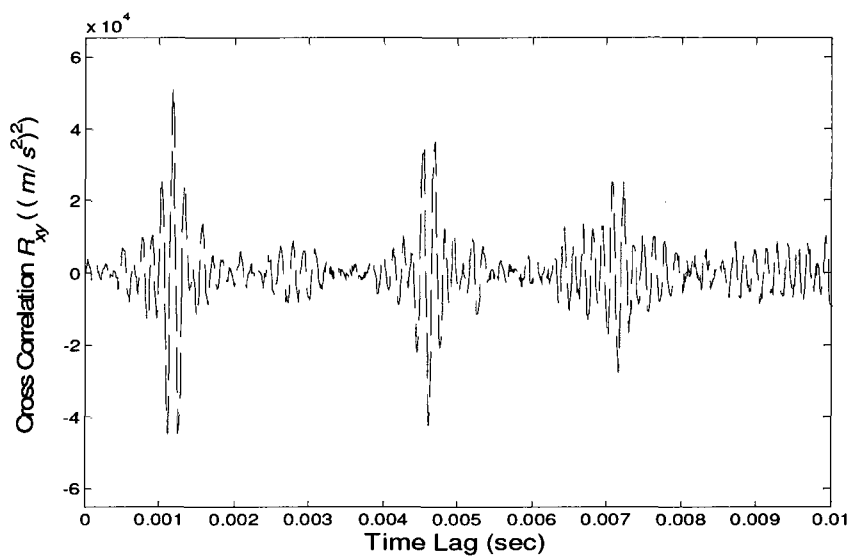


Figure (5.44): Cross-correlation function of acceleration measurements: 10% damage on the left side of sensor A (damage length 2.5 m)

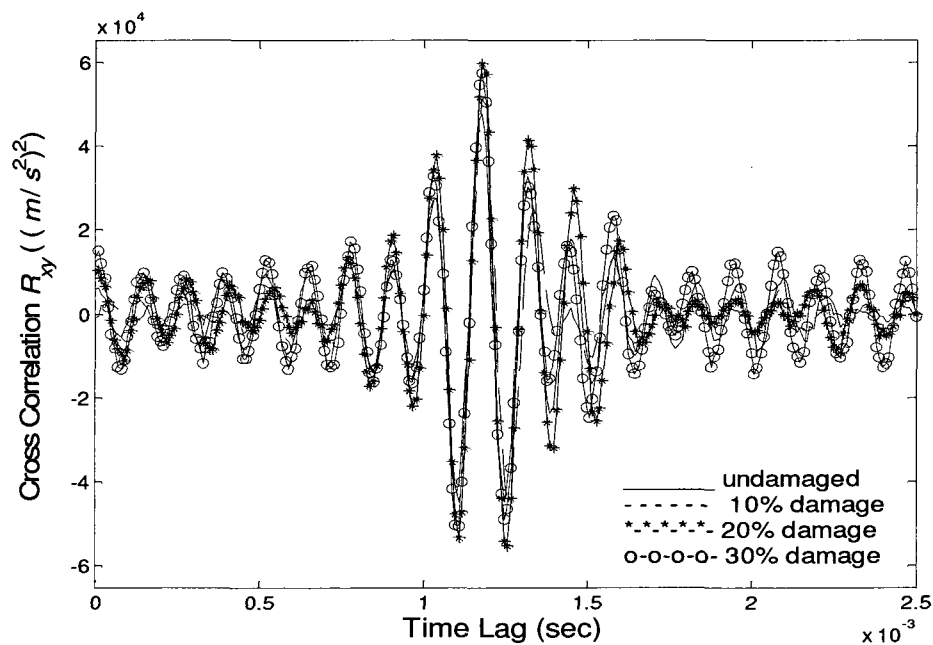


Figure (5.45): Cross-correlation function of acceleration measurements: comparison of the effect of different damage extent on the first peak (damage length 2.5 m)

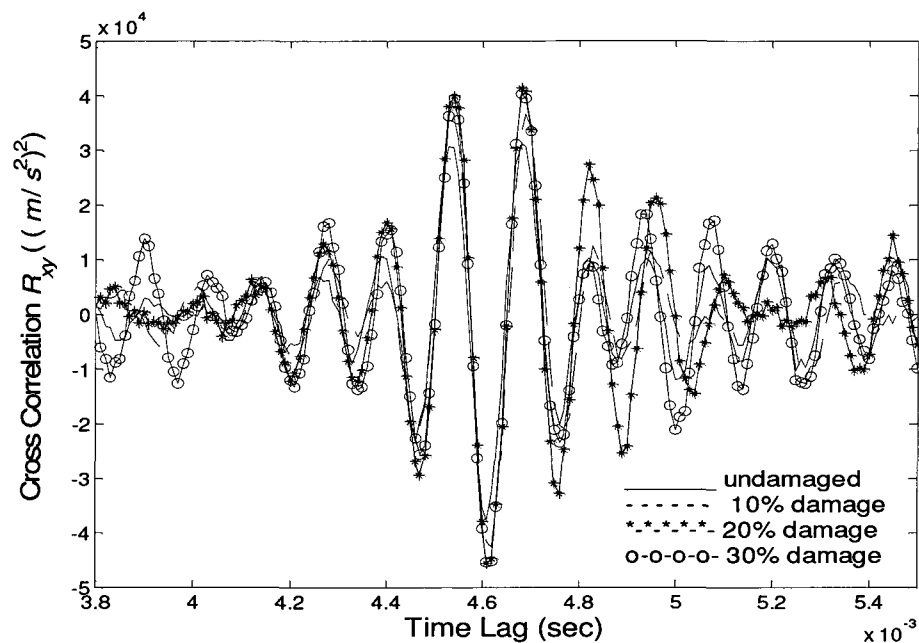


Figure (5.46): Cross-correlation function of acceleration measurements: comparison of the effect of different damage extent on the second peak (damage length 2.5 m)

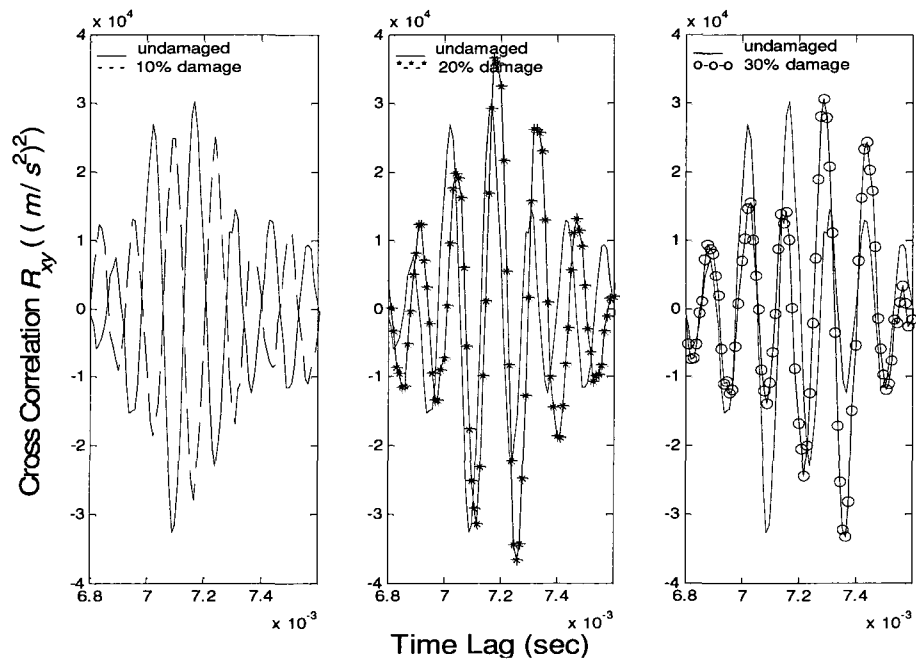


Figure (5.47): Cross-correlation function of acceleration measurements: comparison of the effect of different damage extent on the third peak (damage length 2.5 m)

The interesting properties observed from these figures are summarized in the following:

- The first peak of cross-correlation function, which shows the time delay between the arrival of wave at sensors A and B (incident or reflected), remains unchanged
- The second peak of cross-correlation function, which shows the time delay between the arrival of incident wave at sensor A and the arrival at B of the wave reflected from the right hand end, remains unchanged.
- The third peak of cross-correlation function, which shows the time delay between the arrival of incident wave at sensor A and the arrival at B of the wave reflected from the left hand end of the rod, has shifted on account of the damage and the shift depends on the amount of damage.
- Increase in damage extent results in longer shifts in time delays. This shows that time delay shifts are proportional to the extent of damage. This fact could be an indicator of the prediction of damage severity.

Based on the foregoing observations it can be concluded that:

- Damage occurs at the left side of sensor A.
- Different amounts of damage reflect different amounts of time delay shifts appearing in the correlation function. The more severe the damage is, the longer the shift in the time delay estimation.

In order to relate the time delay shifts to the extent of damage, the following steps are carried out:

The time delay in the damaged rod is written in terms of the speed of acceleration wave in undamaged and damaged area using Equation (5.24). Table (5.7) shows these

calculations. On the other hand the, time delays in the damaged rod are detected from the peaks of cross-correlation functions, as shown by Figure (5.44). The comparison of the calculated and detected time delays results in an estimation of the damage extent. Table (5.8) shows the damaged extent results. It should be noted that in Tables (5.7) and (5.8), the time delay is calculated for two cases: in the first case it is assumed that the damage length is known $L_d = 2.5 \text{ m}$. In the second case, it is assumed that the entire length on the left side of force is damaged; hence the value of the extent of damage represents the minimum of the possible damage extent on the left side of sensor.

	Arrival of the incident wave at sensor A	Arrival of reflected wave from left support at sensor B		Calculated time delay	
		Known damage length	Unknown damage length	Known damage length	Unknown damage length
Undamaged	$\frac{0.2}{c} = 0.00006 \text{ s}$	$\frac{24.2}{c} = 0.00716 \text{ s}$	$\frac{24.2}{c} = 0.00716 \text{ s}$	0.00710 s	0.00710 s
Damaged	$\frac{0.2}{c} = 0.00006 \text{ s}$	$\frac{19.2}{c} + \frac{5}{(\sqrt{1-s})c}$	$\frac{4.2}{c} + \frac{20}{(\sqrt{1-s})c}$	$\frac{19}{c} + \frac{5}{(\sqrt{1-s})c}$	$\frac{4}{c} + \frac{20}{(\sqrt{1-s})c}$

Table (5.7): Calculation of time delay in undamaged and damaged rod (damage length 2.5 m)

	Time delay estimation	Extent of damage	
		Known damaged length	Unknown damaged length
Damage case 1 (s=10%)	0.00717 s	8.5%	2.22%
Damage case 2 (s=20%)	0.00726 s	18.3%	5.1%
Damage case 3 (s=30%)	0.00737 s	28.2%	8.4%

Table (5.8): Calculation of damage extent in damaged rod (damage length 2.5 m)

II. Damage length 1 m

In this case the damage is introduced in a 1 m length on the left side of sensor A. Similar to the previous case, the cross-correlation function of the two acceleration measurements at A and B show three distinct peaks. The first and second peaks remain unchanged but the third peak exhibits varying amounts of shifts caused by different amounts of damage.

Figure (5.48) shows this fact.

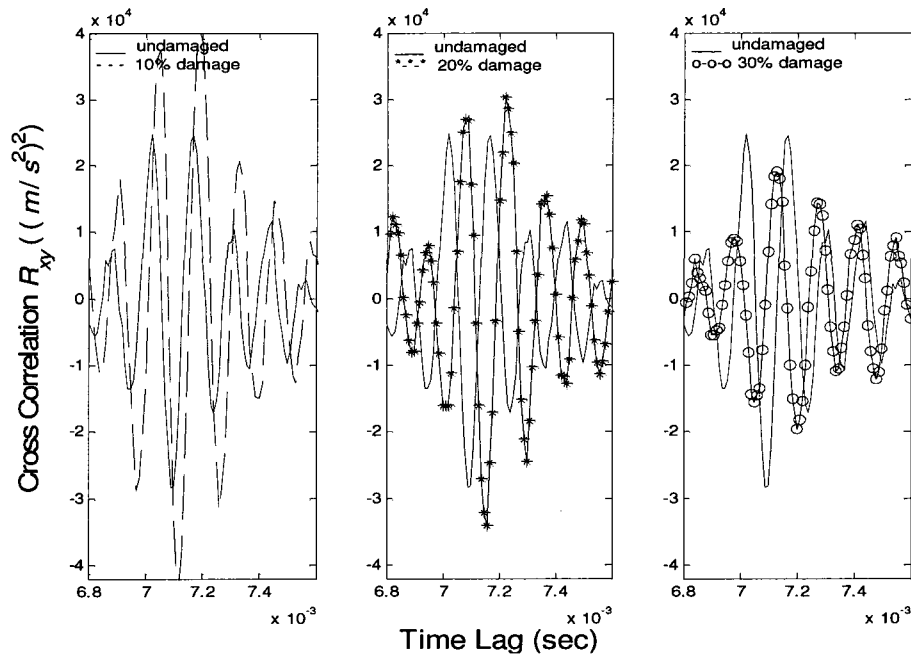


Figure (5.48): Cross-correlation function of acceleration measurements: comparison of the effect of different damage extent on the third peak (damage length 1 m)

In order to estimate the damage extent, a procedure similar to that in the previous case is carried out. Table (5.9) and Table (5.10) show the results.

	Arrival of the incident wave at sensor A	Arrival of reflected wave from left support at sensor B		Calculated time delay	
		Known damage length	Unknown damage length	Known damage length	Unknown damage length
Undamaged	$\frac{0.2}{c} = 0.00006 \text{ s}$	$\frac{24.2}{c} = 0.00716 \text{ s}$	$\frac{24.2}{c} = 0.00716 \text{ s}$	0.0071 s	0.0071 s
Damaged	$\frac{0.2}{c} = 0.00006 \text{ s}$	$\frac{22.2}{c} + \frac{2}{(\sqrt{1-s})c}$	$\frac{4.2}{c} + \frac{20}{(\sqrt{1-s})c}$	$\frac{22}{c} + \frac{2}{(\sqrt{1-s})c}$	$\frac{4}{c} + \frac{20}{(\sqrt{1-s})c}$

Table (5.9): Calculation of time delay in undamaged and damaged rod (damage length 1m)

	Time delay estimation	Extent of damage	
		Known damaged length	Unknown damaged length
Damage case 1 (s=10%)	0.00712 s	5.5%	0.6%
Damage case 2 (s=20%)	0.00716 s	16.8%	1.9%
Damage case 3 (s=30%)	0.00720 s	26.2%	3.2%

Table (5.10): Calculation of damage extent in damaged rod (damage length 1m)

From the analyses performed in this section, the following conclusions can be drawn:

1. Any dynamical property change on the left side of sensor A will appear as a change in the time delay which is related to reflection from left support. This characteristic is a crude indicator of damage location.
2. According to Table (5.8) and Table (5.10), if an estimate of the damage length already exist, time delay shifts will provide an fairly accurate estimate of the damage extent. In reality however providing any information about the damage length prior to an experiment is quite difficult. In that case the entire length of the

propagation path between two sensors, or between sensors and supports can be used to obtain a rough estimate of the damage extent.

3. In this study only two sensors are used to measure the dynamic responses. In order to have a better estimation of damage location and damage extent, more measurement points would be necessary.

5.4.2 Damage on the Right Side of Sensor B

In this section, it is assumed that the damage occurs on the right side of the sensor B. Figure (5.49) shows the configuration of the damage.

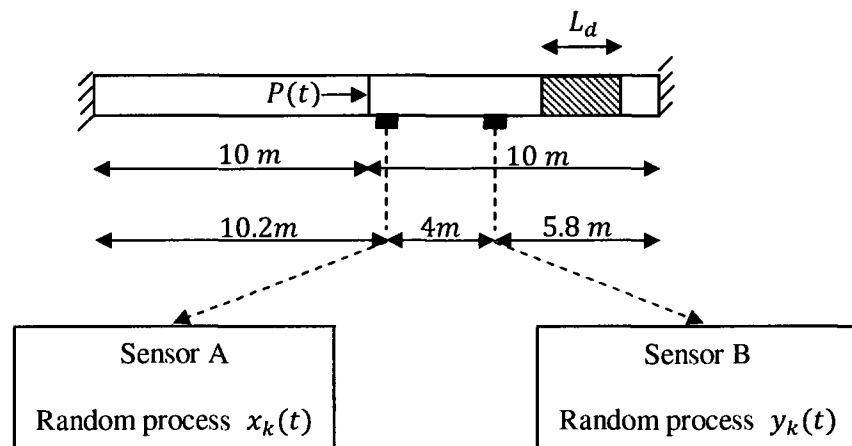


Figure (5.49): Model of rod with damage on right side of sensor B

Similar to previous section, two scenarios will be discussed:

- I. Damage length is 2.5 m ($L_d = 2.5$ m).
- II. Damage length is 1 m ($L_d = 1$ m).

I. Damage length 2.5 m

Cross-correlation function of the acceleration measurements at sensors A and B is shown in Figure (5.50). Three peaks exist in this figure:

1. The first peak which shows the time delay between arrival of the incident wave or reflected waves at sensor locations A and B.
2. The second peak which shows the time lag between the arrival of incident wave at A and the arrival of the wave after reflection from the left support at B.
3. The third peak which shows the time delay between the arrival of incident wave at A and the arrival at B of a wave after reflection from the right boundary.

Figure (5.51) shows that the damage does not cause the first peak to shift along the time delay axis. Hence it can be concluded that damage does not occur between the two measurements locations. Unchanged location of third peak, which is depicted in Figure (5.52), implies that damage does not affect the response after reflection of the wave from the left boundary. Hence there is no induced damage in that area. But, as shown by the results presented in Figure (5.53), the second peak, which reflects the properties of the right side of sensor B, moves along the time axis, the extent of movement depending on the level of damage. The longer time delay in this path reveals a greater reduction in the wave speed. Since wave speed is proportional to square root of axial stiffness of the rod, the reduction in axial stiffness can be estimated. This dynamic property change is interpreted as damage.

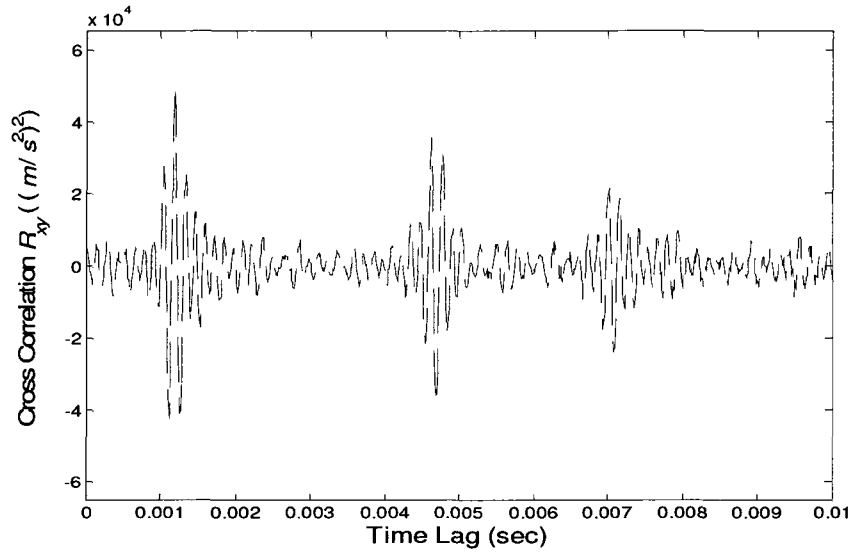


Figure (5.50): Cross-correlation function of acceleration measurements: 10% damage on the right side of sensor B (damage length 2.5 m)

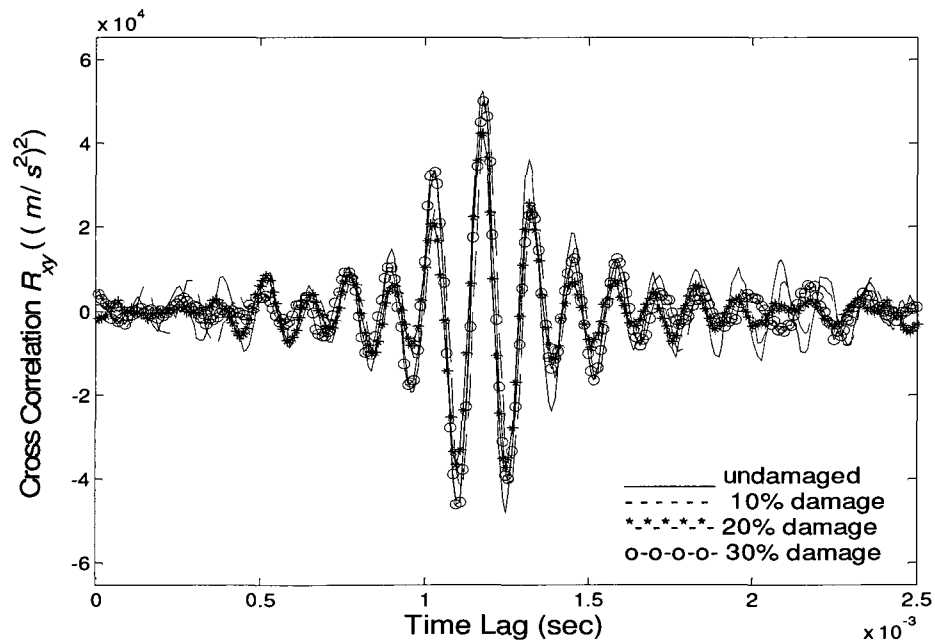


Figure (5.51): Cross-correlation function of acceleration measurements: comparison of the effect of different damage extent on the first peak (damage length 2.5 m)

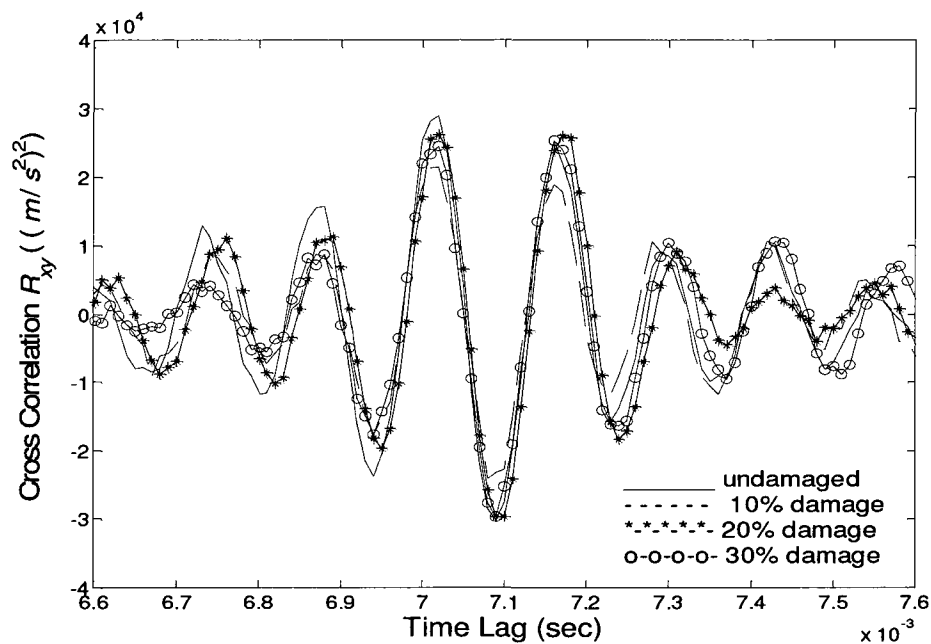


Figure (5.52): Cross-correlation function of acceleration measurements: comparison of the effect of different damage extent on the third peak (damage length 2.5 m)

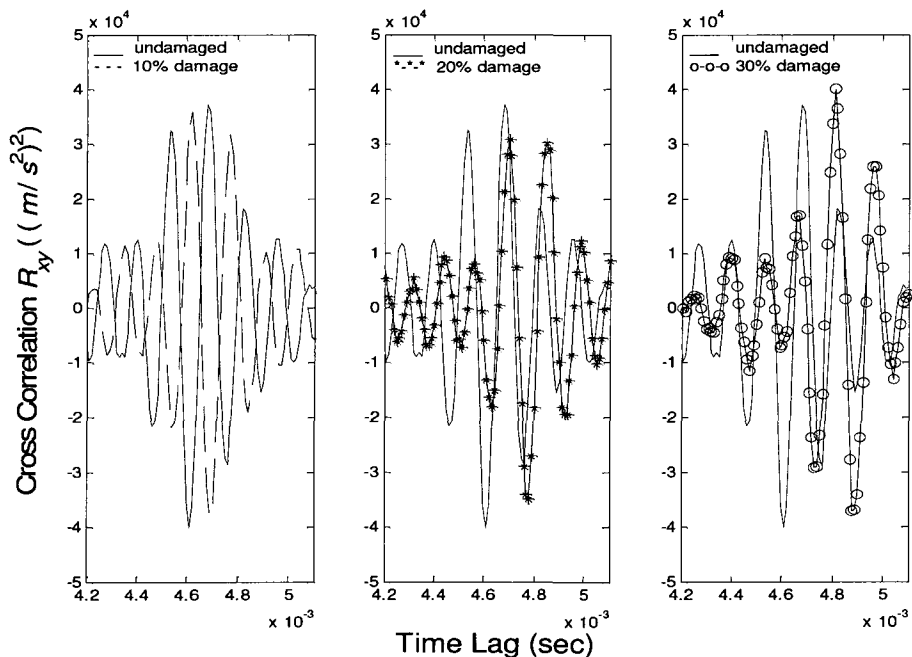


Figure (5.53): Cross-correlation function of acceleration measurements: comparison of the effect of different damage extent on the second peak (damage length 2.5 m)

Following the procedure outlined in Section 5.4.1, the extent of damage can be estimated as shown in Tables (5.11) and (5.12).

	Arrival of the incident wave at sensor A	Arrival of reflected wave from right support at sensor B		Calculated time delay	
		Known damage length	Unknown damage length	Known damage length	Unknown damage length
Undamaged	$\frac{0.2}{c} = 0.00006 \text{ s}$	$\frac{15.8}{c} = 0.00468 \text{ s}$	$\frac{15.8}{c} = 0.00468 \text{ s}$	0.00462 s	0.00462 s
Damaged	$\frac{0.2}{c} = 0.00006 \text{ s}$	$\frac{10.8}{c} + \frac{5}{(\sqrt{1-s})c}$	$\frac{4.2}{c} + \frac{11.6}{(\sqrt{1-s})c}$	$\frac{10.6}{c} + \frac{5}{(\sqrt{1-s})c}$	$\frac{4}{c} + \frac{11.6}{(\sqrt{1-s})c}$

Table (5.11): Calculation of time delay in undamaged and damaged rod (damage length 2.5 m)

	Time delay estimation	Extent of damage	
		Known damaged length	Unknown damaged length
Damage case 1 (s=10%)	0.00469 s	9.2%	4.1%
Damage case 2 (s=20%)	0.00478 s	18.9%	8.9%
Damage case 3 (s=30%)	0.00488 s	27.9%	13.7%

Table (5.12): Calculation of damage extent in damaged rod (damage length 2.5 m)

II. Damage length 1 *m*

In this scenario, it is assumed that the damage length is 1 *m*. Thus the severity of damage is less than in the previous case. The analysis in this section clarifies how much the time delay and wave speed are sensitive to small magnitudes of damage.

As in Figure (5.50), the cross-correlation analysis between the acceleration measurements at A and B, shows three different peaks. While the first and third peaks do not show any change, the second peak shifts, the amount of shift depending on the level of damage. Figure (5.54) shows these displacements along the time axis. Tables (5.13) and (5.14) show the calculation of damage extent for two cases: first when the damage length is already known, second when the whole propagation path is considered as the damage length.

Referring to the analyses presented in this section, it is worth noting that

1. Any dynamical changes on the right side of sensor B only changes the time delay which corresponds to reflections from the right support.
2. 10% damage in 1 *m* of rod is a damage of very small magnitude. Detection of this kind of damage is a very difficult problem in the field of damage detection. Here also, as can be seen from Figure (5.54), time delay shift caused by this small amount of damage is very difficult to detect. But when the amount of stiffness reduction is substantial, the approach presented here appears to be a promising tool for the identification of local damage.

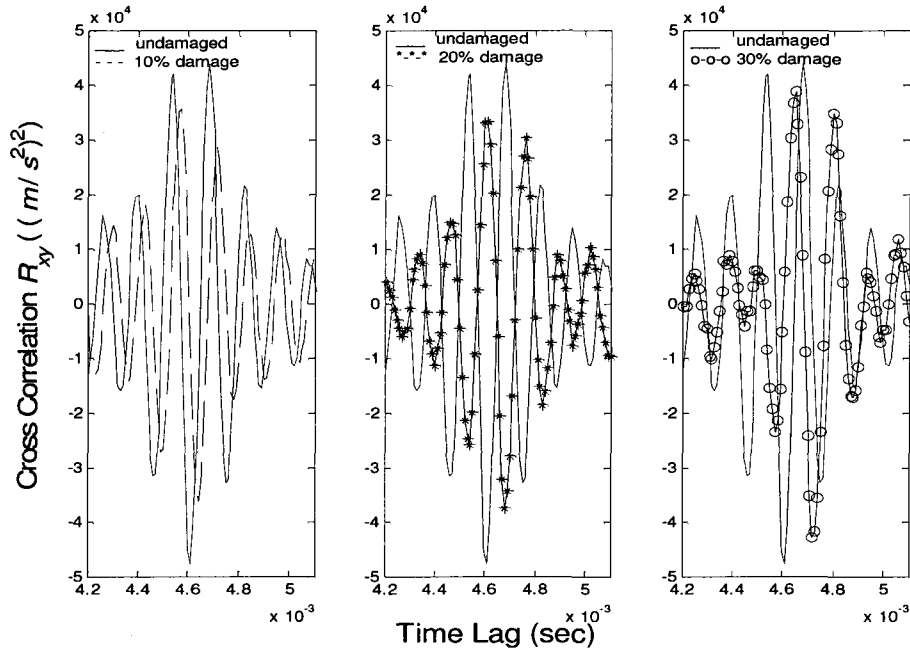


Figure (5.54): Cross-correlation function of acceleration measurements: comparison of the effect of different damage extent on the second peak (damage length 1 m)

	Arrival of the incident wave at sensor A	Arrival of reflected wave from right support at sensor B		Calculated time delay	
		Known damage length	Unknown damage length	Known damage length	Unknown damage length
Undamaged	$\frac{0.2}{c} = 0.00006 \text{ s}$	$\frac{15.8}{c} = 0.00468 \text{ s}$	$\frac{15.8}{c} = 0.00468 \text{ s}$	0.00462 s	0.00462 s
Damaged	$\frac{0.2}{c} = 0.00006 \text{ s}$	$\frac{13.8}{c} + \frac{2}{(\sqrt{1-s})c}$	$\frac{4.2}{c} + \frac{11.6}{(\sqrt{1-s})c}$	$\frac{13.6}{c} + \frac{5}{(\sqrt{1-s})c}$	$\frac{4}{c} + \frac{11.6}{(\sqrt{1-s})c}$

Table (5.13): Calculation of time delay in undamaged and damaged rod (damage length 1 m)

	Time delay estimation	Extent of damage	
		Known damaged length	Unknown damaged length
Damage case 1 (s=10%)	0.00464 s	7.4%	1.3%
Damage case 2 (s=20%)	0.00468 s	18.3%	3.6%
Damage case 3 (s=30%)	0.00472 s	27.5%	5.8%

Table (5.14): Calculation of damage extent in damaged rod (damage length 1 m)

5.4.3 Damage Between Sensors A and B

This section of Chapter 5 is devoted to a study of the effect of damage on cross-correlation function when the damage occurs between the measurement locations.

The model for this problem is presented in Figure (5.55).

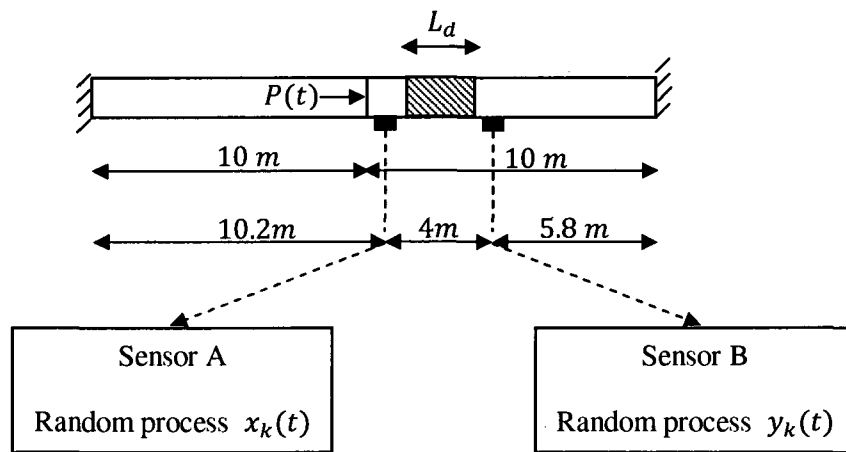


Figure (5.55): Model of damage between sensors A and B

In the analysis of this section, two scenarios are considered:

- I. Damage length is 2.5 m .
- II. Damage length is 1 m .

I. Damage length 2.5 m

The cross-correlation function for the acceleration measurements at sensors A and B, in presence of 30% noise, and damage in 2.5 m of the 4 m length of AB, is depicted in Figure (5.56). This figure shows three different peaks which are illustrated in more details in Figure (5.57), Figure (5.58) and Figure (5.59). As illustrated in these figures, all the peaks are shifted, the amount of shift depending on the magnitude of damage. Tables (5.15), (5.16) and (5.17) show the calculation of damage extent.

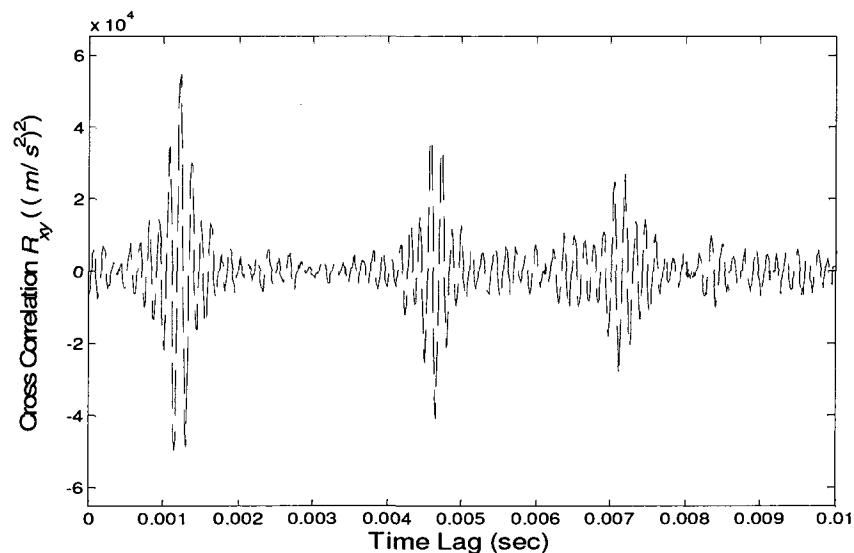


Figure (5.56): Cross-correlation function of acceleration measurements: 10% damage between sensor A and B (damage length 2.5 m)

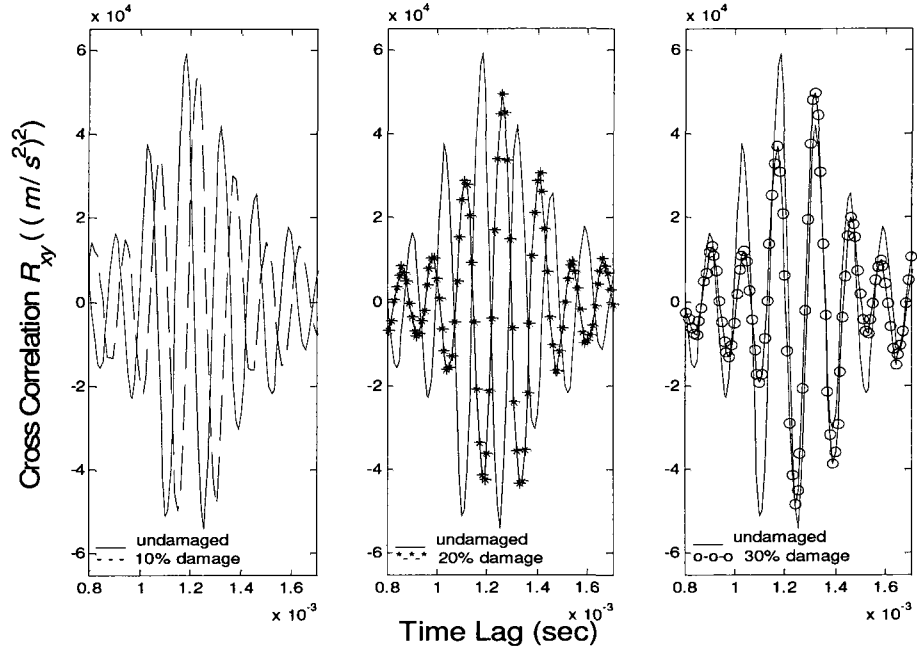


Figure (5.57): Cross-correlation function of acceleration measurements: comparison of the effect of different damage extent on the first peak (damage length 2.5 m)

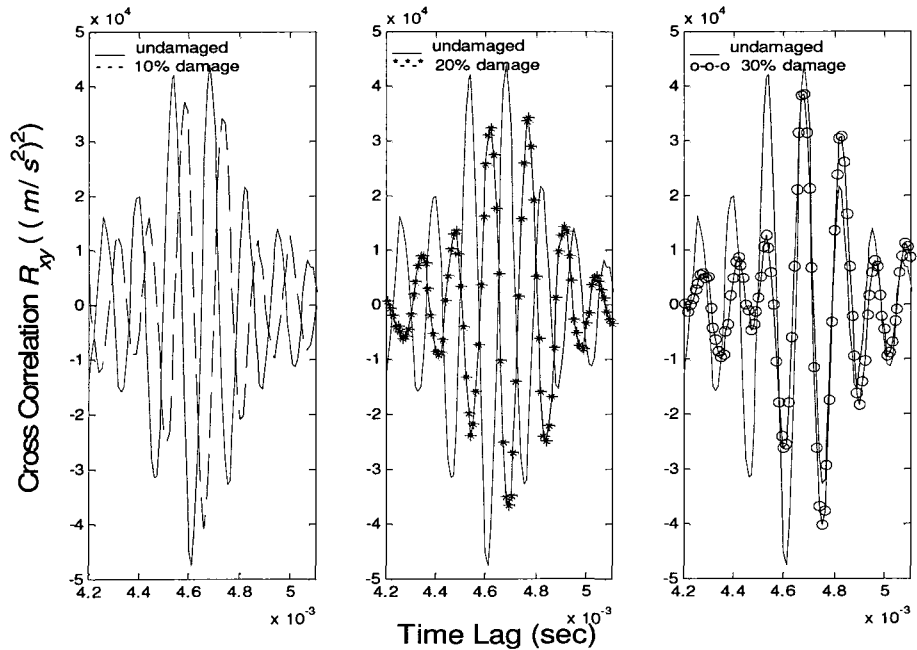


Figure (5.58): Cross-correlation function of acceleration measurements: comparison of the effect of different damage extent on the second peak (damage length 2.5 m)

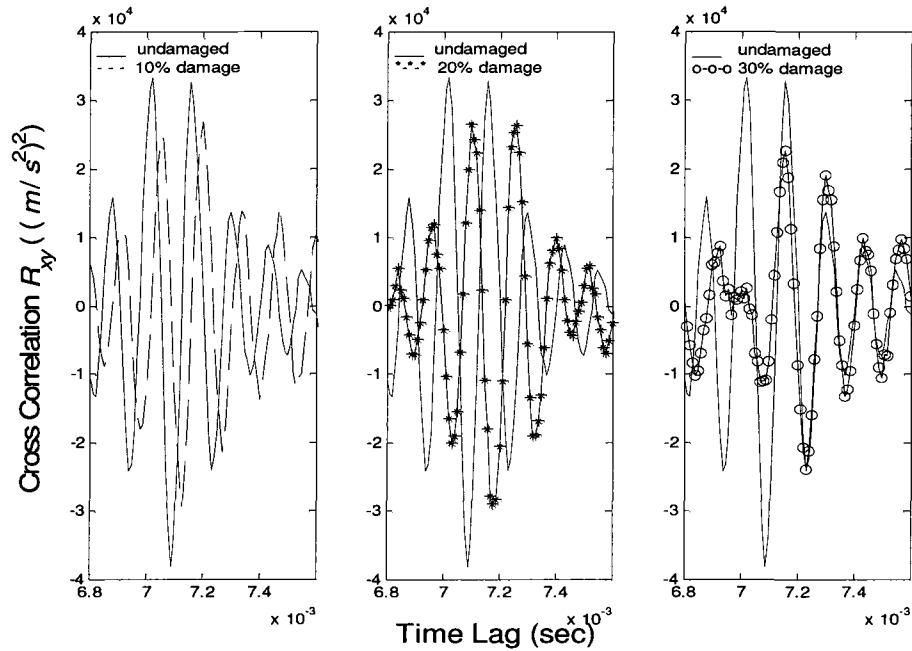


Figure (5.59): Cross-correlation function of acceleration measurements: comparison of the effect of different damage extent on the third peak (damage length 2.5 m)

	Arrival of the incident wave at sensor A	Arrival of the incident wave at sensor B	Arrival of reflected wave at sensor B	
			From left support	From right support
Undamaged	$\frac{0.2}{c} = 0.00006 \text{ s}$	$\frac{4.2}{c} = 0.00124 \text{ s}$	$\frac{24.2}{c} = 0.00716 \text{ s}$	$\frac{15.8}{c} = 0.00468 \text{ s}$
Damaged	$\frac{0.2}{c} = 0.00006 \text{ s}$	$\frac{4.2 - L_d}{c} + \frac{L_d}{(\sqrt{1-s})c}$	$\frac{24.2 - L_d}{c} + \frac{L_d}{(\sqrt{1-s})c}$	$\frac{15.8 - L_d}{c} + \frac{L_d}{(\sqrt{1-s})c}$

Table (5.15): Calculation of time delay in undamaged and damaged rod (damage length 2.5 m)

	Estimated time delay			Calculated time delay	
	1 st case (s=10%)	2 nd case (s=20%)	3 rd case (s=30%)	Known damage length	Unknown damage length
First peak	0.00123 s	0.00126 s	0.00132 s	$\frac{1.5}{c} + \frac{2.5}{(\sqrt{1-s})c}$	$\frac{4}{(\sqrt{1-s})c}$
Second peak	0.00466 s	0.00469 s	0.00475 s	$\frac{13.1}{c} + \frac{2.5}{(\sqrt{1-s})c}$	$\frac{11.6}{c} + \frac{4}{(\sqrt{1-s})c}$
Third peak	0.00713 s	0.00718 s	0.00723 s	$\frac{21.5}{c} + \frac{2.5}{(\sqrt{1-s})c}$	$\frac{20}{c} + \frac{4}{(\sqrt{1-s})c}$

**Table (5.16): Calculated and estimated time delay in damaged rod
(damage length 2.5 m)**

	Damage extent							
	Estimation from first peak		Estimation from second peak		Estimation from third peak		Mean	
	Known damaged length	Unknown damaged length	Known damaged length	Unknown damaged length	Known damaged length	Unknown damaged length	Known damaged length	Unknown damaged length
1 st case (s=10%)	11.4%	7.4%	10.7%	6.9%	6.9%	4.4%	9.7%	6.2%
2 nd case (s=20%)	17%	11.7%	17.1%	11.3%	18.0%	11.8%	17.4%	11.6%
3 rd case (s=30%)	28.7%	19.6%	28.2%	19.2%	27.2%	18.4%	28.0%	19.1%

Table (5.17): Calculation of damage extent in damaged rod (damage length 2.5 m)

Four important conclusions can be drawn from the results presented in Figures (5.57), (5.58), and (5.59):

1. Shifts in all the peaks of cross-correlation function reveals that damage occurs between the sensor locations.
2. As shown by data presented in the tables, for each time delay shift, the new wave speed and thus the extent of damage can be calculated. The final damage extent is considered as the mean of the evaluated values.
3. As the propagation path is shorter than in the previous cases, the estimated damage extents are more reasonable.
4. For better prediction of damage location and damage extent, the propagation path should be restricted to a shorter length as emerged from this analysis. This fact demands the use of more sensors to measure responses at large number of points on the structure.

II. Damage length 1 *m*

In this case, the introduced damage between sensors A and B has 1 *m* length. Cross-correlation function is similar to Figure (5.56) exhibiting three peaks. The effect of the magnitude of damage on the location of these peaks is illustrated in Figures (5.60), (5.61) and (5.62). Tables (5.18), (5.19) and (5.20) show the calculation of damage extent.

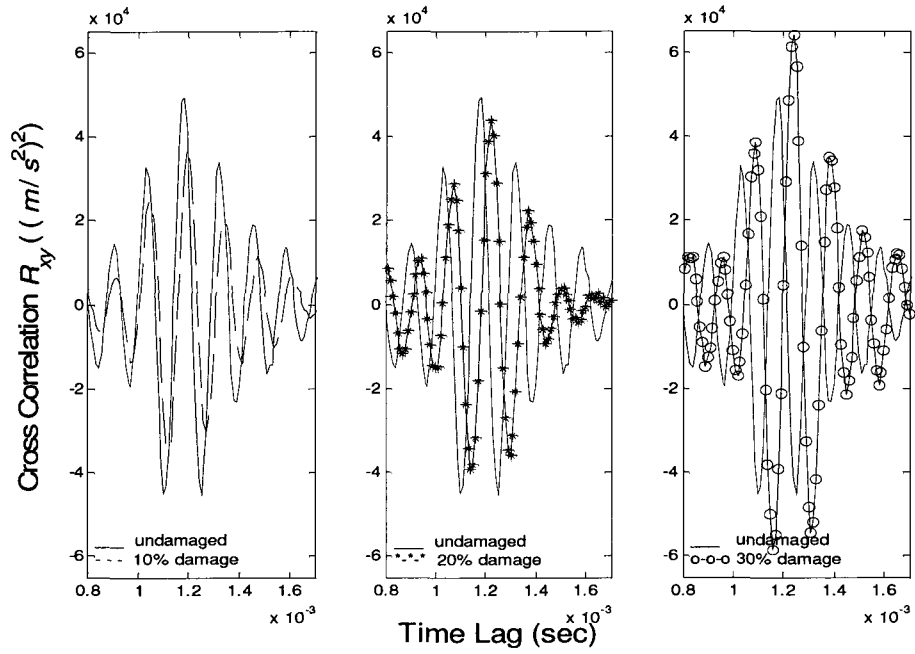


Figure (5.60): Cross-correlation function of acceleration measurements: comparison of the effect of different damage extent on the first peak (damage length 1 m)

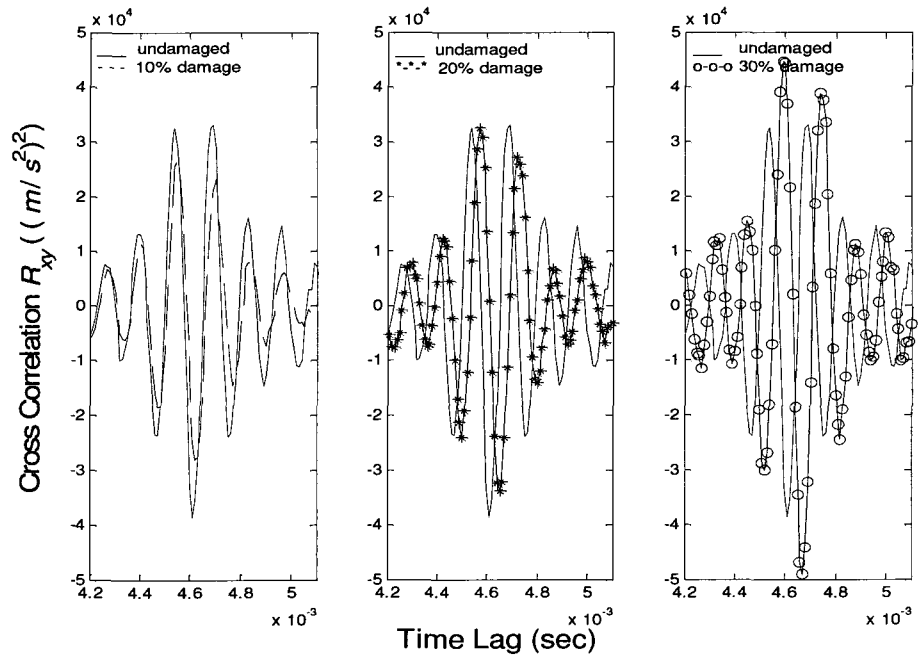


Figure (5.61): Cross-correlation function of acceleration measurements: comparison of the effect of different damage extent on the second peak (damage length 1 m)

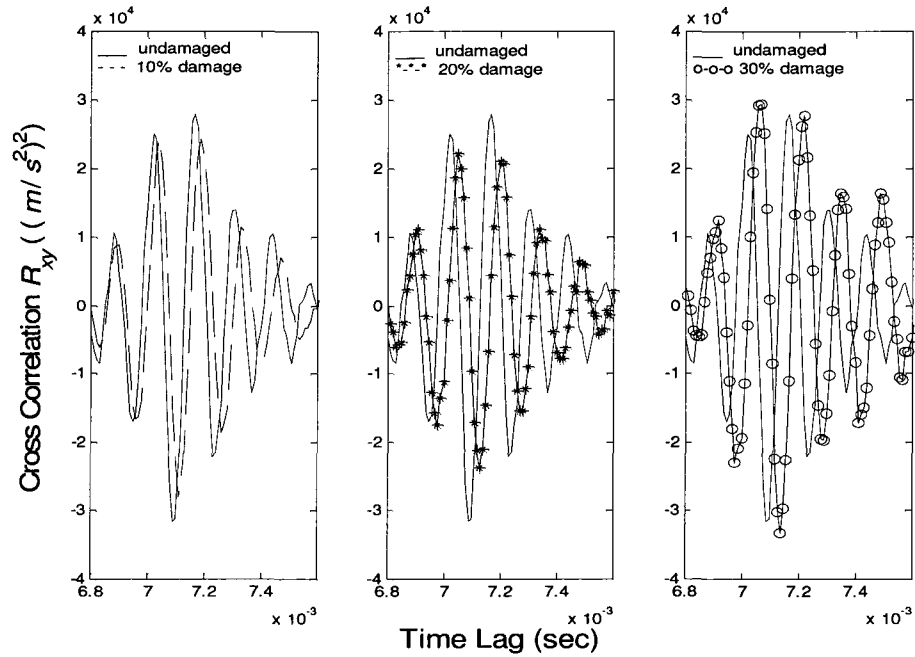


Figure (5.62): Cross-correlation function of acceleration measurements: comparison of the effect of different damage extent on the third peak (damage length 1 m)

	Arrival of the incident wave at sensor A	Arrival of the incident wave at sensor B	Arrival of reflected wave at sensor B	
			From left support	From right support
Undamaged	$\frac{0.2}{c} = 0.00006 \text{ s}$	$\frac{4.2}{c} = 0.00124 \text{ s}$	$\frac{24.2}{c} = 0.00716 \text{ s}$	$\frac{15.8}{c} = 0.00468 \text{ s}$
Damaged	$\frac{0.2}{c} = 0.00006 \text{ s}$	$\frac{4.2 - L_d}{c} + \frac{L_d}{(\sqrt{1-s})c}$	$\frac{24.2 - L_d}{c} + \frac{L_d}{(\sqrt{1-s})c}$	$\frac{15.8 - L_d}{c} + \frac{L_d}{(\sqrt{1-s})c}$

Table (5.18): Calculation of time delay in undamaged and damaged rod (damage length 1 m)

	Estimated time delay			Calculated time delay	
	1 st case (s=10%)	2 nd case (s=20%)	3 rd case (s=30%)	Known damage length	Unknown damage length
First peak	0.00119 s	0.00122 s	0.00124 s	$\frac{3}{c} + \frac{1}{(\sqrt{1-s})c}$	$\frac{4}{(\sqrt{1-s})c}$
Second peak	0.00462 s	0.00465 s	0.00467 s	$\frac{14.6}{c} + \frac{1}{(\sqrt{1-s})c}$	$\frac{11.6}{c} + \frac{4}{(\sqrt{1-s})c}$
Third peak	0.00711 s	0.00713 s	0.00714 s	$\frac{23}{c} + \frac{1}{(\sqrt{1-s})c}$	$\frac{20}{c} + \frac{4}{(\sqrt{1-s})c}$

Table (5.19): Calculated and estimated time delay in damaged rod (damage length 1 m)

	Damage extent							
	Estimation from first peak		Estimation from second peak		Estimation from third peak		Mean	
	Known damaged length	Unknown damaged length	Known damaged length	Unknown damaged length	Known damaged length	Unknown damaged length	Known damaged length	Unknown damaged length
1 st case (s=10%)	4.0%	1.0%	2.0%	1.0%	4.6%	1.2%	3.5%	1.1%
2 nd case (s=20%)	20.6%	5.8%	19.1%	5.4%	16.0%	4.4%	18.6%	5.2%
3 rd case (s=30%)	29.4%	8.9%	28.1%	8.4%	21.0%	6.0%	26.2%	7.8%

Table (5.20): Calculation of damage extent in damaged rod (damage length 1 m)

5.4.4 Conclusions

Based on the analysis carried out in the last three sections, the following general conclusion can be drawn

1. The presented structural health monitoring approach is not model based, that is there is no need to construct a mathematical model for the structure. In the examples presented here, the FEM model is used to produce the simulated measurements. In real life cases the measurements would be obtained through instrumentation of the structure.
2. This approach is entirely based on the measurements of structural response.
3. Implementation of this approach does not need any information about the source or the nature of force. In other words it can deal with narrow-band and broad-band random forces as well as transient forces.
4. This approach is based on the determination of a local parameter of the structure, namely the wave speed, while conventional modal analysis based approaches rely on the global parameters such as natural frequencies or mode shapes.
5. In comparison to other methods of structural health monitoring, the approach presented here is less sensitive to the effect of measurement noises. Such noises in measurements taken at different locations of the structure are expected to be uncorrelated. As illustrated through examples presented in this chapter, even in the presence of 30% noise the changes in dynamical properties are identified with reasonable accuracy.

6. Computational simplicity is one of the important features of this approach when viewed in the context of structural health monitoring.
7. Even with two measurement sensors, an initial prediction of location of damage is possible as illustrated here through examples.
8. Using this approach, an average value of the damage extent can be estimated.

Some of the limitations of this approach are as follows

1. This approach suffers from the assumption of linearity.
2. Detailed information on the location and extent of damage can be obtained only when measurements are made at sufficient number of closely spaced locations.
3. In its present form the method would not work when there are multiple travel paths surrounding the damaged area.
4. The type of noise considered in the current investigation is measurement noise. Such noise in the measurement samples taken from different locations is expected to be uncorrelated. In real life problems another type of noise namely model noise may exist. Examples of such noise are physical changes caused by temperature variations and mass accumulations. The analysis carried out in this thesis does not take into account this type of noise.
5. If the damage is very local such as for example due to a crack in the rod, the estimated damage extent shows the severity of damage smeared over the entire length between measurement locations or the measurement location and boundaries.

Chapter 6

Numerical Illustration:

Dispersive Wave Propagation

6.1 Introduction

In the first part of this chapter, an FEM model is developed to study dispersive wave propagation for bending waves in a beam. This model is validated by an analytical solution. Next cross-correlation analysis is used to estimate time delay of bending wave propagation. Effects of different types of loading, length of propagation path, reflection from the boundaries, and presence of measurement noise are discussed in more detail. Last part of this chapter is devoted to structural health monitoring of dispersive waveguides. Case studies on the estimation of damage location and damage extent are presented.

6.2 Model Validation

In this part, an analytical model is developed for a uniform beam. The analytical solution for the model is considered as a benchmark for the validation of FEM model as presented next.

6.2.1 Analytical Model

I. Problem Description

In Figure (6.1), the infinite beam with modulus of elasticity E , uniform cross-sectional area A , and moment of inertia I is subjected to a force history $P(t)$ at the center, $x = 0$. The material used in this model is concrete with properties shown in Table (6.1). The area and moment of inertia chosen for the model are $A = 0.04 \text{ m}^2$ and $I = 133.3 \times 10^{-6} \text{ m}^4$. Table (6.2) shows the material properties per unit length.

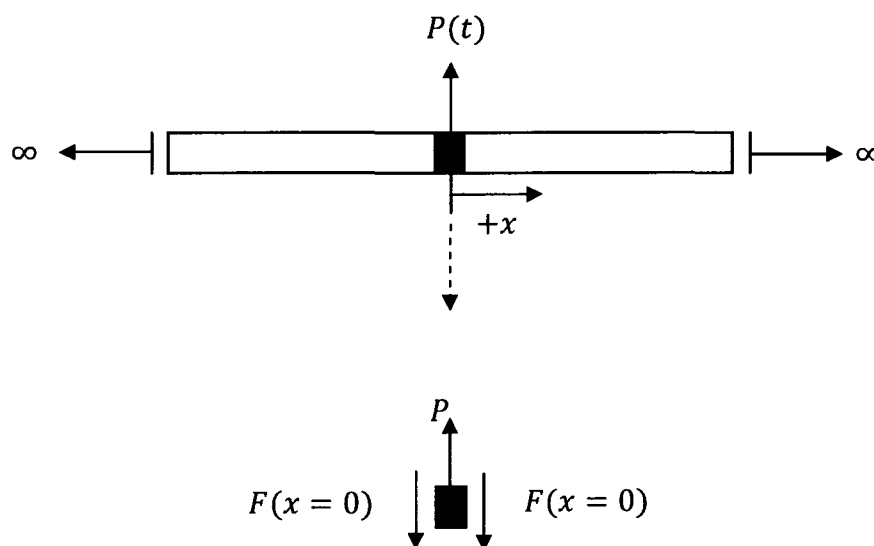


Figure (6.1): Analytical model: infinite beam impacted at center

Material Property	Value
Elasticity Modulus (E)	27.4 GN/m ²
Mass Density	2400 kg/m ³
Viscous Damping Density	178000 N.s/m ⁴

Table (6.1): Material properties of the beam model

Material Property	Value
Mass per Unit Length (\bar{m})	96 kg/m
Viscous Damping per Unit Length (\bar{c})	7000 N.s/m ²

Table (6.2): Material properties of beam model per unit length

Using Equations (4.26) and (4.27), the group and phase speeds are determined as

$$c_p \cong \sqrt{\omega} \left[\frac{EI}{\bar{m}} \right]^{1/4} = 13.966\sqrt{\omega} \quad (6.1)$$

$$c_g \cong 2\sqrt{\omega} \left[\frac{EI}{\bar{m}} \right]^{1/4} = 27.932\sqrt{\omega} \quad (6.2)$$

The force used in this analysis is a triangular impulsive force. Time history and Fourier spectrum of the force are plotted in Figures (6.2) and (6.3), respectively. The Fourier spectrum of the force is obtained using a time step of 0.00001 s and a period of 0.01 s . This time step results in a Nyquist frequency of 50 kHz that completely contains the frequency content of the force.

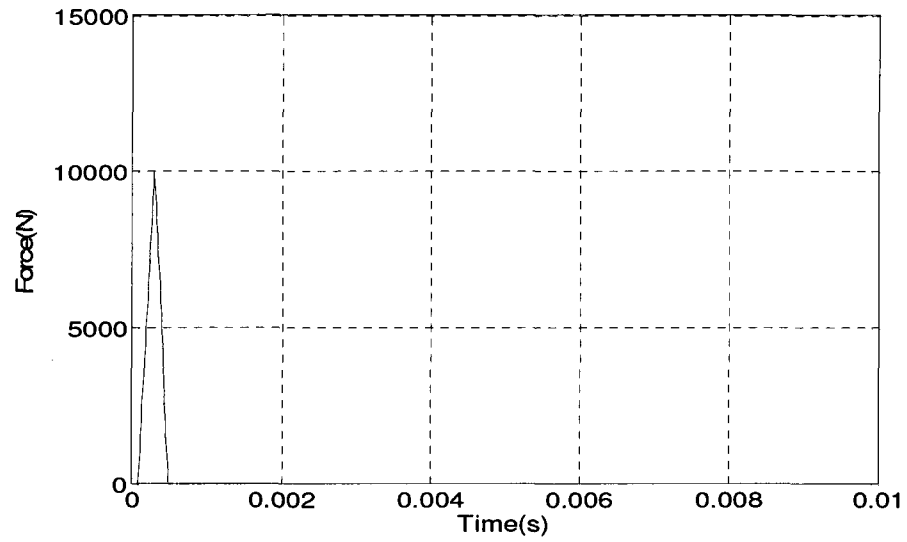


Figure (6.2): Triangular impulsive force applied at the center of infinite beam

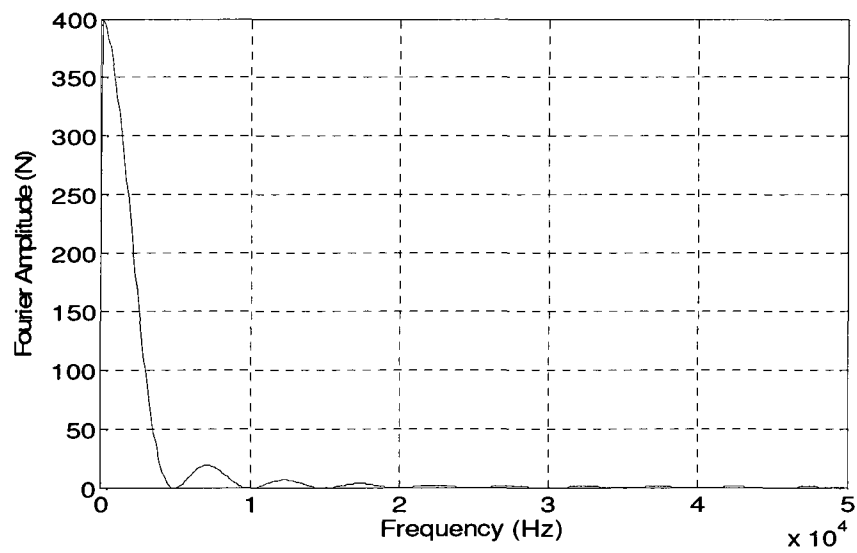


Figure (6.3): Fourier spectrum of impulsive force

II. Analytical Solution

The general solution of the equation of motion of beam, presented in Section 4.3.1, is given by

$$\begin{aligned}
 u(x, t) = & \sum A e^{-i(kx - \omega t)} + \sum B e^{-(kx - \omega t)} \\
 & + \sum C e^{+i(kx + \omega t)} + \sum D e^{+(kx + \omega t)}
 \end{aligned} \tag{6.3}$$

For positive ($x > 0$) propagating wave, one obtains

$$u(x, t) = \sum A e^{-i(kx - \omega t)} + \sum B e^{-(kx - \omega t)} \tag{6.4}$$

Coefficients A and B are selected so as to satisfy the boundary conditions. To enforce the boundary conditions, an infinitesimal element at the impact location ($x = 0$) is considered. The Free Body Diagram of this element is depicted in Figure (6.1). On account of the symmetry of the beam (Doyle, 1997):

1. There is no rotation at this point.
2. The two internal shear forces, which act on the element, are equal.

Hence, one obtains

$$1) \frac{\partial u(x = 0, t)}{\partial x} = 0 \tag{6.5}$$

and

$$\text{II) } 2F = 2EI \frac{\partial^3 u(x=0, t)}{\partial x^3} = P(t) \quad (6.6)$$

The spectral form of these boundary conditions are expressed as

$$\text{I) } \frac{\partial \hat{u}}{\partial x} = 0 \quad (6.7)$$

and

$$\text{II) } 2\hat{F} = 2EI \frac{d^3 \hat{u}(x=0)}{dx^3} = \hat{P} \quad (6.8)$$

Substituting of Equation (6.4) in Equation (6.5) and setting $x = 0$, one obtains

$$-ikA - kB = 0 \quad (6.9)$$

or

$$B = -iA \quad (6.10)$$

The solution thus becomes

$$u(x, t) = \sum A \left(e^{-ikx} - ie^{-kx} \right) e^{i\omega t} \quad (6.11)$$

In order to find the coefficient A , the second boundary condition stated in Equation (6.8) is used

$$2EIA \left(2ik^3 \right) = \hat{P} \quad (6.12)$$

or

$$A = \frac{\hat{P}}{4EIk^3} \quad (6.13)$$

Thus the complete analytical solution is

$$u(x, t) = \sum \frac{-i\hat{P}}{4EIk^3} \left(e^{-ikx} - ie^{-kx} \right) e^{i\omega t} \quad (6.14)$$

On the basis of Equation (6.14), the frequency response function of force and displacement is given by

$$H_{f-d}(x, \omega) = \frac{-i}{4EIk^3} \left(e^{-ikx} - ie^{-kx} \right) \quad (6.15)$$

III. Analytical Results

The numerical solution of Equation (6.14) is obtained using the procedure described in Section 4.4.1., Figure (6.4) shows this solution. Some of the interesting features that can be observed from this figure are

1. The wave packet disperses as it travels. The dispersion effect results in distortion of the wave packet.
2. Dispersion effect occurs because each frequency component travels with its own speed. In other words, the wave speed depends on the frequency.

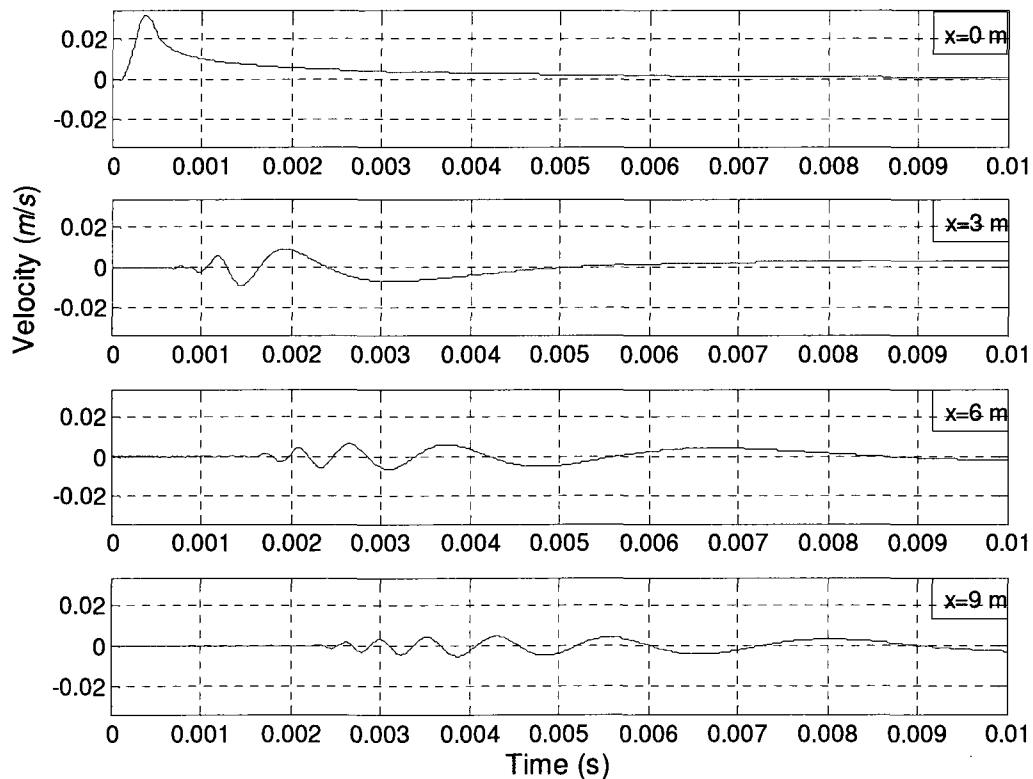


Figure (6.4): Velocity response of infinite beam impacted at the center

6.2.2 FEM Model

I. Problem Description

Figure (6.5) shows a finite beam with modulus of elasticity E , uniform cross-sectional area A and moment of inertia I . It is subjected to a force history $P(t)$ at the center, $x = 0$. Different types of end conditions are enforced with translational and rotational springs. The solutions are obtained for different values of stiffness of spring. The cases modeled are:

1. Beam with fixed-fixed boundary condition.
2. Simply supported beam.

The material and geometric properties of the beam are similar to properties of beam in section 6.2.1. The length of the beam is 20 m.

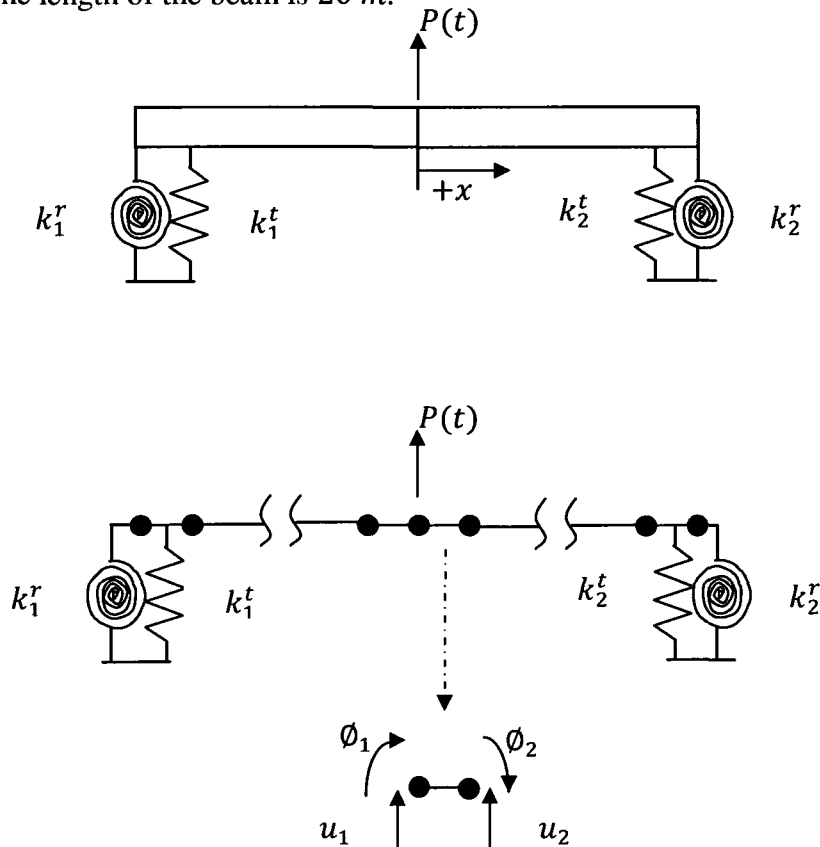


Figure (6.5): FEM model: finite beam impacted at center

II. FEM Mesh

The properties of the FEM mesh modeled in this study are presented in Table (6.3)

Properties	Value
Length of the Beam	20 m
Length of Elements	5 cm
Number of Elements	400
Number of Degrees of Freedom	802

Table (6.3): FEM mesh properties

In order to examine the ability of the FEM mesh for capturing the wave characteristics, the following analysis is carried out.

Suppose that the wavelength of the response is represented by n finite elements, namely $\lambda = ne_l$. Then the wavenumber can be obtained as

$$k = \frac{2\pi}{ne_l} \quad (6.16)$$

Using the undamped spectrum relation expressed in Equation (4.25) one obtains

$$\sqrt{\omega} \left(\frac{\bar{m}}{EI} \right)^{1/4} = \frac{2\pi}{ne_l} \quad (6.17)$$

thus

$$n = \frac{\sqrt{2\pi}}{e_l \sqrt{f}} \left(\frac{EI}{\bar{m}} \right)^{1/4} \quad (6.18)$$

Assuming the maximum frequency that should be captured is 17 kHz, substitution of the numerical values given in Tables (6.1) and (6.2) in Equation (6.18) results in

$$n = 5.4 \quad (6.19)$$

This result shows that the wavelength corresponding to the maximum frequency that should be captured is represented by more than five finite elements. This reveals that the FEM mesh approximates the continuous model quite accurately.

III. FEM results

In this section, two FEM model are considered:

1. Beam with fixed-fixed supports
2. Simply supported beam

The solutions are obtained using the average acceleration method described in Section 4.4.2. Figure (6.6) and Figure (6.7) show the velocity response of impacted beam with fixed-fixed supports and the simply supported beam respectively. These figures also show comparison with the response of infinite beam described in the previous section.

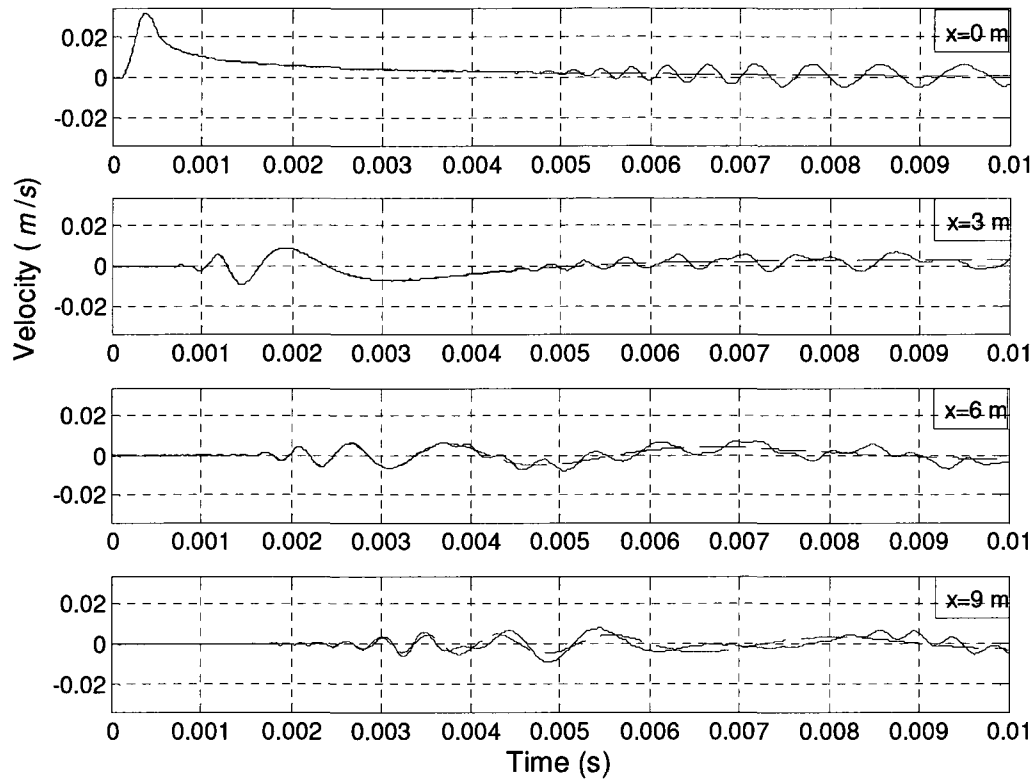


Figure (6.6): Velocity response of impacted beam:

— beam with fixed-fixed boundary - - - infinite beam

Some interesting observations that can be made on the basis of Figure (6.6) and Figure (6.7) are

1. The time at which the solutions of infinite model and FEM model diverge is the time at which the reflected wave has reached the measurement location.
2. Because of different boundary conditions, different types of reflected waves appear.

3. The reflected wave from a pinned supports, is inverted waveform of the incident waves. Due to dispersion effect, this property is not clear in the figure but it can be proved analytically.

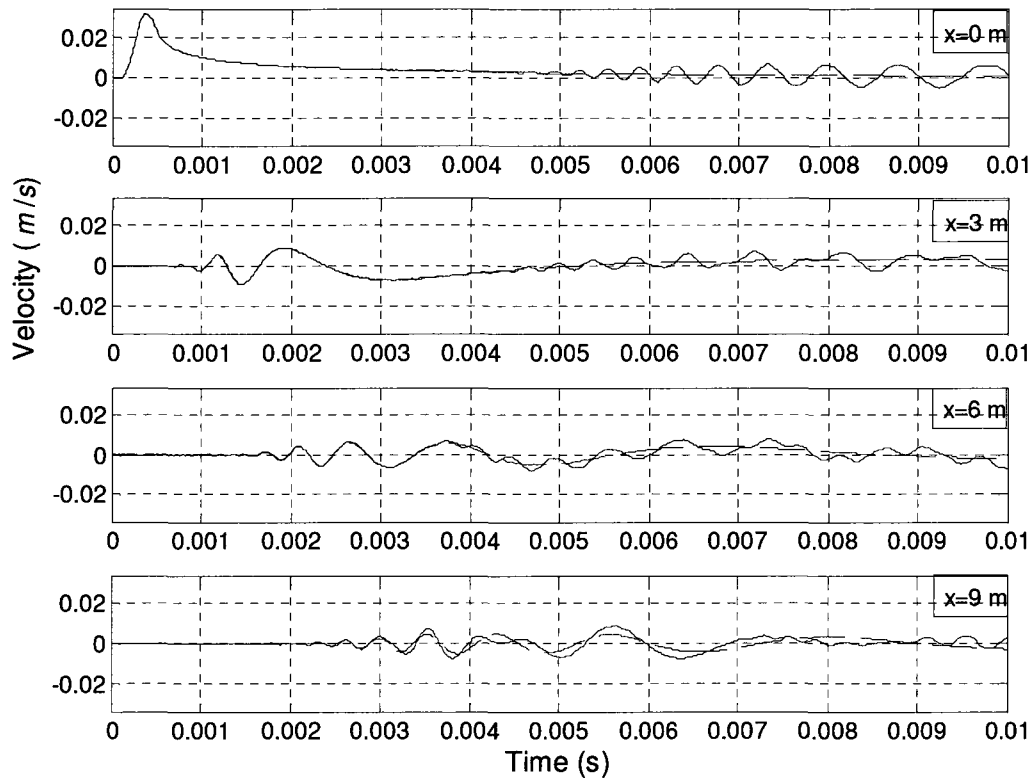


Figure (6.7): Velocity response of impacted beam:

___ simply supported beam _ _ _ _ infinite beam

6.3 Time Delay Estimation

In this part of Chapter 6, cross-correlation analysis is used for the estimation of time delay in a beam, which is a dispersive waveguide. This part is presented in four sections:

1. Effect of loading
2. Effect of propagation length
3. Effect of reflection
4. Effect of noise

6.3.1 Effect of Loading

Figure (6.8) sketches the model used in this analysis.

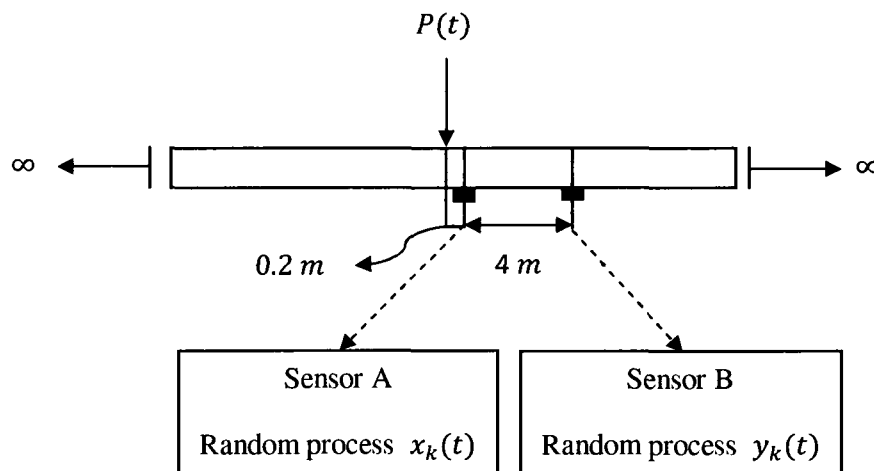


Figure (6.8): Beam model for time delay estimation problem: investigation of the effect of different types of loading

As shown in Figure (6.8), two sensors located 4 m apart measure the velocity and acceleration response of the beam. Using Equation (6.2), the time delay between the measurements at sensors A and B is given by

$$t = \frac{d}{c_g} = 0.1432\omega^{-1/2} \quad (6.20)$$

In this section three different force histories are considered, namely

- I. Narrow-band force
- II. Broad-band force
- III. Transient force

I. Narrow-band force

The narrow-band force used in this analysis is a white random process with the central frequency $\omega_0 = 2\pi \times 6000 \text{ rad/s}$ and bandwidth $B = 2\pi \times 4000 \text{ rad/s}$. Using Equation (6.2), for this central frequency the time delay works out to

$$t = 0.0074 \text{ s} \quad (6.21)$$

Figure (6.9) shows a sample of narrow-band force history. Figure (6.10) presents the corresponding autospectral density function of the narrow-band force.

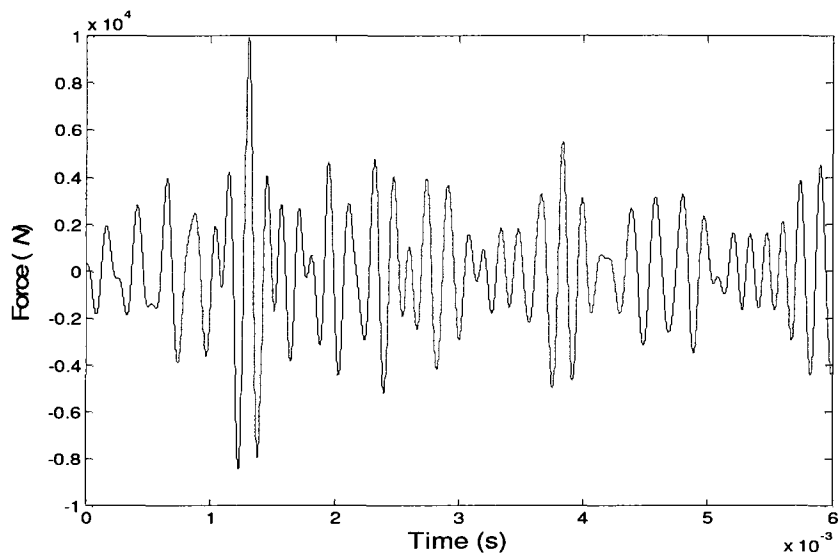


Figure (6.9): A sample of the narrow-band force history

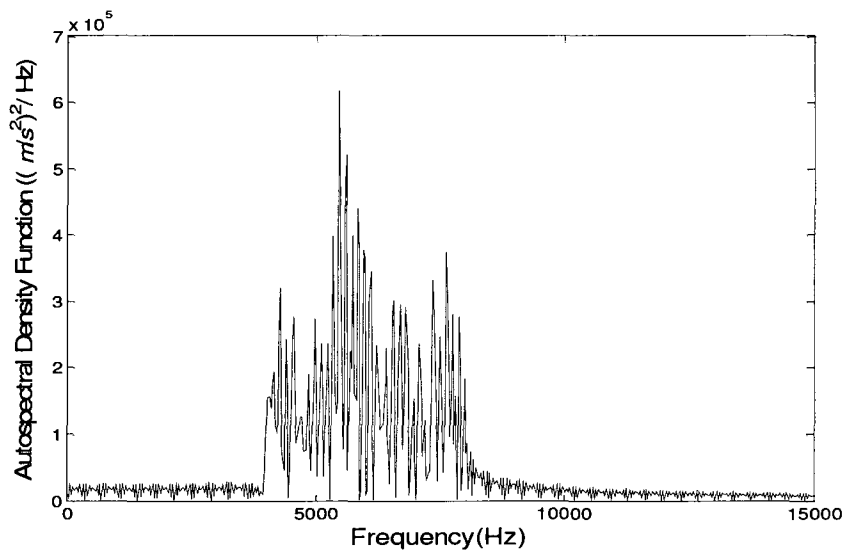


Figure (6.10): Aut spectral density function of narrow-band force

The acceleration responses measured at sensors A and B are plotted in Figure (6.11). It is assumed that there is no noise in these measurements. The arrival time of highest frequency at sensor B can be readily detected. Such detection is not generally practical due to the presence of noise.

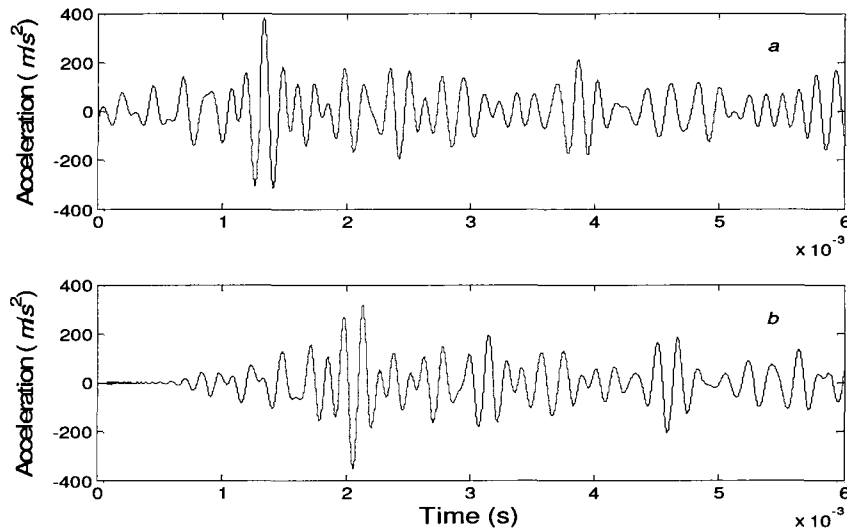


Figure (6.11): Acceleration response a) at sensor A b) at sensor

Figure (6.12) shows the autospectral density functions of the acceleration responses at sensors A and B. It may be noted that the spectra of these measurements spans the same frequency band of force. Cross-correlation coefficient of the acceleration and velocity measurements are plotted in Figure (6.13) and Figure (6.14) respectively. These figures reveal some interesting features that are worth mentioning here:

1. The time delay detected by measurements exactly coincides with the exact solution of Equation (3.54).

2. As explained in Section 3.3 the time delay between two measurements along a dispersive path coincides with the peak of cross-correlation envelope.
3. Velocity response shows better coincidence with the exact solution of cross-correlation coefficient.

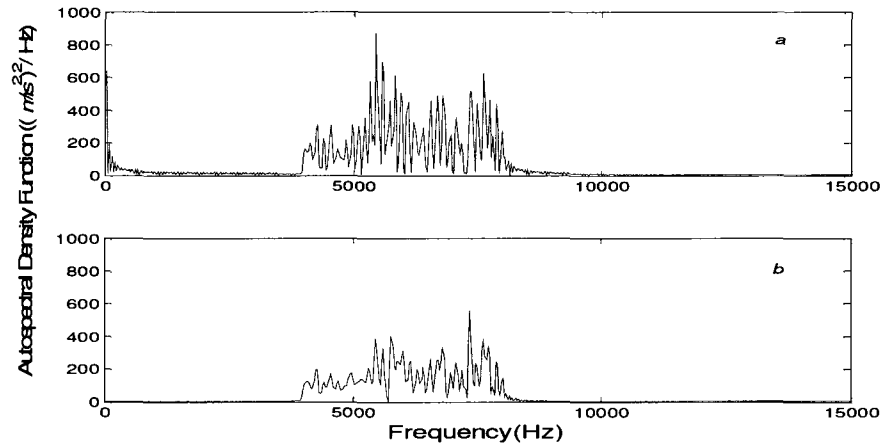


Figure (6.12): Autospectral density function of acceleration responses

a) at sensor A b) at sensor B

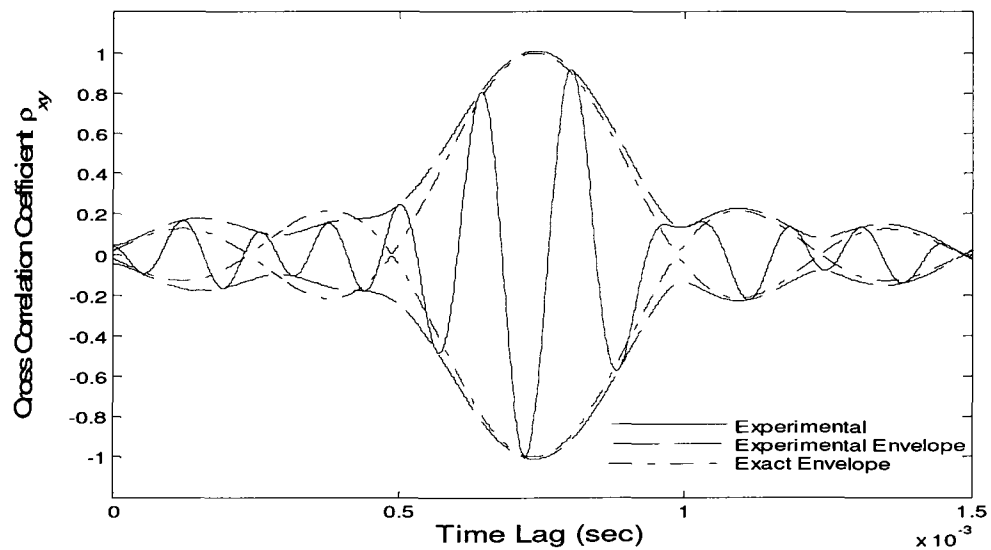


Figure (6.13): Cross-correlation coefficient of acceleration response to narrow-band force

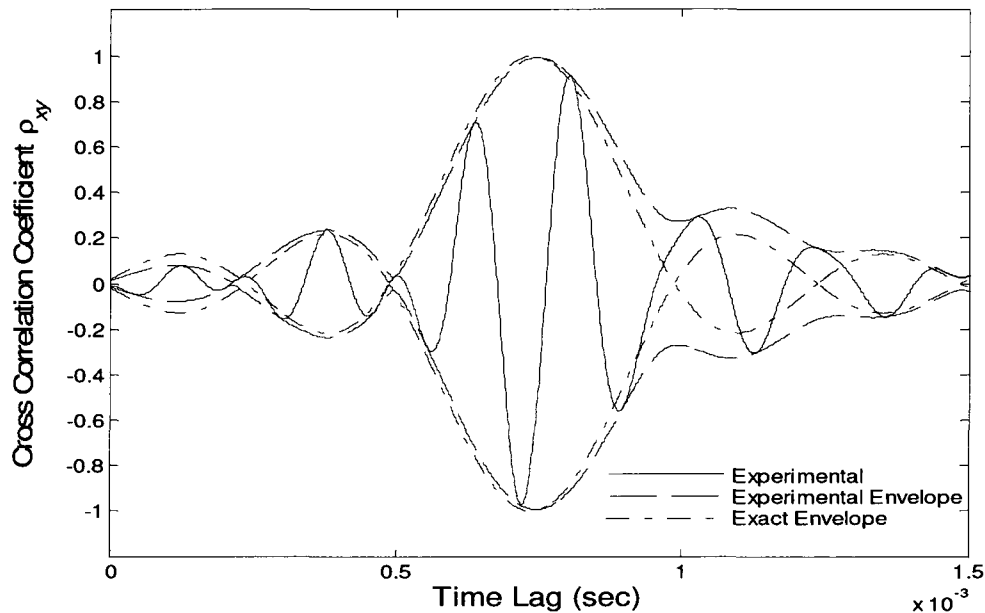


Figure (6.14): Cross-correlation coefficient of velocity response to narrow-band force

In order to have a distinct peak in the cross-correlation coefficient, the waves should have acceptable bandwidth. Two conflicting points arise here:

1. To avoid the dispersion effect, the waves should have narrow-band.
2. As the bandwidth of wave becomes narrower, the wave tends to become a monocomponent wave. For a monocomponent wave, cross-correlation coefficient is a sinusoid. Hence no distinct peak can be detected.

In order to resolve this difficulty, a compromise between these two properties should be achieved. As shown in Figure (6.13), an octave bandwidth is an acceptable bandwidth (White, 1969). It is also interesting to investigate the cross-correlation coefficients for broader and narrower bandwidth responses. Broader bandwidth is investigated in the next section. The cross-correlation coefficient for a narrower bandwidth, namely one third of

an octave, but with the same central frequency, is shown in Figure (6.15). It may be noted that for a bandwidth equal to one third of an octave, the cross-correlation coefficient still exhibits distinct peak needed for the time delay detection.

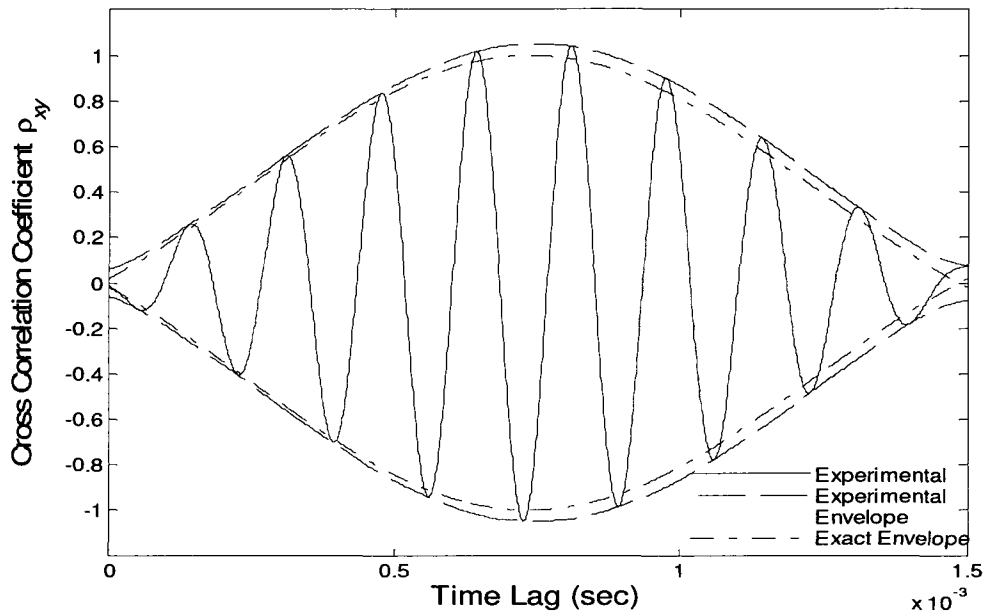


**Figure (6.15): Cross-correlation coefficient of acceleration response to narrow-band force
(with the bandwidth of 1/3 of an octave)**

II. Broad-band force

The broad-band force used in this analysis is a white random process with the central frequency $\omega_0 = 2\pi \times 6000 \text{ rad/s}$ and bandwidth $B = 2\pi \times 12000 \text{ rad/s}$. As evident from Figure (6.16), the cross-correlation coefficient of a broad-band wave packet does not provide meaningful results (White, 1969). Hence, the acceleration responses are filtered using a bandpass filter as explained in Section 3.3. The pass band is an octave, namely $2\pi \times 4000 \text{ rad/s}$ with the central frequency $2\pi \times 6000 \text{ rad/s}$. Figure (6.17)

shows one sample of filtered acceleration responses at sensors A and B while Figure (6.18) displays the autospectral density functions of these responses. The cross-correlation coefficient of filtered response, which is plotted in Figure (6.19), shows accurate estimation of time delay.

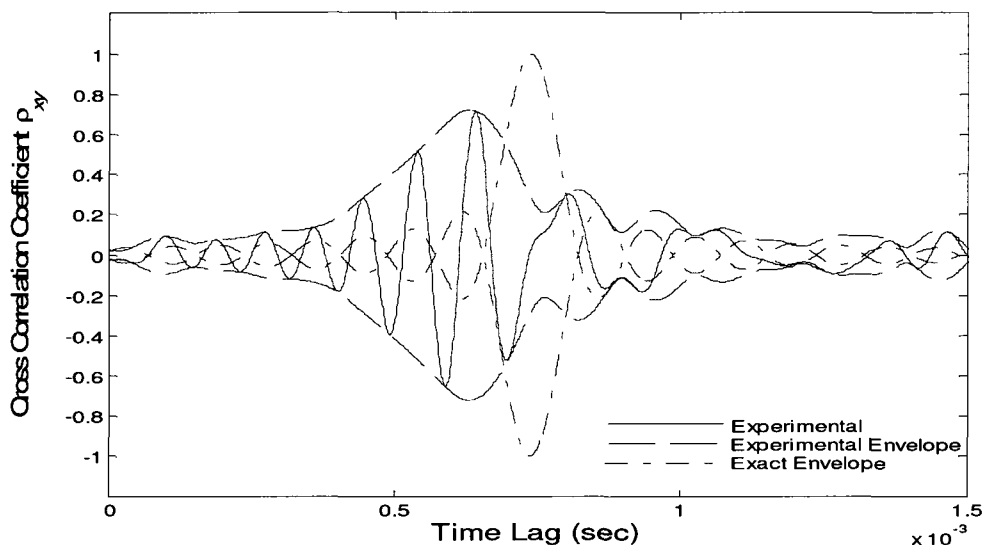
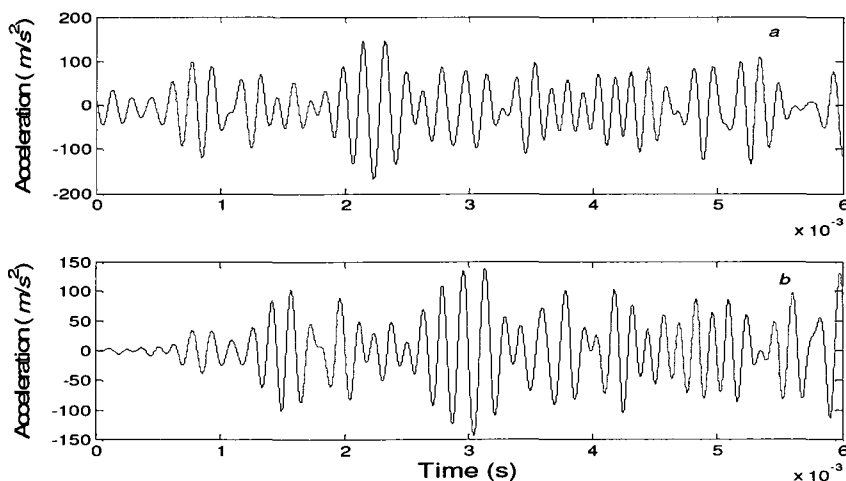


Figure (6.16): Cross-correlation coefficient of acceleration response to broad-band force



**Figure (6.17): A sample of filtered acceleration response a) at sensor A b) at sensor B
(with the pass band of one octave)**

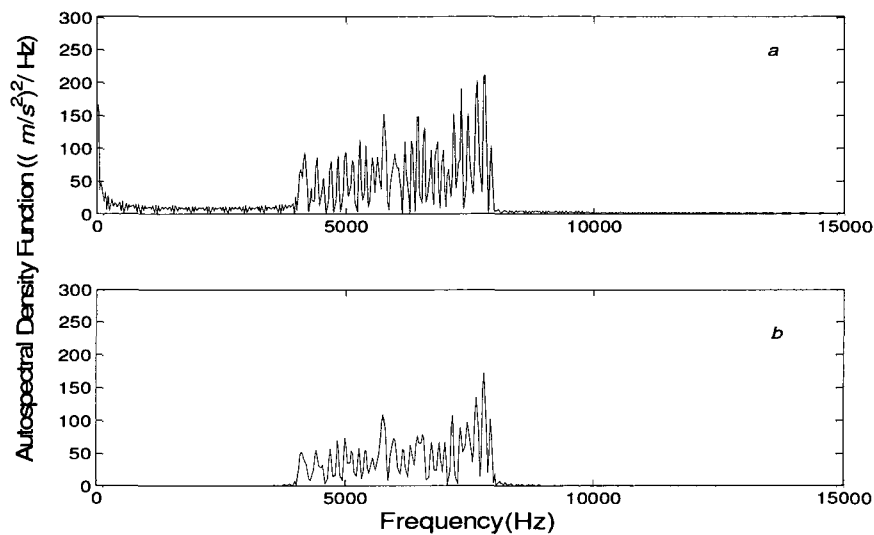


Figure (6.18): Autospectral density function of filtered acceleration response

a) at sensor A b) at sensor B

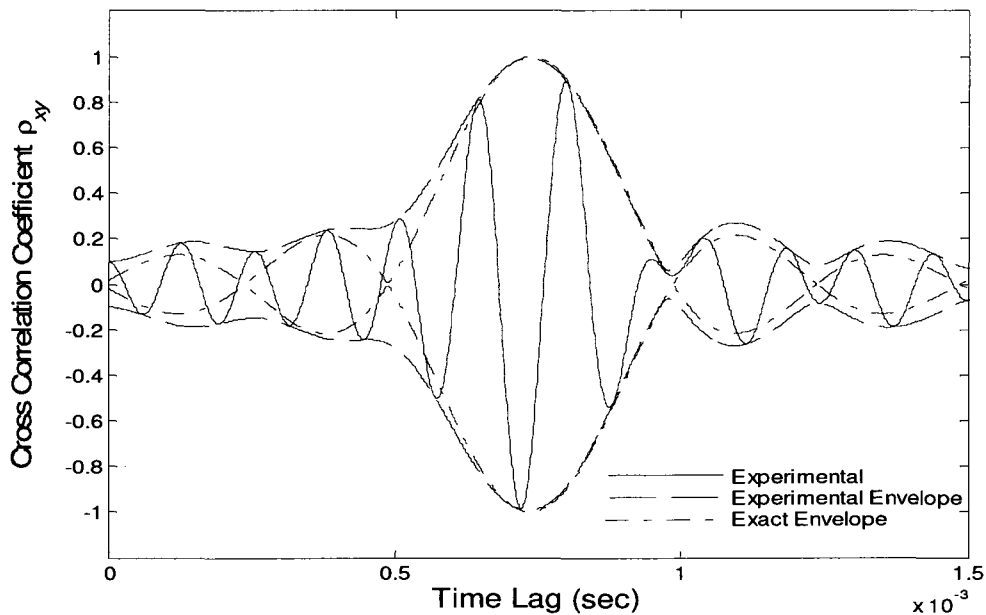


Figure (6.19): Cross-correlation coefficient of filtered acceleration response to

broad-band force

III. Transient force

The transient force used in this analysis is a triangular impulsive force. This transient force and its Fourier spectrum are plotted in Figures (6.20) and (6.21), respectively. It may be noted that the Fourier spectrum of the force spans up to 15 kHz. The dominant energy is contained in the frequency band 0 to 5 kHz. This proves that the transient force has a broad spectrum. Similar to broad-band random force, the acceleration responses are filtered with a frequency band $B = 2\pi \times 4000 \text{ rad/s}$ and central frequency $\omega_0 = 2\pi \times 6000 \text{ rad/s}$. Figure (6.22) shows the resultant filtered acceleration responses and Figure (6.23) presents the Fourier spectrum of these filtered accelerations. Although the Fourier spectrum of the responses are not flat (which is expected for a random force), the peak of correlation coefficient envelope shows the time delay. This fact is illustrated in Figure (6.24).

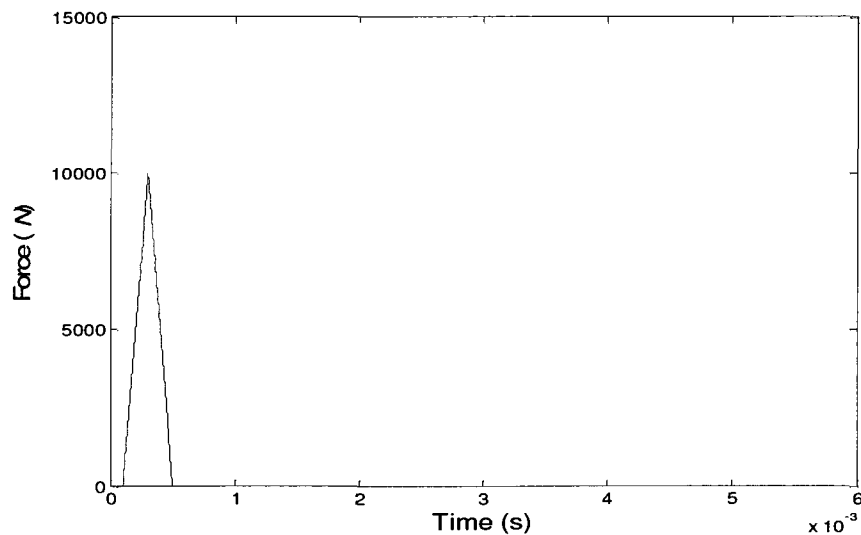


Figure (6.20): Triangular impulsive force

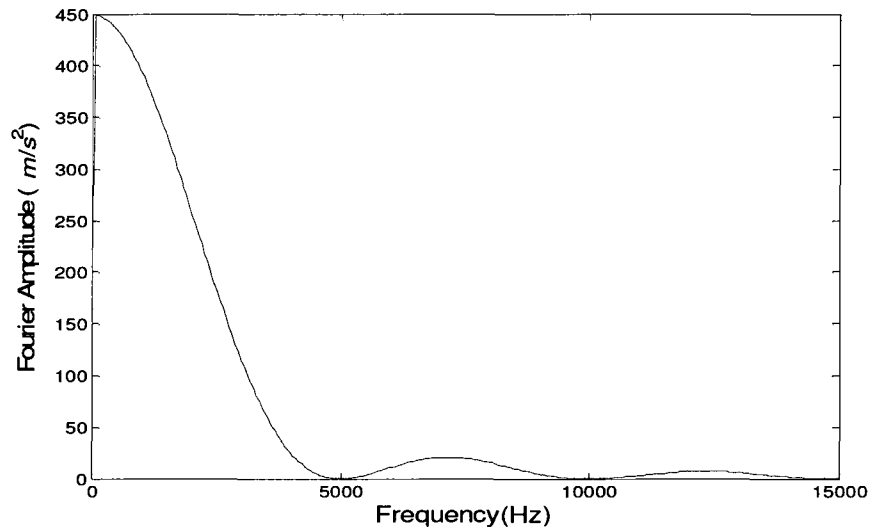
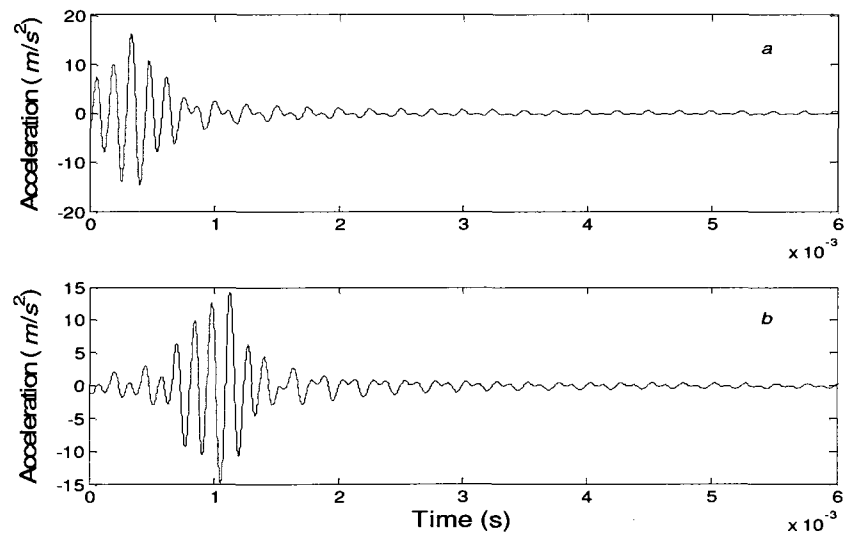


Figure (6.21): Fourier spectrum of the triangular impulsive force



**Figure (6.22): Filtered acceleration response a) at sensor A b) at sensor B
(with the pass band of one octave)**

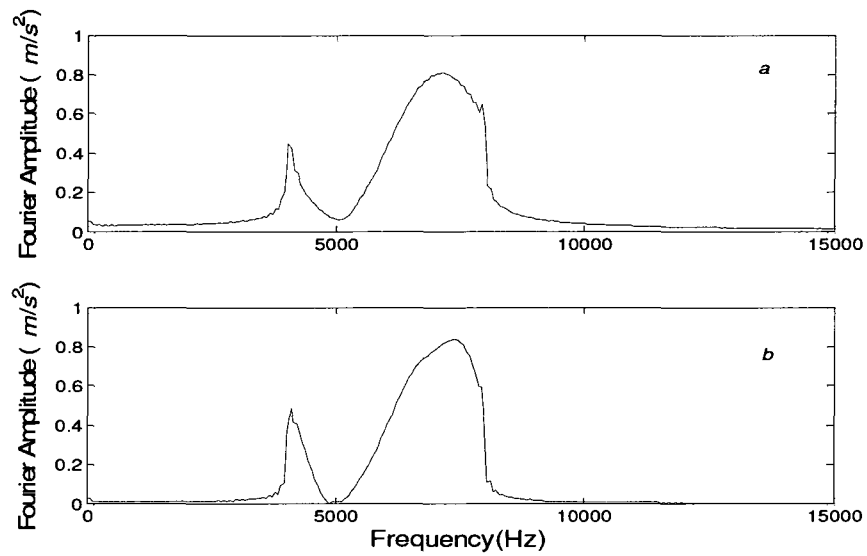


Figure (6.23): Fourier spectrum of filtered acceleration response

a) at sensor A b) at sensor B

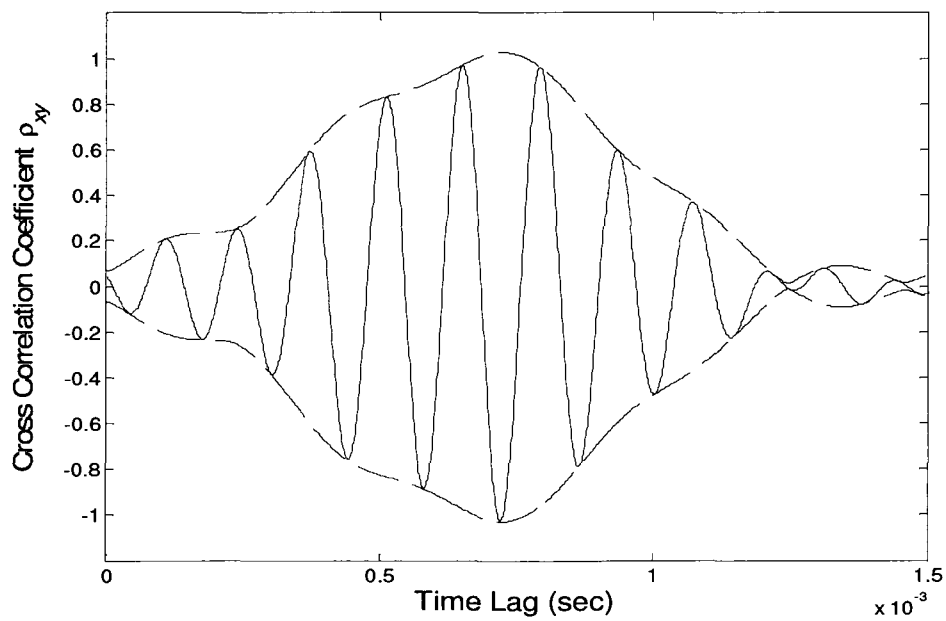


Figure (6.24): Cross-correlation coefficient of filtered acceleration response to transient

force ($B = 2\pi \times 4000 \text{ rad/s}$, $\omega_0 = 2\pi \times 6000 \text{ rad/s}$)

In comparison with the previous cases, the peak of cross-correlation coefficient is less distinct; hence the detection of the peak maybe more difficult. The choice of the pass band of the filter in the main lobe of the Fourier spectrum produces a more identifiable peak. Figure (6.25) shows the cross-correlation coefficient for the case where the bandwidth of the filter is chosen to be $B = 2\pi \times 2000 \text{ rad/s}$ with the central frequency $\omega_0 = 2\pi \times 3000 \text{ rad/s}$. Recalling equation (6.20) the time delay of this band of wave is:

$$t = 0.00104 \text{ sec} \quad (6.22)$$

The location of peak in the cross-correlation coefficient in Figure (6.25) closely corresponds to the value calculated in Equation (6.22).

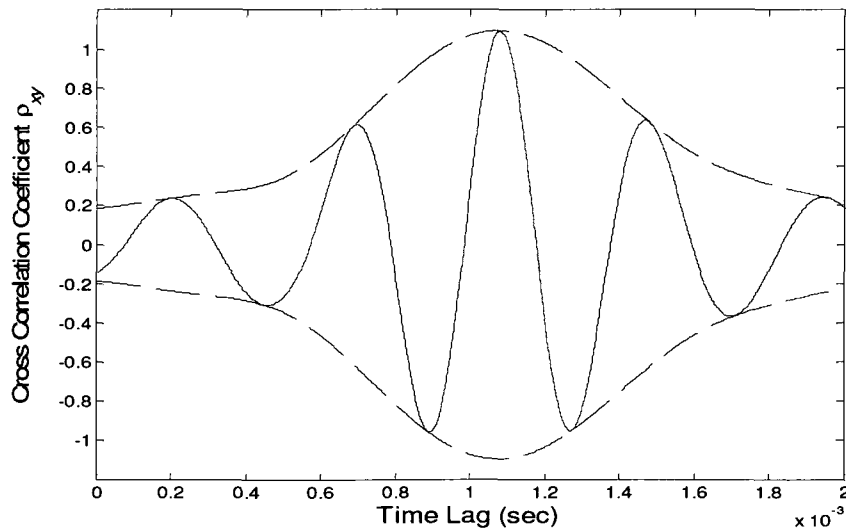


Figure (6.25): Cross-correlation coefficient of filtered acceleration response to transient force ($B = 2\pi \times 2000 \text{ rad/s}$, $\omega_0 = 2\pi \times 3000 \text{ rad/s}$)

6.3.2 Effect of Length of Propagation Path

As the wave propagates through a non-dispersive path, the shape of the waveform remains unchanged. If there is no dissipation in the system, the measurements at any two locations along the propagation path are fully correlated. This property is however not valid for dispersive propagation path. Due to distortion effect in dispersive path, the waveform loses its coherency as it progresses through the path (White, 1969). In this section this property is examined in the model shown in Figure (6.26). In order to investigate how the length of propagation path affects the correlation analysis of a dispersive wave, sensor A is kept fixed and sensor B is situated at different locations. The length of propagation path is denoted by L_p . The force history is a narrow-band white random process with the central frequency $\omega_0 = 2\pi \times 6000 \text{ rad/s}$ and bandwidth $B = 2\pi \times 4000 \text{ rad/s}$. Three different lengths of path are considered: (1) $L_p = 8\text{m}$ (2) $L_p = 16\text{m}$ (3) $L_p = 20\text{m}$. Figures (6.27), (6.28) and (6.29) show the cross-correlation coefficients for these three cases respectively.

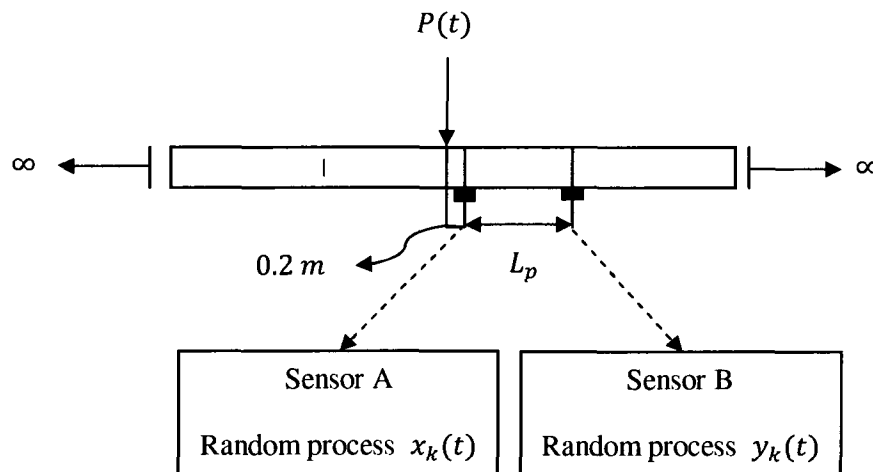


Figure (6.26): Beam model for time delay estimation problem: investigation of the effect of propagation path length

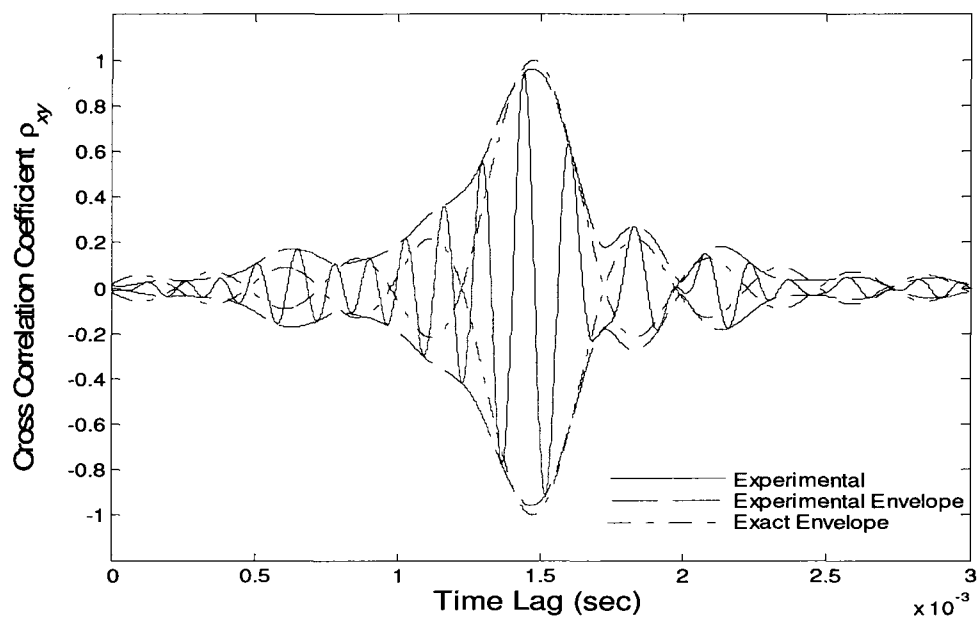


Figure (6.27): Cross-correlation coefficient of acceleration response $L_p = 8$ m

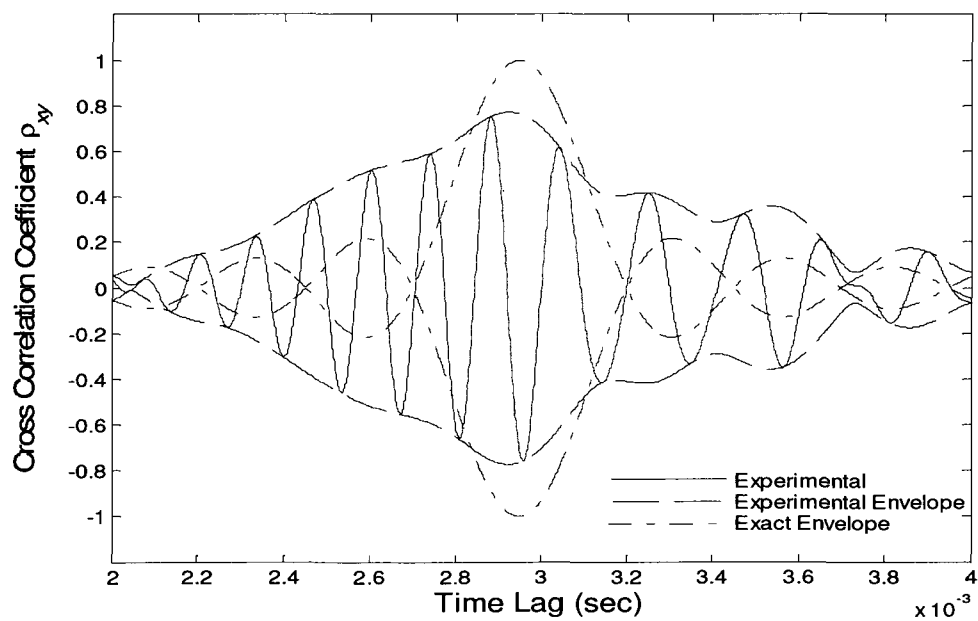


Figure (6.28): Cross-correlation coefficient of acceleration response $L_p = 16$ m

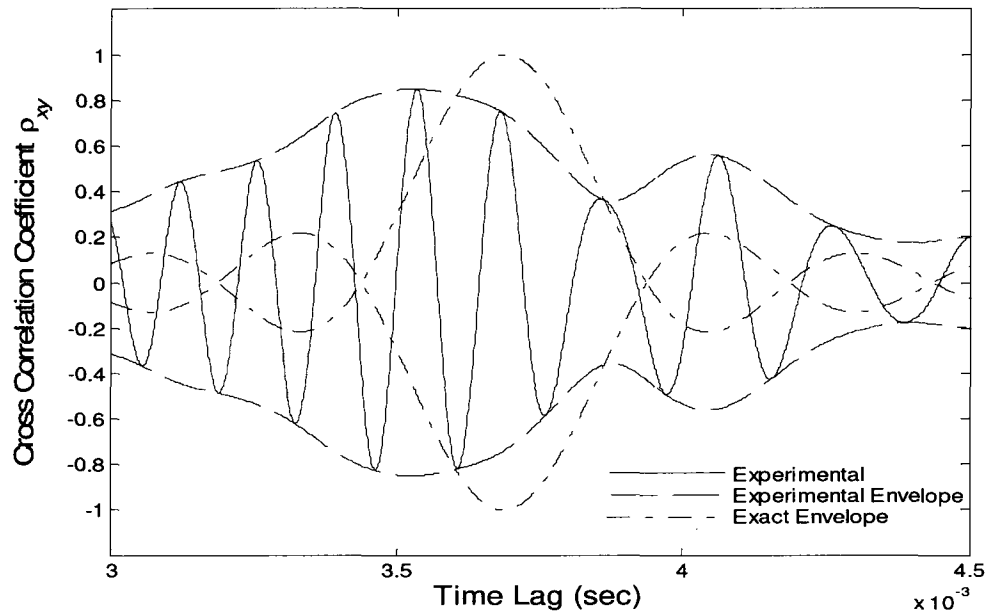


Figure (6.29): Cross-correlation coefficient of acceleration response $L_p = 20$ m

Based on the results of different simulated experiments two conclusions can be drawn:

1. As L_p increases, the accuracy of the detected time delay decreases.
2. As L_p increases, the correlation of two measurements at the time delay (where the peak happens) decreases. This fact happens because the group wave (one octave band of wave) deforms along the propagation path.

6.3.3 Effect of Reflection

In this section the effect of reflected waves (from the boundaries of a simply supported beam) on the cross-correlation analysis is considered. The model chosen for this study is shown in Figure (6.30). As can be mathematically proved, the reflected waves in a simply supported beam are the inverted forms of incident waves. The force history is a narrow-band white random process with the central frequency $\omega_0 = 2\pi \times 6000 \text{ rad/s}$ and bandwidth $B = 2\pi \times 4000 \text{ rad/s}$.

When the load is applied, two incident waves are created: the forward wave ($+x$) and backward wave ($-x$). The forward wave passes through ab , is reflected from boundary at e in an inverted form, and again travels through ba . The backward wave travels from f to d , is reflected in an inverted shape, then it passes through ab and reaches the other end of the beam. Table (6.4) shows the calculation of the times at which the incident and reflected waves arrive at the two sensors

	Arrival of incident wave	Arrival of reflected wave	
		From left support	From right support
Sensor A	$fa/c = 0.00004 \text{ s}$	$(fd+da)/c = 0.00372 \text{ s}$	$(fe+ea)/c = 0.00366 \text{ s}$
Sensor B	$fb/c = 0.0078 \text{ s}$	$(fd+db)/c = 0.00446 \text{ s}$	$(fe+eb)/c = 0.00291 \text{ s}$

Table (6.4): Arrival time of incident and reflected waves in a simply supported beam

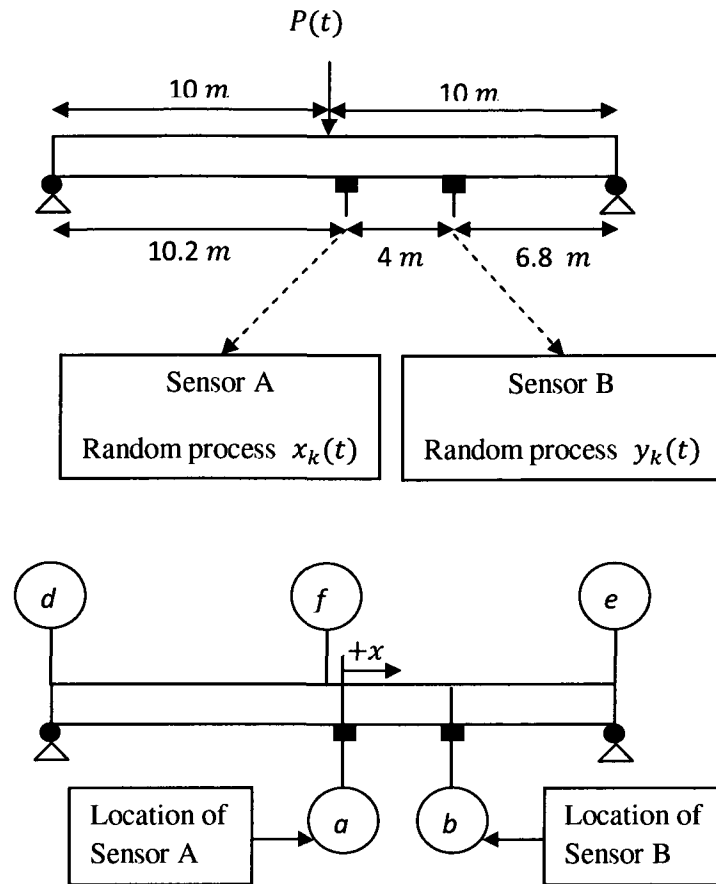


Figure (6.30): Beam model for time delay estimation problem: investigation of the effect of reflection from boundaries

Analogous to the non-dispersive propagation analysis discussed in Chapter 5, three peaks are expected in the envelope of cross-correlation coefficient:

1. First peak, which is positive, reveals the time delay between the arrival of incident or reflected wave at sensors A and B.
2. Second peak, which is negative, shows the time delay between the arrival of incident wave at A and reflected wave from right support at B.

3. Third peak, which is negative, shows the time delay between the arrival of incident wave at A and reflected wave from left support at B.

Figure (6.31) shows the cross-correlation coefficient of the acceleration measurements. The peaks are detected and presented in Table (6.5). This table also shows the calculated time delay and the percentage of error of the estimation.

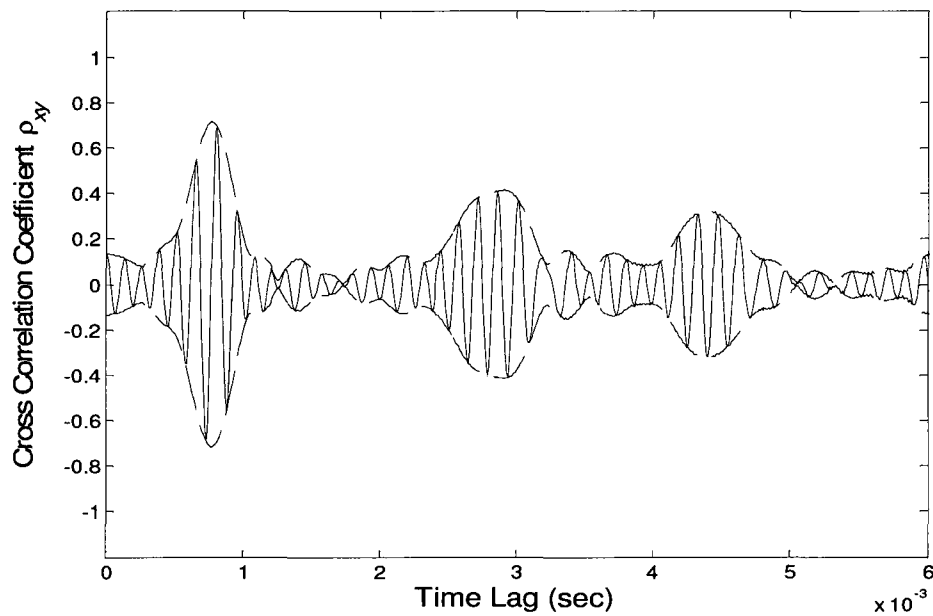


**Figure (6.31): Cross-correlation coefficient of acceleration response
in a simply supported beam**

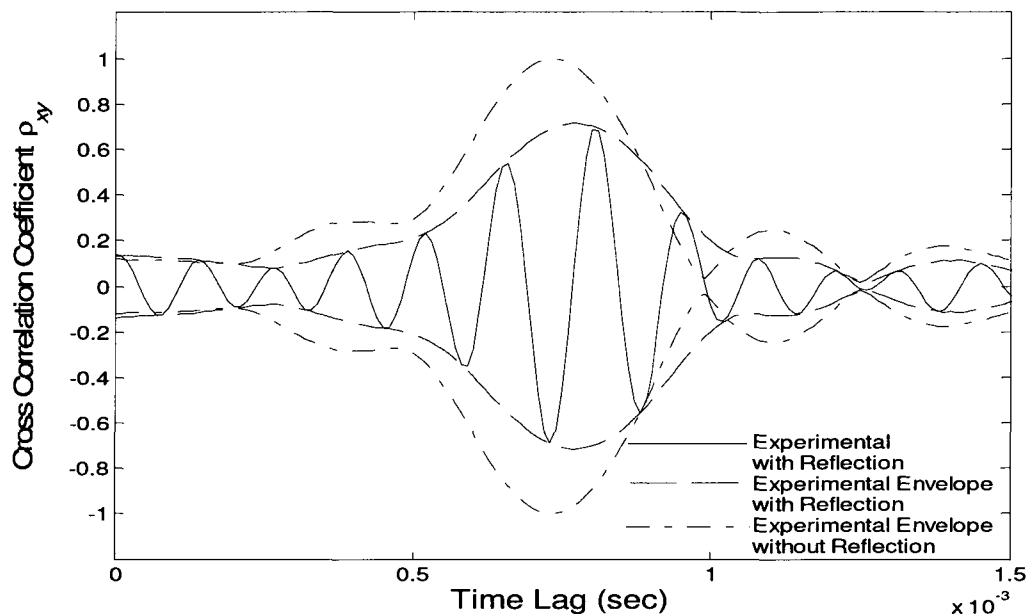


**Figure (6.32): First peak of cross-correlation coefficient of acceleration responses:
comparison of simply supported beam and infinite beam**

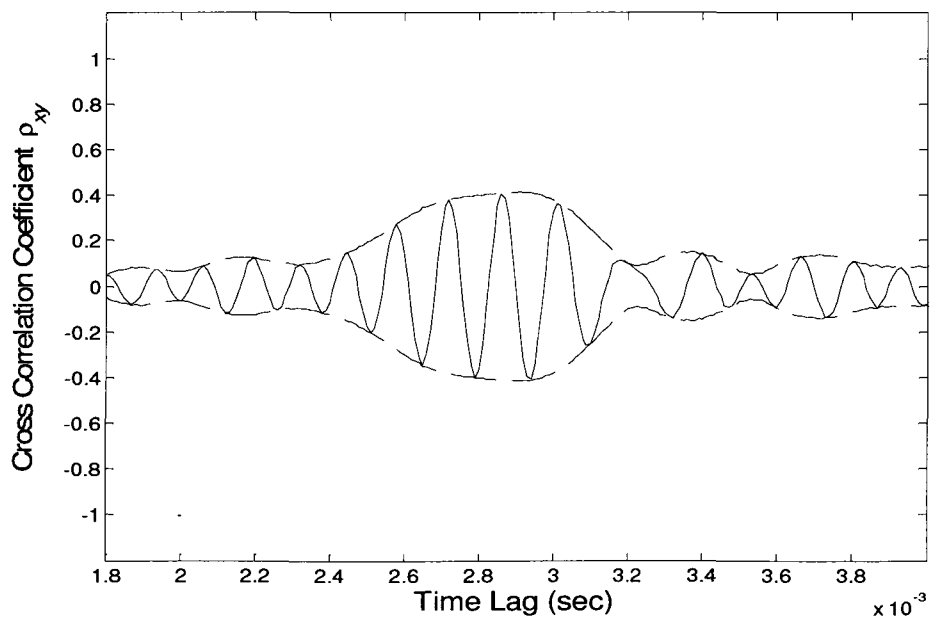


Figure (6.33): Second peak of cross-correlation coefficient of acceleration responses

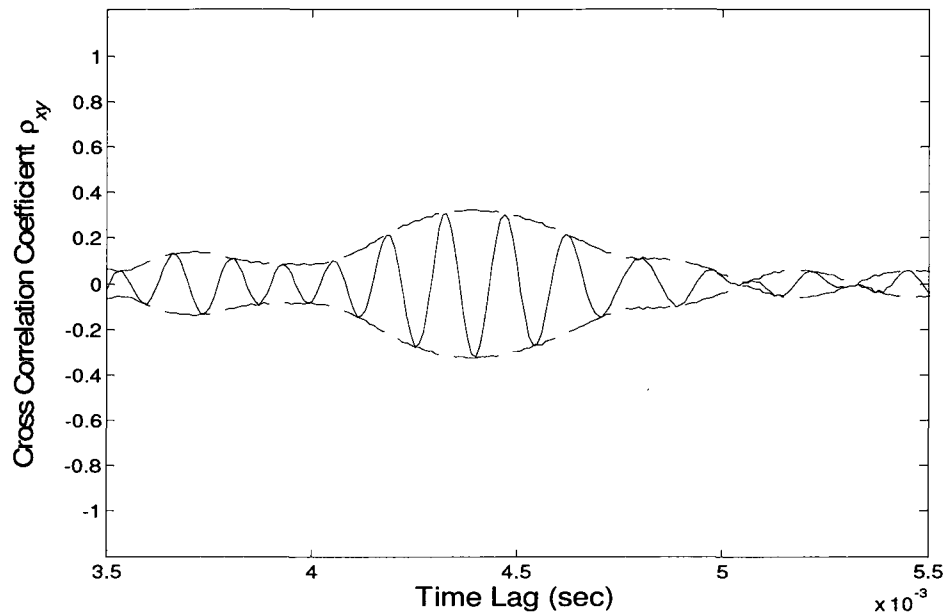


Figure (6.34): Third peak of cross-correlation coefficient of acceleration responses

	Calculated time delay	Estimated time delay	Percentage of error
First peak	0.00074 s	0.00077 s	4.0%
Second peak	0.00287 s	0.00291 s	1.4%
Third peak	0.00442 s	0.00440 s	0.5 %

Table (6.5): Percentage of error of estimated time delay

Figures (6.32), (6.33) and (6.34) show time delays in greater detail. According to the analysis presented here, the following conclusions can be drawn:

1. The first peak detected in the cross-correlation coefficient is less accurate comparing to the previous cases. This happens because the reflected waves, traveling the path between sensors A and B, are less correlated to each other.
2. The amplitude of the first peak is reduced because:
 - The reflected wave from right boundary passes ab from b to a while reflected wave from right boundary travels from a to b .
 - The reflected waves are not completely correlated due to the dispersion effect in dispersive path.
 - Dissipation (damping) in the system and numerical dispersion due to FEM discretization effect also create some degree of decorrelation.
3. The backward incident wave travels 10 m to reach left support and an extra 14.2 m to reach the sensor B. While traveling along a distance of 24.2 m , the wave loses its coherency to some extent, but the detected time delay is still reasonably clear in the cross-correlation coefficient.
4. The reflected wave from right support travels a 15.8 m path to reach sensor B, but the corresponding time delay is clearly identifiable in the cross-correlation coefficient.

6.3.4 Effect of Noise

In this section the effect of noise on the cross-correlation analysis is investigated. The model used in this analysis is shown in Figure (6.30): A simply supported beam is subjected to a narrow-band force with the central frequency $\omega_0 = 2\pi \times 6000\text{ rad/s}$ and

a bandwidth of $B = 2\pi \times 4000 \text{ rad/s}$. The noise level R that is introduced in the measurement $x(t)$ is defined as:

$$R = \frac{\sigma}{\max(x(t))} \quad (6.23)$$

where σ is the rms value associated with the measurement $x(t)$.

In this study two noise levels are introduced: (1) 15% noise, and (2) 30% noise. Figure (6.35) and Figure (6.36) show one sample of noisy acceleration response with 30% noise at both sensors A and B. The autospectral density functions of the noisy accelerations are plotted in Figure (6.37). Cross-correlation coefficient of the measurements at sensors A and B with 30% noise is plotted in Figure (6.38). In this figure, two peaks are clearly detected, but the last expected peak is smeared by noise. Figure (6.39), Figure (6.40) and Figure (6.41) show the peaks in greater detail. These figures also show a comparison between the effects of different levels of noise on the cross-correlation coefficient. It may be noted that

1. Recall that an increase in the level of the noise decreases the amplitude of cross-correlation coefficient at the estimated time delay. Hence the detection of the peak becomes more difficult.
2. An increased level of the noise does not change the locations of the peaks of cross-correlation coefficient indicating the time delays. This property is useful if the amplitude of the peak is distinct enough for time delay detection.

Based on these properties and the results presented in the preceding sections it can be concluded that

1. Even in the presence of 30% noise, the first peak can be readily detected.
2. For 15% and 30% percent noise levels the detection of the second peak becomes increasingly difficult.
3. For 15% and 30% noise, the third peak cannot be detected.

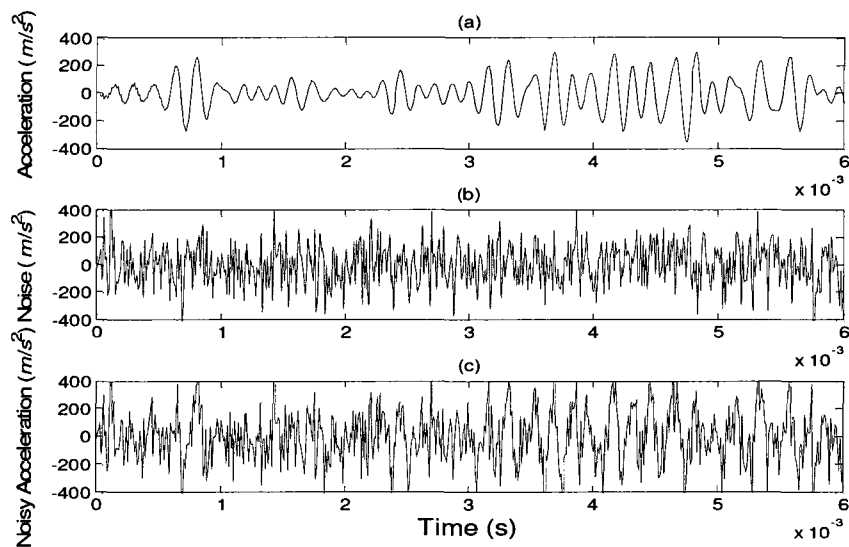


Figure (6.35): Response at sensor A a) acceleration b) noise(R=30%) c) noisy acceleration

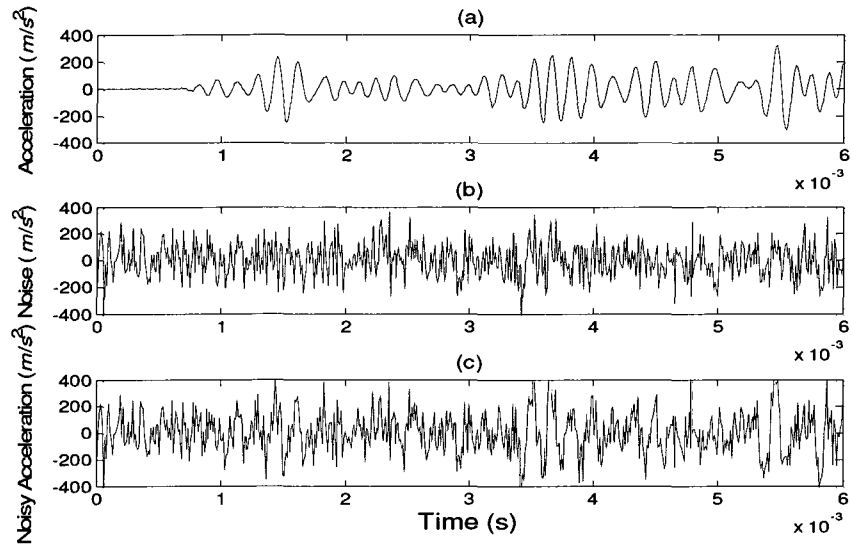
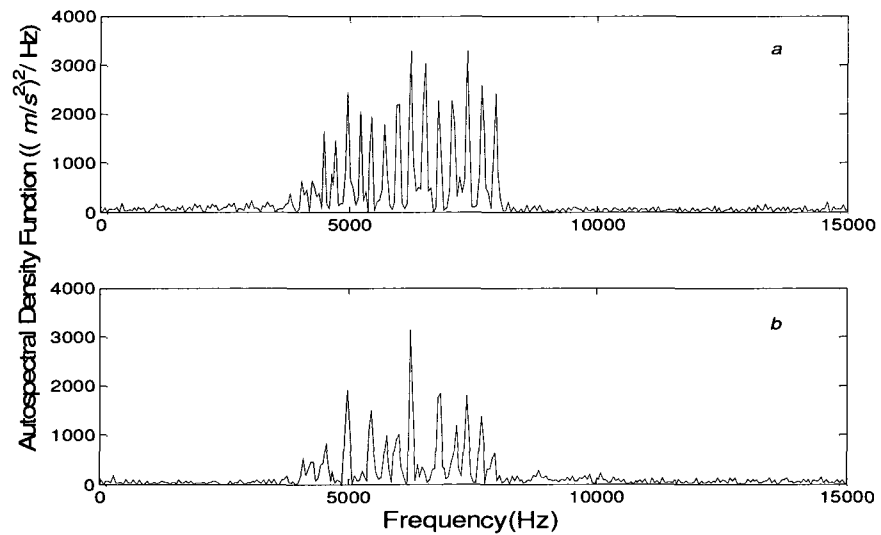
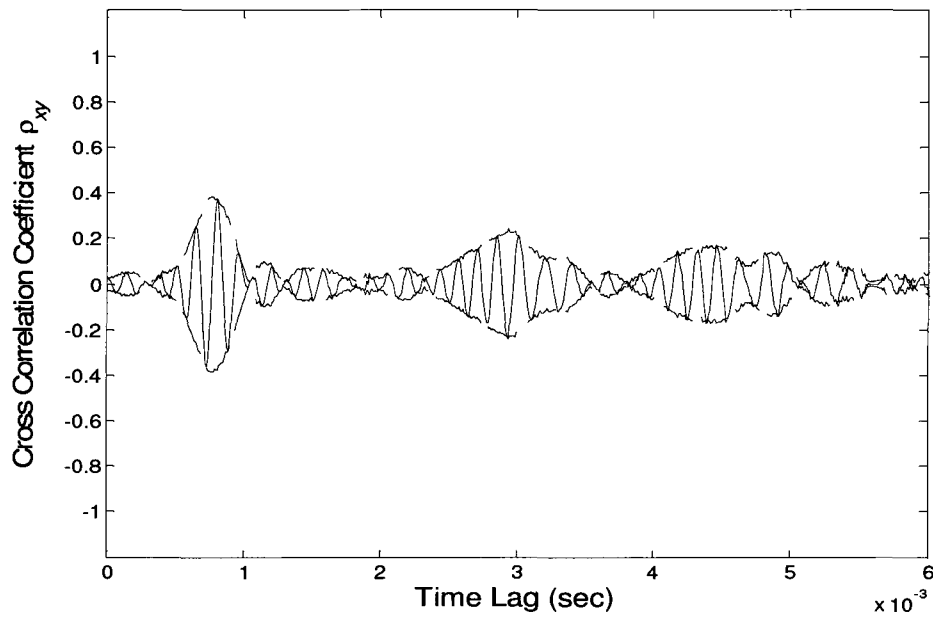


Figure (6.36): Response at sensor B a) acceleration b) noise(R=30%) c) noisy acceleration



**Figure (6.37): Aut spectral -density -function of noisy acceleration (R=30%) response at
a) sensor A b) sensor B**



**Figure (6.38): Cross-correlation coefficient of acceleration response
in presence of 30% noise**

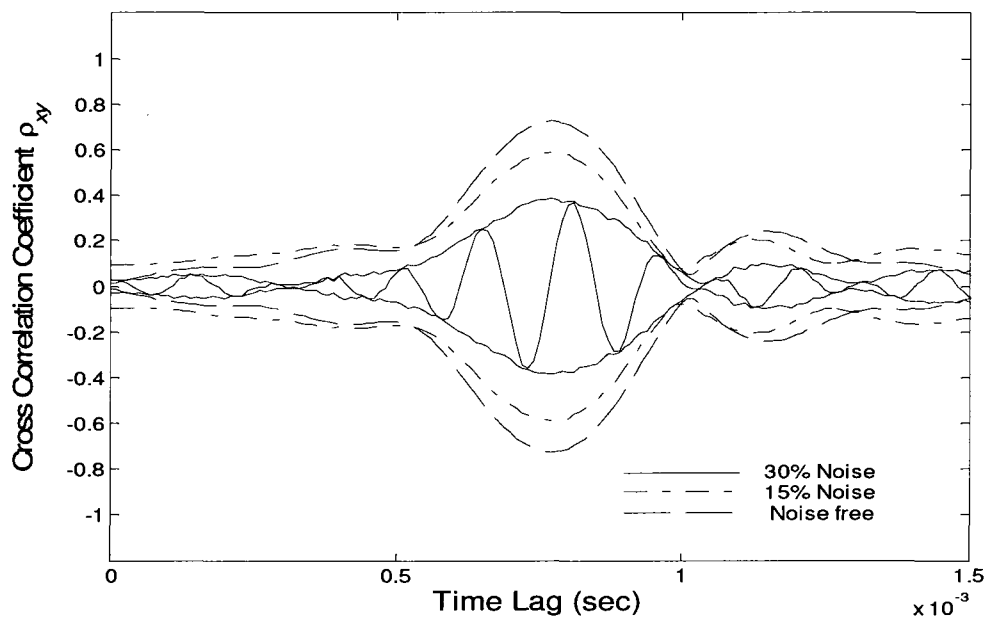


**Figure (6.39): Cross-correlation coefficient between noisy acceleration measurements:
comparison of the effect of different levels of noise on first peak**

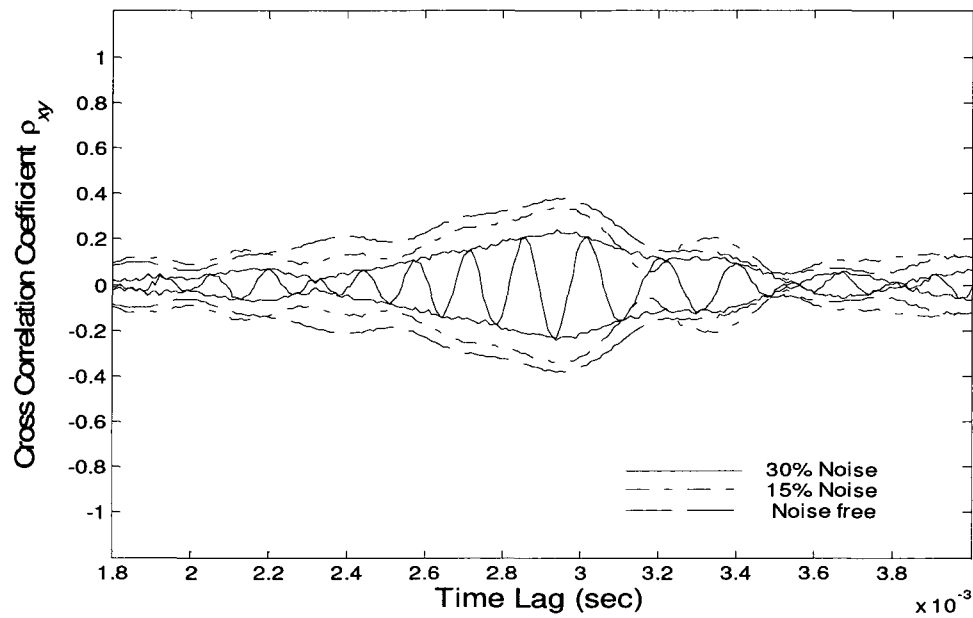


**Figure (6.40): Cross-correlation coefficient between noisy acceleration measurements:
comparison of the effect of different levels of noise on second peak**

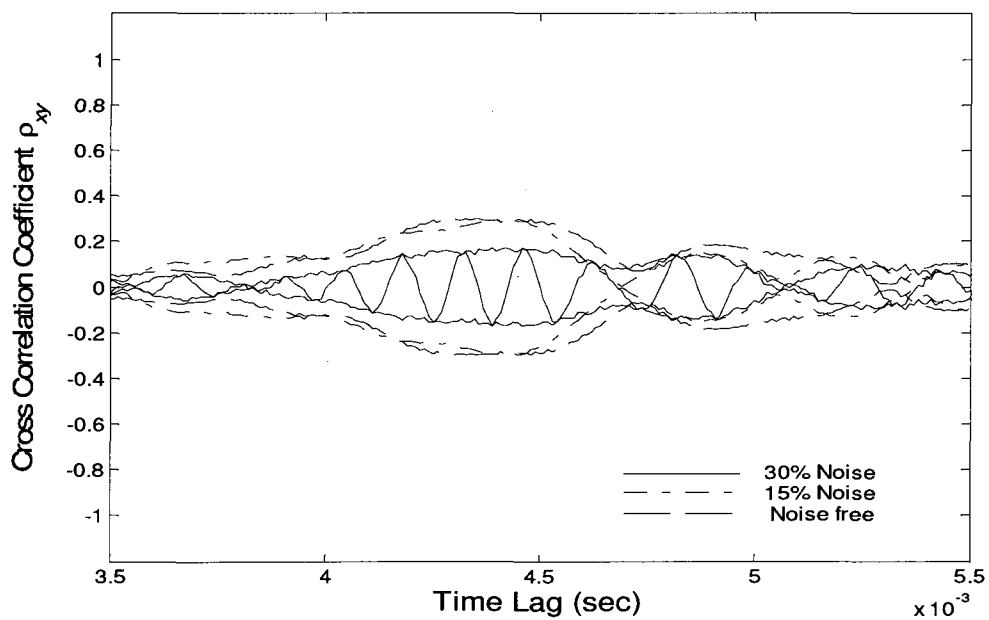


**Figure (6.41): Cross-correlation coefficient between noisy acceleration
measurements: comparison of the effect of different levels of noise on third peak**

In order to suppress the effect of noise, the cross-correlation function is used instead of cross-correlation coefficient. However, the results appear to be useful for detection of only the first peak. This fact is clarified in Figures (6.42), (6.43) and (6.44).

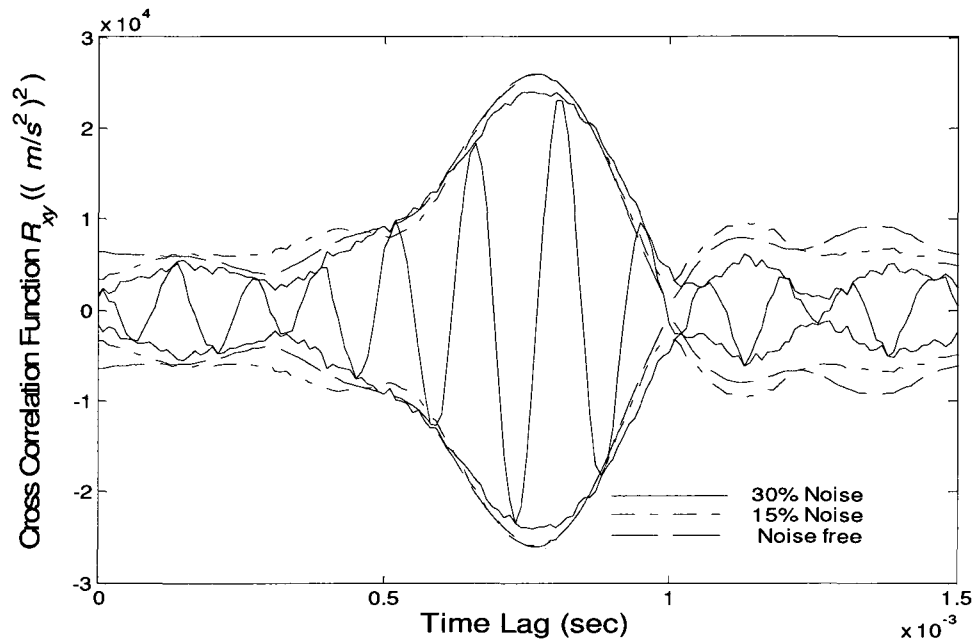


**Figure (6.42): Cross-correlation function between noisy acceleration measurements:
comparison of the effect of different levels of noise on first peak**

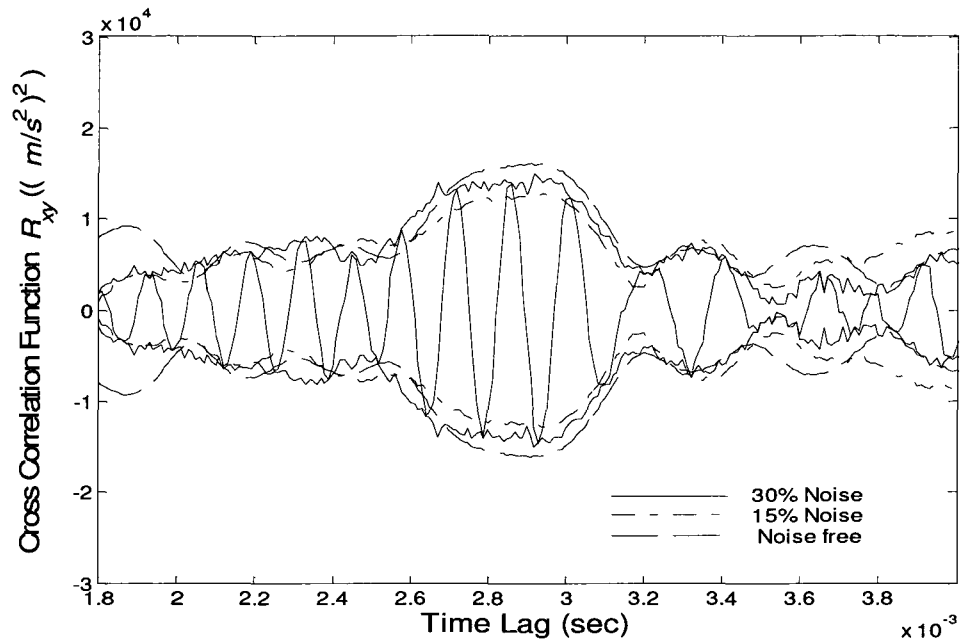


**Figure (6.43): Cross-correlation function between noisy acceleration measurements:
comparison of the effect of different levels of noise on second peak**

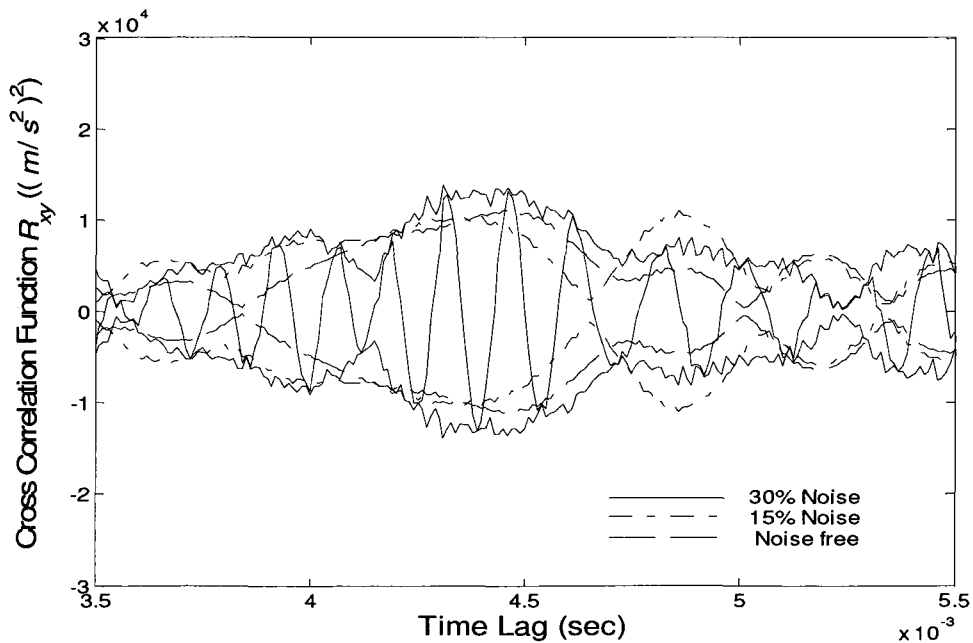


**Figure (6.44): Cross-correlation function between noisy acceleration measurements:
comparison of the effect of different levels of noise on third peak**

6.4 Damage Detection

In this section, cross-correlation analysis is used to detect damage in a dispersive waveguide representing bending wave propagation in a beam. The model is a simply supported beam shown in Figure (6.45). As discussed in the previous chapter, dispersion of waves causes difficulty in the detection of time delay between the noisy measurements of incident and reflected waves; hence only the time delay caused by the incident waves is investigated. For simplicity, the damage detection procedure is restricted only to the case where damage occurs between the measurement locations.

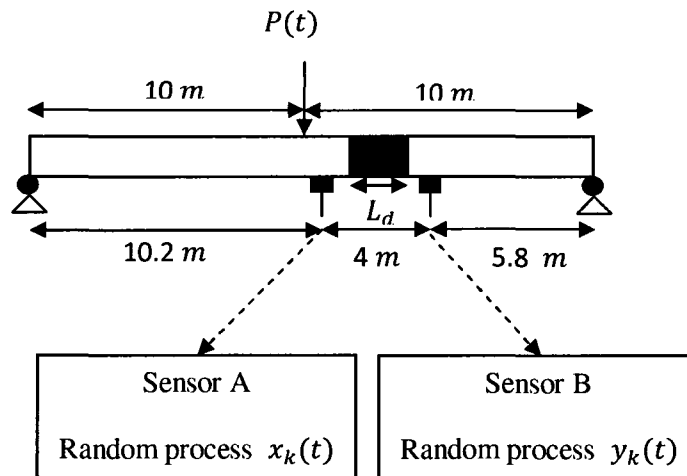


Figure (6.45): Beam model for time delay estimation problem: investigation of damage in a beam

Simulated damage is introduced over its length L_d and the extent of simulated damage is s . Specifically, L_d refers to the length of damage while s indicates the percentage reduction in the flexural stiffness of the beam. In this analysis, the mass of the damaged element is assumed to be unchanged.

Based on this assumption the group wave speed in the damage area is defined as

$$\begin{aligned} c_{gd} &= 2\sqrt{\omega} \left(\frac{(1-s)EI}{m} \right)^{1/4} = 2(1-s)^{1/4} \sqrt{\omega} \left(\frac{EI}{m} \right)^{1/4} \\ &= (1-s)^{1/4} c_g \end{aligned} \quad (6.24)$$

where c_{gd} denotes the group speed in the damaged area, and c_g is the group speed of undamaged beam. Two cases for the length of damage are considered:

1. $L_d = 2 m$
2. $L_d = 4 m$

In each case, analyses are carried out for three different values for the extent of damage.

1. $s = 25\%$
2. $s = 50\%$
3. $s = 75\%$

The beam is subjected to a narrow-band white random force with the central frequency $\omega_0 = 2\pi \times 6000 \text{ rad/s}$ and one octave bandwidth $B = 2\pi \times 4000 \text{ rad/s}$. All the measurements in this section are assumed to be corrupted by 20% noise.

6.4.1 Damage Length $L_d = 2\text{ m}$

Cross-correlation function of the acceleration measurements at sensors A and B is plotted in Figure (6.46). It will be noted that

1. Damage causes delay in the propagation of wave between two locations of the beam manifested through the shifts in the peaks of cross-correlation.
2. Higher magnitude of damage extent increases the time delay between two measurement points

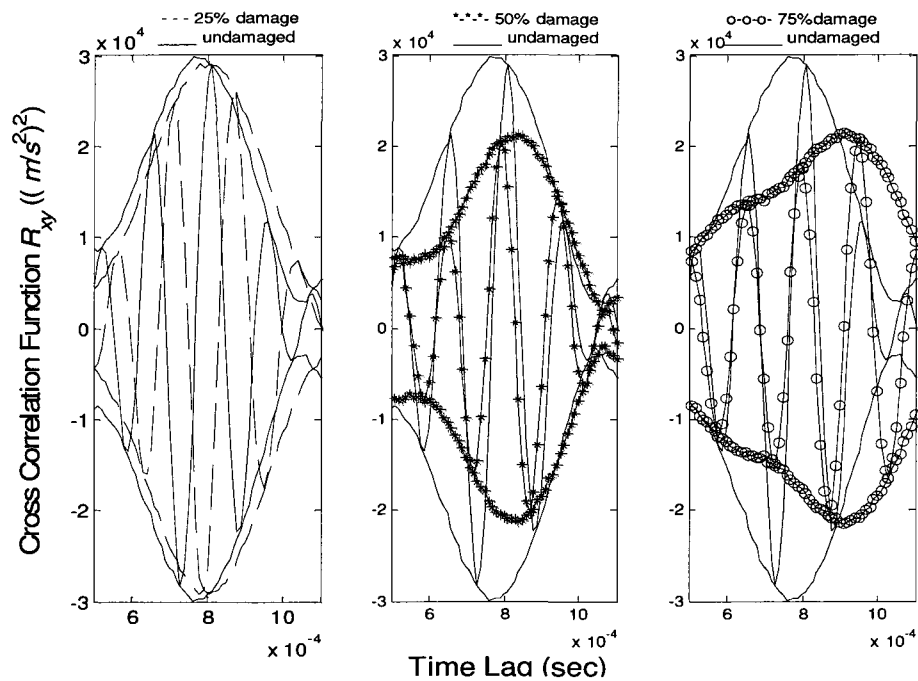


Figure (6.46): Cross-correlation function of acceleration measurements: comparison of the effect of different damage extent (damage length 2 m)

Damage extent is computed based on the comparison of the time delay in the undamaged and damaged model. Two cases are considered:

In the first case, it is assumed that the damage length is known and is equal to L_d . Hence one obtains

$$\frac{t}{t_d} = \frac{\frac{d}{c_g}}{\frac{d - L_d}{c_g} + \frac{L_d}{c_{gd}}} \quad (6.25)$$

where t and t_d are the time delays in undamaged and damaged beam, respectively, d and L_d are the length of propagation path and the length of damaged area, and c_g and c_{gd} are, respectively, the group wave speed in undamaged and damaged beam. Using Equation (6.24), one obtains

$$\frac{t}{t_d} = \frac{(1 - s)^{1/4} d}{(1 - s)^{1/4} d + (1 - (1 - s)^{1/4}) L_d} \quad (6.26)$$

In the second case, it is assumed that the damaged length is unknown. The entire propagation path d is considered as the damage length L_d . Using Equation (6.27), one obtains

$$\frac{t}{t_d} = (1 - s)^{1/4} \quad (6.27)$$

Of course such assumptions on the damage length only provide the minimum estimate of damage extent. If more accurate estimate of damage extent is needed, higher number of sensors (more than two) would be required. Table (6.6) shows the calculated damage extent.

	Time delay in undamaged beam	Time delay in damaged beam	Damage extent	
			Known damage length	Unknown damage length
First case (s=25%)	0.00076 s	0.00078 s	18.5% s	9.9% s
Second case (s=50%)		0.00084 s	53.4% s	33.0% s
Third case (s=75%)		0.00091 s	73.6% s	51.3% s

Table (6.6): Calculation of damage extent in damaged beam (damage length 2m)

6.4.2 Damage Length $L_d = 4\text{ m}$

In this case, it is assumed that the entire length of the propagation path between sensors A and B is damaged. Figure (6.47) shows the cross-correlation function of the noisy acceleration measurements at sensors A and B. The calculation of damage extent is presented in Table (6.7).

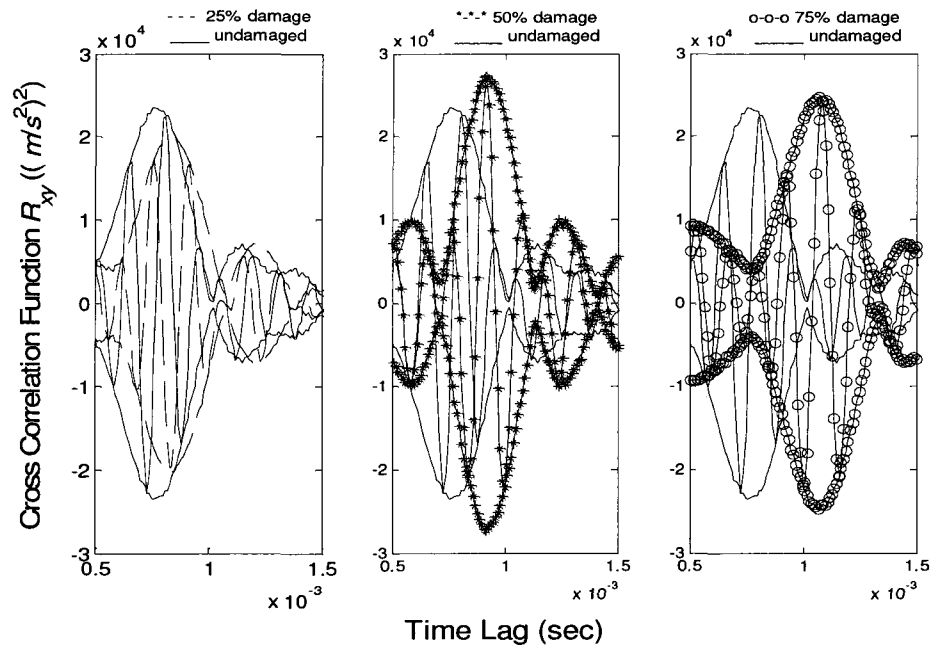


Figure (6.47): Cross-correlation function of acceleration measurements: comparison of the effect of different damage extent (damage length 4 m)

	Time delay in undamaged beam	Time delay in damaged beam	Damage extent
First case (s=25%)	0.00076 s	0.00084 s	33.0%
Second case (s=50%)		0.00092 s	53.4%
Third case (s=75%)		0.00107 s	74.5%

Table (6.7) Calculation of damage extent in damaged beam (damage length 4m)

In comparison to the previous case, because the damage introduced in the beam is more severe (a greater length is damaged); the time delay shifts are longer. This property makes the detection of the time delay easier.

In the following sections, advantages and disadvantages of the proposed approach are discussed.

6.4.3 Conclusions

The advantages of this approach are summarized below:

1. This approach is data-driven. There is no need to define any specific model.
2. The analysis presented is applicable to any type of loading (transient or stationary).
3. One of the main difficulties of conventional damage detection approaches (i.e. modal analysis based methods) is the high degree of sensitivity to the measurement noise. It is shown that the correlation analysis provides acceptable results in the presence of high levels of measurement noise.
4. The simplicity of the presented approach makes it applicable to engineering problems.

The limitations of presented approach for detection of damages in dispersive waveguides are:

1. Unlike non-dispersive wave propagation, use of the information related to reflected waves from the boundary seems to be difficult. Hence prediction of the damage location requires more measurement locations.
2. In contrast to non-dispersive wave propagation, minor damages are difficult to detect when using this approach for dispersive media.

The general limitations of the proposed approach (both for non-dispersive and dispersive propagation cases) are:

1. This approach is not applicable to non-linear cases.
2. Prediction of the location and severity of damage needs more sensors.
3. In the analysis performed in this thesis, only one dimensional elements namely rod and beam are considered. In two and three dimensional waveguides, waves are traveling in more than one direction. Hence application of the proposed approach may have pose difficulties resolution of which requires further research.
4. The noise simulated in this analysis is assumed to be measurement noise only. For such noise the assumption of low degree of correlation between noises at two different locations is quite reasonable. However the effects of model noise such as due to environmental effects, which may have high degree of correlation between different locations, are not considered in the current investigation.

Chapter 7

Summary, Conclusions and Future Research

7.1 Summary

The non-model approach to vibration based damage identifications is based on comparison between the values of a dynamic parameter obtained directly from measurements in intact and damaged structures. The parameter chosen in this work is wave speed. In order to find the wave speed an estimate of the time delay in the arrival of the wave between two neighboring measurement points is required. Cross-correlation analysis, which is being used in several different fields of engineering, is applied in this work to obtain the estimate of time delay. In order to evaluate the effectiveness of this technique computer simulation studies are carried out on two different one-dimensional structures: an infinite rod, which acts as a non-dispersive waveguide, and an infinite beam, which is a dispersive waveguide. Use of infinitely long structures guarantees that the response includes only the incident wave. For the purpose of simulation numerical solutions of the response at two neighboring locations of a mathematical model of the structure are obtained by Fast Fourier transform. The excitation is assumed to be an

impulsive force applied at the middle of the structure, that is, at the origin of the single coordinate. Cross-correlation analysis is performed on these solutions. The results show that the technique has a high level of accuracy for both the rod and the beam and under each of the different loading conditions used in the analysis.

In the next step, boundary conditions are imposed on the simulation models to investigate the effect of reflection from boundaries. Finite element models are used to achieve this. Cross-correlation analyses of the responses provide accurate results for the arrival times of incident as well as reflected waves for both the rod and the beam models.

Next, in order to simulate the most realistic measurements, random errors are introduced in the results obtained from FEM. Such errors represent the presence of noise in the measurements. The cross-correlation analysis is performed in the presence of different levels of noise. It is shown that the effect of noise can be suppressed to a large degree by using cross-correlation function instead of cross-correlation coefficient. The results are still accurate and reliable in the case of non-dispersive wave. However in the dispersive case, the results obtained for reflected waves become inaccurate when noise is present. Further research is required for this case.

At the final step, a procedure for damage detection based on the comparison of wave speed in undamaged and damaged waveguides is developed. In the non-dispersive case, an initial estimate of damage location and the minimum possible amount of damage is predicted. In the dispersive case the estimate of damage location can be predicted only when it lies in the path between two measurement locations. Further investigations need to be carried out for this case.

7.2 Conclusions

The following conclusions can be drawn from the work presented in this thesis:

Non-dispersive waveguide

1. The time delay between two acceleration measurement locations in a non-dispersive waveguide excited by narrow-band, broad-band or transient forces, can be estimated quite accurately, even in the presence of high level of noise. In the examples presented in this work the error in the time delay estimate was found to be less than 1%.
2. If a non-dispersive waveguide has fixed boundary conditions at the ends, the time delay between incident and reflected waves can be estimated quite accurately, even in the presence of high levels of noise. In the examples in this work the error in the estimate was again less than 1%.
3. Based on two measurement locations in a non-dispersive waveguide with fixed boundary conditions, an initial estimate can be obtained of the location of even a low level of damage caused by axial stiffness reduction. This is true even when a high level of noise is present. If the length of damage is known, the extent of damage can be estimated accurately, otherwise the minimum possible damage

extent can be found. To refine the estimate of the damage location and hence of the damage extent more closely spaced measurement locations would be required.

Dispersive waveguide

1. The time delay between two acceleration measurement locations in a dispersive waveguide excited by narrow-band, broad-band or transient forces, can be estimated quite accurately, even in the presence of high level of noise. Again, the error in the estimate was less than 1% in the examples presented in this work. The distance between measurement locations should be such that the coherency of dispersive waves is guaranteed.
2. If a dispersive waveguide has pinned supports at the ends, the time delay between the arrival acceleration waves can be estimated with fair accuracy, the error being less than 5% in the examples presented in this work. This holds true even in the in the presence of low levels of noise.
3. In a dispersive waveguide with pinned supports at the ends, presence of damage caused by flexural stiffness reduction can be found, provided such damage lies between two neighboring measurement locations. If the length of damage is known, the extent of damage can be estimated accurately, otherwise the minimum possible damage extent can be found. The damage detection procedure described

here to small damage is not as effective for a dispersive waveguide as it is for a non-dispersive waveguide.

7.3 Future Research

Time delay estimation

1. In the time delay detection of dispersive wave propagation discussed in the current study, the time delay is found for a specific band of frequency. As a long-term research focus, it will be very useful to provide a time-frequency-amplitude representation of dispersive wave propagation. This representation can be obtained using time-frequency analysis tools such as wavelet analysis or Hilbert-Huang transform. In this context, any decomposition that can extract group waves from a dispersive wave seems to be promising.
2. In this work, the response of a dispersive waveguide to the broad-band force is filtered to narrow-band of frequency in order to use cross-correlation analysis for the estimation of time delay. The filter, which is chosen in this study, is frequency selective filter. One of the major problems of frequency selective filters is phase distortion. Hence the time delay estimates obtained from such filtered signals is less accurate. Time domain decomposition of the wave could results in more accurate results. One of the new decomposition methods that can be applied to non-stationary and non-linear signals is Empirical Mode Decomposition.

3. In the current study, the time delays detected are related to the positive time delay axis. There are also other peaks that appear in the negative side of time delay axis. These peaks contain some information about the dynamic characteristics of the waveguide and reflection properties from the boundaries. Investigation of the time delay detected by these peaks and their amplitude may provide more useful knowledge about the dynamic system.
4. The effect of boundary conditions on dispersive wave propagation needs to be investigated in more details. Defining some criteria for correlation length, in which the coherency of dispersive wave is guaranteed, leads to an upper limit for the propagation path. Investigation of time delay estimation for the propagation of reflected waves in a path that satisfies this limitation may lead to extraction of more information about the reflection in dispersive medium and needs additional study.

Damage detection

1. The efficiency of cross-correlation analysis for estimation of time delay between incident waves in both non-dispersive and dispersive waveguides has been validated through experiments in previous studies (White, 1969). Based on the analysis carried out in this thesis, the applicability of time delay estimation in damage detection also needs to be investigated through laboratory experiments.

2. In this study, the damage is modeled by reduction in axial and flexural stiffness in non-dispersive and dispersive waveguides, respectively. This simple model does not take into account the effect of scattering of the wave in the damaged area. A more precise modeling of the wave propagation in the damaged propagation path is necessary.
3. The focus of this work is on the detection of time delay shifts due to damage. If the dissipation of energy of the system caused by damage can be modeled, the amplitude of cross-correlation coefficient should show decrement. Hence a combination of time delay shift and decrement of cross-correlation coefficient at the time delay could be a promising tool for use in damage detection.
4. The analysis performed in the current work is based on single path propagation. The mathematical derivation of multiple path propagation, especially in non-dispersive wave propagation, is available in the literature. Using that basis, investigation of the applicability and effectiveness of the techniques studied here in damage detection of more complex structures is worthy of further study.

References

1. Amin, M. S. 2002. An Integrated Vibration-Based Structural Health Monitoring System. PhD thesis, Dept of Civil & Environmental Engineering, Carleton University, Ottawa, Canada.
2. Bedrosian, E. 1963. A product theorem for Hilbert transforms. Proc IEEE (lett), No. 51, 868-869.
3. Bendat, J.S. 1958. Principles and Applications of Random Noise Theory. John Wiley & Sons, New York.
4. Bendat, J.S. 1985. The Hilbert Transform and Application to Correlation Measurements. Bruel and Kjaer, Denmark.
5. Bendat, J.S. and Piersol, A. G. 1986. Random Data: Analysis and Measurement Procedures. John Wiley & Sons, New York.
6. Bendat, J.S. and Piersol, A.G. 1993. Engineering Application of Correlation and Spectral Analysis. John Wiley & Sons, New York.
7. Brillouin, L. 1960. Wave Propagation and Group Velocity. Academic Press, New York.
8. Chang, F.-K., 2001. Structural Health Monitoring 2000. CRC Press, 1062 pp.
9. Chang, F.-K., 2003. Structural Health Monitoring 2003: From Diagnostics and Prognostics to Structural Health Management. DEStech Publications, Inc, 1552 pp.
10. Doebling, S.W., Farrar, C.R., Prime, M.B. and Shevitz, D.W. 1996. Damage Identification and Health Monitoring of Structural and Mechanical Systems from

Changes in their Vibration Characteristics: A Literature Review. Los Alamos National Laboratory, Los Alamos, New Mexico, Report No. LA 13070-MS.

11. Doebling, S. W., Farrar, C. R. and Prime, M. B. 1998. A Summary Review of Vibration Based Damage Identification Methods. *The Shock and Vibration Digest*, Vol. 30, No. 2, 91-105.
12. Doyle, J.F. 1997. *Wave Propagation in Structures*. Springer, New York.
13. Elmore, W. C. and Heald, M. A. 1985. *Physics of Waves*, Dover, New York.
14. Farrar, C. R. and Sohn H. 2001. Condition/Damage Monitoring Methodologies. The Consortium of Organizations for Strong Motion Observation Systems Workshop, Invited talk, Emeryville, CA, LA-UR-01-6573.
15. Ghanem, R. and Ferro, G. 2006. Health Monitoring for Strongly Non-linear Systems Using the Ensemble Kalman Filter. *Structural Control and Health Monitoring*, Vol. 13, Issue 1, 245-259.
16. Hera, A. and Hou, Z. 2004. Application of wavelet Approach for ASCE Structural Health Monitoring Benchmark Studies. *Journal of Engineering Mechanics*, Vol. 130 No. 1, 96-104.
17. Huang, N.E., Shen, Z., Long, S. R., Wu, M. C., Shih, H.H., Zheng, Q., Yen, N.C., Tung, C.C. and Liu, H.H. 1998. The Empirical Mode Decomposition and the Hilbert Spectrum for Nonlinear and Non-Stationary Time Series Analysis. *Proceeding of the Royal Society of London*, Vol. 454, No. 1971, 903-995.
18. Humar, J. L. 2002. *Dynamics of Structures*. Swets & Zeitlinger B.V. Lisse.

19. Humar, J. L., Bagchi, A. and Xu, H. 2006. Performance of Vibration-based Techniques for the Identification of Structural Damage. *Structural Health Monitoring*, Vol. 5, No. 3, 215-245.
20. Mufti, A. A. 2001. Guidelines for Structural Health Monitoring. Design Manual, No.2.
21. Novikov, A. K. 1962. Spatial Correlation of Plane Bending Waves. *Soviet Physics-Acoustics*, Vol. 7, No. 4, 374-379.
22. Pines, D. and Salvino, L. 2006. Structural Health Monitoring Using Empirical Mode Decomposition and the Hilbert Phase. *Journal of Sound and Vibration*, Vol. 294, No. 1-2, 97-124.
23. Rytter, A. 1993. Vibration Based Inspection of Civil Engineering Structures. Ph.D Dissertation. Department of Building Technology and Structural Engineering, Alborg University, Denmark.
24. Salvino, L. W., Pines D. J., Todd, M. and Nicholas, J. M. 2005. EMD and Instantaneous Phase Detection of Structural Damage, Chapter 11. World Scientific Publishing, Singapore.
25. Staszewski, W. J. 1998. Structural and Mechanical Damage Detection Using Wavelets. *The Shock and Vibration Digest*, Vol. 30, No. 6, 457-472.
26. White, P. H. 1969. Cross-Correlation in Structural Systems: Dispersive and Non-dispersive Waves. *Journal of Acoustical Society of America*, Vol. 45, No. 5, 118-1128.

27. Winter, E. F. and Bies, D. A. 1962. Correlation Properties of Flexural Waves in Long Thin Bars. *The Journal of Acoustical Society of America*, Vol. 34, Issue 4, 472-475.
28. Xu, H. 2005. Application of Artificial Neural Networks in Vibration-Based Damage Identification. PhD thesis, Dept of Civil & Environmental Engineering, Carleton University, Ottawa, Canada.
29. Yang, J. N., Lin, S., Huang H. and Zhou, L. 2006. An Adaptive Extended Kalman Filter for Structural Damage Identification. *Structural Control and Health Monitoring*, Vol. 13, Issue 4, 849-867.
30. Yang, Z., Yu, Z. and Sun H. 2007. On the Cross Correlation Function Amplitude Vector and its Application to Structural Damage Detection. *Mechanical Systems and Signal Processing* Vol. 21 Issue 7, 2918-2932.